NANOMESH ON SIC SURFACE: STRUCTURE, REACTIONS AND TEMPLATE EFFECTS

CHEN SHI

(*B. Sc, ZHEJIANG UNIV*)

A THESIS SUBMITTED

FOR THE DEGREE OF DOCTOR OF PHILOSOPHY

DEPARTMENT OF PHYSICS

NATIONAL UNIVERSITY OF SINGAPORE

(2010)

DEDICATION

To my beloved wife and parents

ACKNOWLEDGEMENT

Over the past five years, I received numerous helps from my supervisors, friends and my family to complete this thesis. I am indebted to them for their precious help and wish to express my gratitude to them at here.

First and foremost, I would like to express my deepest gratitude to my supervisor, Professor Andrew Thye Shen Wee; a respectable, responsible and resourceful scholar, who has seamlessly guided me in every stage of this project. Despite having a busy schedule as the head of physics department and the Dean of Science, Professor Wee has graciously spent a great amount of time on my thesis, meticulously reading through all my manuscripts. I would not be able to finish this thesis without his constant support. Prof. Wee also grants me research assistantship and supports my extensions to finish this thesis.

I would like to thank my co-supervisor, Professor Gao Xingyu, who led me into the fascinating world of surface science and synchrotron facilities. He gave many suggestions on the design of experiments and taught me how to extract important information from experimental data. He also brought me to Japan several times to conduct important experiments and to have exciting tours.

I would like to thank assistant professor Chen Wei for his support in STM experiments. As an expert in STM and PES, he gave me many valuable suggestions to my thesis. He also supported me by granting research assistantship to me during the writing of thesis.

I would like to thank Dr. Liu Tao for his help in conducting calculations for the XAS data by WINXAS and FEFF. His works are vital to make my experimental results meaningful and convincing.

Last but not least, I would like to thank Dr. Qi Dongchen, Mr. Wang Yuzhan. You are my best friends both in work and in life. I will never forget those happy times we had in past five years.

LIST OF PUBLICATIONS

Template-Directed Molecular Assembly on Silicon Carbide Nanomesh: Comparison Between CuPc and Pentacene

Shi Chen, Wei Chen, Han Huang, Xingyu Gao, Dongchen Qi, Yuzhan Wang, and Andrew, T. S. Wee

ACS NANO, **4**, 849, (2010)

Si clusters on reconstructed SiC (0001) revealed by surface extended x-ray absorption fine structure

Xingyu Gao, **Shi Chen**, Tao Liu, Wei Chen, Andrew T. S. Wee, T. Nomoto, S. Yagi, Kasuo Soda and Junji Yuhara

APPLIED PHYSICS LETTERS **95**, 144102 (2009)

Disorder beneath epitaxial graphene on SiC(0001): An x-ray absorption study

Xinyu Gao, **Shi Chen**, Tao Liu, Wei Chen, Andrew T. S. Wee, T. Nomoto, S. Yagi, Kasuo Soda and Junji Yuhara

PHYSICAL REVIEW B **78**, 201404(R) (2008)

Probing the interaction at the C-60-SiC nanomesh interface

Wei Chen, **Shi Chen**, Hongliang Zhang, Hai Xu, Dongchen Qi, Xingyu Gao, Kian Ping Loh and Andrew T. S. Wee

SURFACE SCIENCE **601**, 2994 (2007)

The formation of single layer graphene on silicon oxide

Shi Chen, Han Huang, Yuzhan Wang, Dongchen Qi, Wei Chen, Jiatao Sun, Xingyu Gao, Andrew T. S. Wee

In preparation

Formation of silicon dioxide interlayer by oxidation of epitaxial graphene

Shi Chen, Han Huang, Yuzhan Wang, Dongchen Qi, Wei Chen, Xingyu Gao, Andrew T.S. Wee

In preparation

TABLE OF CONTENTS

ABSTRACT

In this thesis, the nanomesh structure on the 6*H*-SiC(0001) surface, also known as the $6\sqrt{3} \times 6\sqrt{3}$ R30º reconstruction, is experimentally studied. Several surface analytical methods including synchrotron based X-ray photoelectron spectroscopy (XPS), X-ray absorption spectroscopy (XAS), scanning tunneling microscopy (STM) and other complementary methods are used in this investigation. The XPS study reveals a variable elemental composition in this structure depending on the duration of annealing, suggesting that this structure is thermodynamically metastable. Substantial surface disorders at short and intermediate length scales are observed by STM, implying that the surface comprises of self-organized local structures instead of a global surface reconstruction.

Due to the richness of carbon in the nanomesh structure, most studies focus on the carbon atoms. In this thesis, the silicon atoms in the nanomesh are studied by XAS method at the Si *K*-edge using both surface sensitive and bulk sensitive yields. Using the bulk sensitive yield, silicon vacancies are identified, revealing that the silicon desorption process not only happens at surface but also from the bulk beneath the surface. Using the surface sensitive yield, Si-Si bonds are observed, suggesting that the SiC nanomesh surface also contains silicon clusters. The existence of surface silicon is also supported by the oxidation of the SiC nanomesh at elevated temperature, in which surface silicon oxide formation is observed. The reaction of the

SiC nanomesh is also observed even when it is covered by an epitaxial graphene (EG) overlayer. Both oxygen molecules and iron atoms are able to penetrate the topmost EG layer and react with the SiC nanomesh, giving rise to the formation of silicon dioxide and iron silicide at the interface, respectively. Intercalation at the EG/SiC nanomesh interface provides a possible route to modify the EG-substrate interface without external transfer of the EG film.

Having a honeycomb-like corrugation in long range, the SiC nanomesh has a potential application as a nanotemplate. In this work, the template effect of this surface is probed by three organic molecules: fullerene, copper phthalocyanine (CuPc) and pentacene. Spherical fullerene molecules are not affected by the surface corrugations, packing closely together. CuPc molecules, on the other hand, are confined by the cells of the SiC nanomesh, forming single molecular arrays. Pentacene molecules are also confined by the cells, and form a quasi-amorphous layer due to random adsorption at three equivalent absorption sites. As no significant molecule-substrate interaction is present, the different behaviors of three molecules suggest that the geometry of molecules play an important role in the template effect of the SiC nanomesh.

LIST OF TABLES

LIST OF FIGURES

LIST OF ABBREVIATIONS

AEY	Auger Electron Yield
ARPES	Angular Resolved Photoelectron Spectroscopy
ARUPS	Angular Resolved Ultraviolet Photoelectron Spectroscopy
AFM	Atomic Force Microscopy
BE	Binding Energy
BLG	Bilayer Graphene
DFT	Density Functional Theory
DOS	Density of States
EDC	Energy Distribution Curve
EG	Epitaxial Graphene
EXAFS	Extended X-ray Absorption Fine Structure
EY	Electron Yield
FWHM	Full Width at Half Maximum
FY	Fluorescence Yield
HOPG	Highly Oriented Pyrolytic Graphite
HREELS	High Resolution Electron Energy Loss Spectroscopy
IMFP	Inelastic Mean Free Path
KRIPES	Momentum-resolved Inverse Photoelectron Spectroscopy
LDOS	Local Density of States
LEED	Low Energy Electron Diffraction

LT	Low Temperature
MBE	Molecular Beam Epitaxy
ML	Monolayer
NEXAFS	Near Edge X-ray Absorption Fine Structure
PEY	Partial Electron Yield
PES	Photoelectron Spectroscopy
RFM	Refocusing Mirror
SiC	Silicon Carbide
SLG	Single Layer Graphene
STM	Scanning Tunneling Microscopy
TEY	Total Electron Yield
UHV	Ultrahigh Vacuum
UPS	Ultraviolet Photoelectron Spectroscopy
VT	Variable Temperature
XAS	X-ray Absorption Spectroscopy
XRD	X-ray Diffraction
XPS	X-ray Photoelectron Spectroscopy

CHAPTER 1 INTRODUCTION

1.1 Silicon carbide and its surface reconstructions

1.1.1 The structure and properties of silicon carbide

Silicon carbide (SiC) is a binary material with a 1:1 ratio of carbon and silicon atoms. Each Si (C) atom is covalently bonded to four nearest-neighbor C (Si) atoms in a tetrahedral coordination (sp^3 configuration) similar to the diamond structure.[1] With two different atoms in this tetrahedral structure, the atomic structure of SiC is

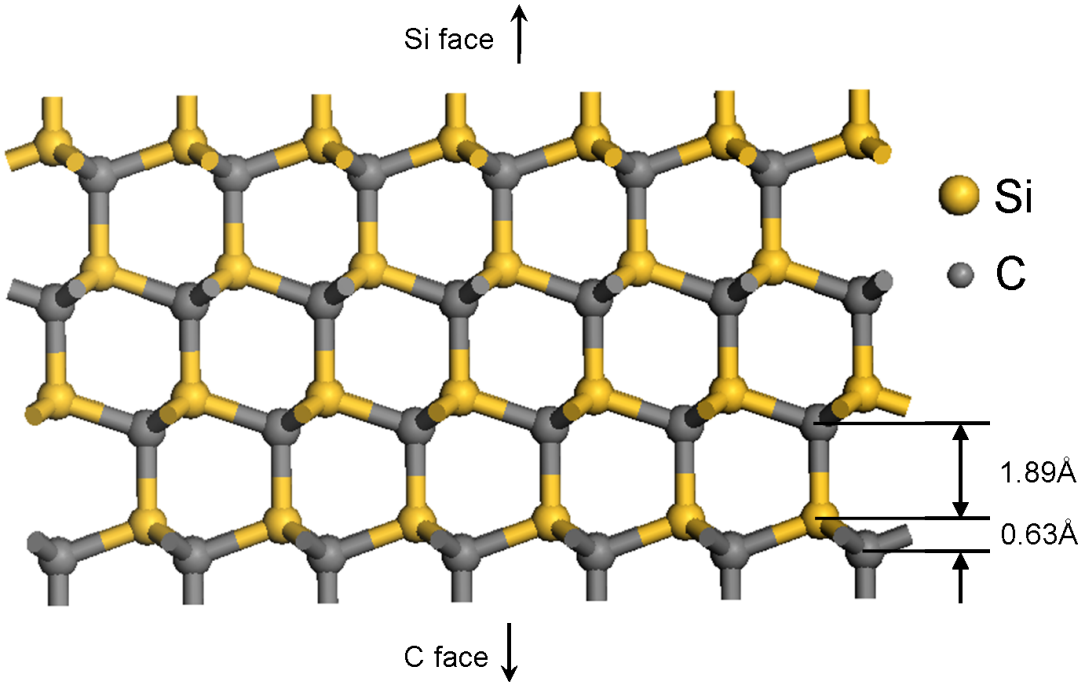

Figure 1.1. The atomic structure of SiC crystal.

often described by Si-C bilayers stacked perpendicularly to the bilayer plane (figure 1.1) with the inter-bilayer distance at 1.89Å and the intra-bilayer distance at 0.63Å. From the view above the SiC surface, the stacking of bilayers is similar to the fcc structure, containing three equivalent stacking sites shown in the inset of figure 1.2.

After accommodating the first bilayer at the site "A", the second bilayer has a choice to sit at either the site "B" or "C". The third bilayer may choose either "A" or "C" or "A" or "B" depending on the choice of the second bilayer. This gives rise to a variety of stacking sequences in the crystal structure of SiC. In crystallography, this difference in stacking sequences is called polytypism.[2] More than 200 polytypes in the SiC bulk structures have been determined.[3] Among all polytypes, three of them (3*C*-SiC, 4*H*-SiC and 6*H*-SiC) are commonly observed and thus widely studied. The

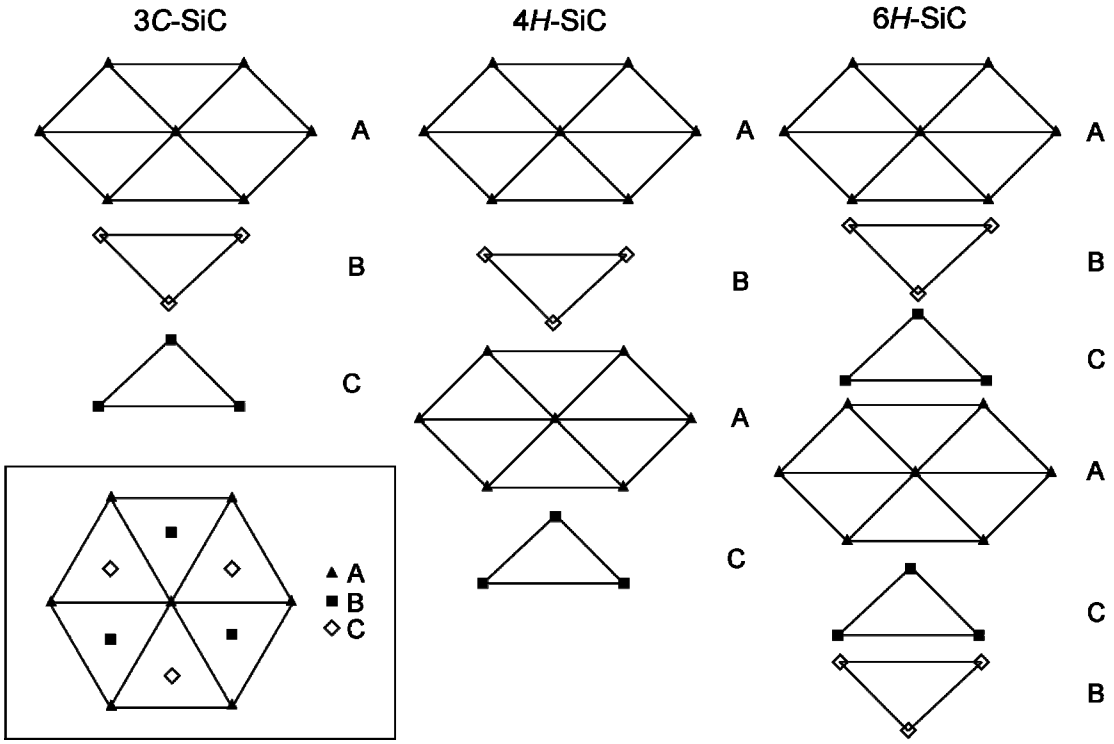

Figure 1.2. The stacking sequence of SiC bilayers in three polytypes: 3*C*-SiC, 4*H*-SiC and 6*H*-SiC. The lateral position of bilayer A, B and C is shown in the inset.

stacking sequences of 3*C*-SiC, 4*H*-SiC and 6*H*-SiC are schematically shown in figure 1.2. The SiC surfaces can be cut from either side of the Si-C bilayer, giving rise to either Si termination or C termination on the surfaces. As shown in figure 1.1, two terminations complementarily appear on two sides of the SiC bulk and are called the

Si-face or C-face, respectively. In hexagonal SiC crystals, the Si-face and C-face are denoted by (0001) and $(000\bar{1})$, respectively.

Owing to its wide band gap and thermal stability, SiC is a promising semiconductor for electronic applications in harsh environments.[4-7] For example, the high breakdown field of SiC makes it suitable for high voltage applications. The high thermal conductivity and wide band gap of SiC enables it to operate at high power and high temperature conditions. The key properties of Si, GaAs, 3*C*-SiC, 4*H*-SiC and 6*H*-SiC are listed in table 1.1. In fact, the SiC based electronic devices are already available in market.

Table 1.1. Key properties of among Si, GaAs, 3*C*-SiC, 4*H*-SiC and 6*H*-SiC.[3, 8]

	Si	GaAs	3*C*-SiC	4*H*-SiC	6*H*-SiC
Crystal structure	Diamond	Zinc Blende	Zinc Blende	Hexagonal	Hexagonal
Lattice constant (Å)	5.4310	5.6532	4.3596	a=3.0730 c=10.053	a=3.0806 c=15.117
Band gap (eV)	1.12	1.42	2.40	3.29	3.10
Breakdown field (V/cm)	3×10^5	4×10^5	$\sim1\times10^6$	$(3\sim5)\times10^6$	$(3\sim5)\times10^6$
Thermal conductivity (W/(cm·ºC))	1.5	0.5	3.2	3.7	3.6

1.1.2 The evolution of 6*H*-SiC(0001) surface reconstructions

Due to the breaking of translational symmetry at the solid surface, atoms at the surface only have half of their coordination in comparison to those in the bulk. As such, surface atoms normally undergo self-rearrangement both in-plane and out of plane to minimize their surface energy. This rearrangement is known as a *surface reconstruction*. The reconstructed surface may show very different structural and

electronic properties from bulk materials. Thus, studies of surface reconstructions have a fundamental importance for a particular surface. The knowledge obtained from these studies serve as the basis for all other application-level studies.

Among all reconstructions observed on SiC surface, a series of reconstructions on (0001) face evolving from the silicon-rich 3 × 3, √3 × √3R30°, carbon-rich 6√3 × 6√3R30° (or SiC nanomesh) to 1 × 1 graphene have been extensively studied over the past two decades.[1, 9-15] One common point in the evolution is that all these reconstructions are driven by the thermal desorption of surface silicon atoms. Due to the structure similarity, this evolution is also observed among 3*C*-SiC(111), 4*H*-SiC(0001) and 6*H*-SiC(0001) surfaces. In this thesis, the 6*H*-SiC(0001) sample is investigated as the model system.

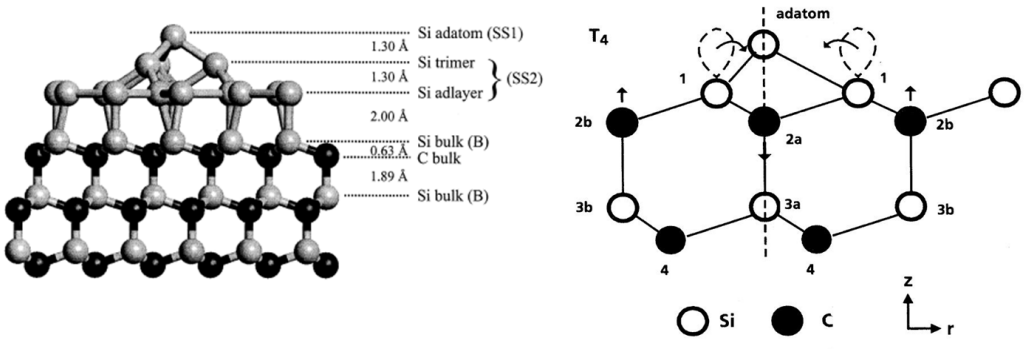

Figure 1.3. Atomic structures for SiC 3 × 3 reconstruction (left)[16] and SiC √3 × √3R30° reconstruction (right).[17]

Among all four surface reconstructions in the evolution, the first two are well understood but the later two are still controversial. This evolution begins from the silicon-rich 3 × 3 reconstruction. The formation of this reconstruction requires annealing at 850─1000°C with external silicon flux.[11, 13, 15] This reconstruction is

described as silicon adatom + silicon trimer on top of a twisted silicon adlayer, containing $1\frac{4}{9}$ layer of excessive silicon atoms on the outermost silicon carbide bilayer (figure 1.3 left panel).[18, 19] Owing to the presence of silicon dangling bonds, this reconstruction is reactive to various adsorbates.[20-23] The subsequent √3 × √3R30° reconstruction is prepared either by annealing the SiC 1 × 1 or 3 × 3 reconstructions at 950°C to 1000°C without silicon flux.[24-26] This reconstruction is described by a silicon adatom on top of the T_4 site of bulk SiC (figure 1.3 right panel).[17] Therefore, this reconstruction is still silicon rich but only has $\frac{1}{3}$ layer of excessive silicon atoms. Similar to the previous reconstruction, the √3 × √3R30° reconstruction is also reactive to adsorbates.[27]

Unlike the first two reconstructions in this evolution, the third is carbon rich, as confirmed by AES, XPS and other surface analytical techniques.[9, 10, 15, 28] This reconstruction can be obtained by subsequent annealing of √3 × √3R30° reconstruction at the temperature between 1050°C and 1150°C.[10, 26] Based on its LEED patterns, this surface was initially referred to as the 6√3 × 6√3R30° reconstruction.[10] However, Owman *et al.* studied this LEED pattern and interpreted it as the combination of 6 × 6, 5 × 5 and √3 × √3.[26] Riedl *et al.* argued that the 6√3 × 6√3R30° did exist although the 6 × 6 and 5 × 5 reconstructions also played an important role in their interpretation of this LEED pattern.[29] Therefore, the name "6√3 × 6√3R30°" is controversial or at least insufficient to represent this surface structure. However, many authors continue to use this name for consistency. Meanwhile, STM studies of this reconstruction suggest a different structure. Li *et al.*

revealed a 6 × 6 honeycomb-like topography on this reconstruction.[15] Owman *et al.* also observed 5 × 5 patterns on this surface.[26] However, no direct observation of $6\sqrt{3} \times 6\sqrt{3}R30°$ periodicity has been confirmed in STM studies. Chen *et al.* discovered that the diameters of honeycomb cells were dependent on the annealing time, and called this surface reconstruction a "carbon nanomesh" based on its topography in STM.[28] In this thesis, we discover that the silicon atoms, although deficient at surface, do exist in this reconstruction and may play an important role in these atomic structures. Thus, the name "carbon nanomesh" is not accurate to describe this surface and the term "SiC nanomesh" will be used in this thesis to give a better interpretation to this surface.

The last reconstruction in this evolution is 1 × 1 graphene, prepared by the annealing of previous reconstruction at 1200°C or higher.[10, 30] At such temperatures, the surface continues to graphitize due to silicon desorption and eventually transforms into epitaxial graphene (EG). Although this graphene structure was observed by Van Bommel and his coworkers at 1975, it did not attract much attention until Novoselov and his coworkers discovered the novel properties of graphene exfoliated from HOPG sample.[31-33] Later on, experimental studies confirmed that the EG on SiC exhibits similar properties with the exfoliated graphene.[34-36] Due to the convenience of its preparation method, EG on SiC becomes an important platform for the exploration and characterization of the graphene properties.[37-41] However, the properties of EG layer are slightly different from exfoliated graphene due to the interactions to its supporting layer, the SiC

nanomesh, which can be observed as a 6 × 6 modulation to the graphene networks.[34, 42] These interactions not only give rise to the 6 × 6 modulation to the graphene networks, but also alter the electronic structure by electron doping which moves its Fermi level 0.3eV upwards from its Dirac point.[39, 43] Thus, knowledge of the SiC nanomesh is needed to fully understand the properties of EG. The interaction between EG and SiC nanomesh also affects the formation of EG layers. Different growth mechanisms based on experimental observations are suggested, but the lack of understanding about the atomic structure of the SiC nanomesh hinders further evaluation of these assertions.[42, 44-48] Thus, as the least understood surface structure, the study of the SiC nanomesh not only provides understanding to this unique reconstruction but also helps us understand the properties of EG.

1.1.3 The SiC nanomesh

The discovery of the SiC nanomesh was attributed to Von Bommel and his coworkers who observed this surface in LEED for the first time.[10] From the AES data, they revealed the richness of carbon atoms and speculated this reconstruction to be a graphene layer on top of SiC bilayer. This is not surprising because the superstructure with unit cell $6\sqrt{3}$ times the SiC lattice is commensurate with the graphene lattice. Based on this fact, many models were developed to explain how the graphene layer is bonded to the substrate. The first and the simplest model proposed a graphene layer above SiC 1 × 1, with no covalent bonding.[49] However, XPS studies challenged this model as the graphene signal appeared at temperatures much higher

than SiC nanomesh formation.[9] Another subsequent study by momentum-resolved inverse photoemission spectroscopy (KRIPES) techniques observed the carbon π^* states which was the clear evidence for sp^2 hybridized carbon at temperatures as low as 1080°C.[50] Thus, sp^2 hybridized carbon does exist in SiC nanomesh though it is not in the form of graphene. This is further confirmed by Emtsev *et al.*, who did the angular-resolved photoemission spectroscopy (ARPES) study of SiC nanomesh and graphene, revealing that the characteristic linear dispersion around Dirac point of EG (or "free" graphene) appears in 1 × 1 graphene while SiC nanomesh only showed several localized states close to the Dirac point.[51] Recently, an intercalation of hydrogen atoms through graphene and SiC nanomesh layer showed that the SiC nanomesh transforms into a graphene layer after hydrogen intercalation.[52, 53] These results imply that the SiC nanomesh should have structure similarities to graphene network as it can be reversibly transferred into graphene form by hydrogen intercalation. Cross-sectional TEM study of SiC nanomesh and EG also supports this assertion as both SiC nanomesh and graphene have similar lamella structure except the different in interlayer spacing.[54] As a result, the SiC nanomesh is regarded as a pseudo-graphene layer with covalent bonding to the SiC substrate (figure 1.4a).

Several atomic models of the SiC nanomesh explaining how this pseudo-graphene layer is bonded to the substrate have been proposed. As the $6\sqrt{3} \times 6\sqrt{3}$ lattice is too large to give practical information by calculation, graphene network bonds to the silicon dangling bonds of $\sqrt{3}$ reconstruction is proposed.[55, 56] Without

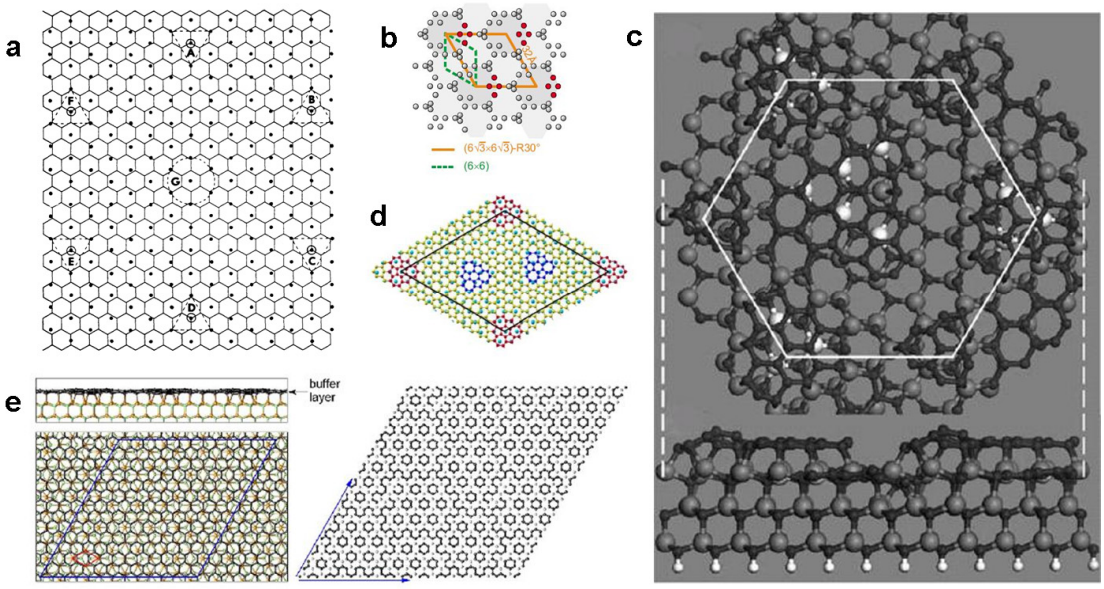

Figure 1.4. Structure models of SiC nanomesh. a, graphene network on SiC (0001);[49] b, phenomenological model to explain 6√3 periodicity on 6 × 6 honeycombs;[29] c, graphene nanoisland model;[28] d, pentagon and heptagon rings model for SiC nanomesh;[57] e, covalent bonding model.[58]

involving the large unit cell of 6√3 × 6√3, this model with a √3 unit cell provides a feasible basis for practical calculations. However, the calculation based on this model could only provide some preliminary results due to the over simplification and thus unable to explain the 6√3 periodicity and the complex structures in the SiC nanomesh. Later on, models based on experimental evidence were brought out to explain the SiC nanomesh. Chen *et al.* proposed that SiC nanomesh contains 6 × 6 periodic graphene nanoislands (figure 1.4c).[28] However, the 6 × 6 periodicity was not been observed by ARPES. Riedl *et al.* also proposed a phenomenological model in which the honeycomb-like cells with "6 × 6" periodicity possess two different sizes, giving rise to a 6√3 × 6√3 periodicity (figure 1.4b).[29] Using the same approaching, Kim *et al.* proposed a detailed SiC nanomesh model by covalent bonding of the graphene layer

to the SiC 1 × 1 substrate (figure 1.4e).[58] Recently, Qi *et al.* further suggests the top layer not only contains hexagon rings but also pentagon and heptagon rings (figure 1.4d).[57] Although these models successfully shows a 6√3 × 6√3 periodicity by dividing 6 × 6 honeycomb cells into two different sizes, these models also contain many inconsistencies from the experimental observations.[28, 29] As carbon atoms in SiC nanomesh are believed to form a graphene-like framework, the possible role of silicon atoms in this superstructure has largely been ignored. Few papers studied the role of silicon atoms in the SiC nanomesh though it is known that silicon desorption is the driving force for this evolution. Ong *et al.* proposed a SiC nanomesh model using silicon clusters on the surface.[59] However, this model is unable to explain the sp^2 hybridization of carbon atoms in this surface.

Despite all the efforts, no conclusive model has been established to explain several characteristics of this unique surface. One well-known apparent contradiction is that this reconstruction shows a 6√3 × 6√3R30° pattern in LEED but a 6 × 6 honeycomb structure in STM.[10, 15] To explain this contradiction, speculative models decomposing the LEED pattern into combinations of several surface reconstructions or by creating a 6√3 × 6√3R30° periodicity by hypothesizing alternative arrangement of two different 6 × 6 honeycomb cells in STM images have been proposed.[26, 29] However, these speculations are only phenomenological explanations and need further investigation.

Another character of this surface which has been observed for long time, but receives little attention is its transition kinetics. Unlike other surface reconstructions

which show an abrupt phase transition from one structure to another, the SiC nanomesh exhibits an unusually slow transition from its preceding phase, *i.e.* the $\sqrt{3} \times \sqrt{3}R30°$ reconstruction and to its succeeding phase, *i.e.* the 1×1 graphene. The slowness of the first transition is observed in LEED whereby $6\sqrt{3} \times 6\sqrt{3}R30°$ and $\sqrt{3} \times \sqrt{3}R30°$ patterns are mixed at the beginning of SiC nanomesh formation, [26, 28] while the slowness of the second transition is observed in STM where the SiC nanomesh and graphene are observed to coexist on the same terrace during the formation of graphene layers.[38, 47, 60] Although the slow speed in the transitions can be generally attributed to the continuous loss of surface silicon atoms,[61] the relation between silicon desorption and the structural changes of the SiC nanomesh remains unclear.

The last character of the SiC nanomesh is its structure complexity which is obviously related to its unusual transition kinetics. First, at least two sub-phases (6×6 honeycomb and 5×5 cluster) are observed on this surface by STM.[26] The ratio of the two sub-phases varies depending on preparation methods and annealing temperatures. Second, its topography in STM has a highly disordered appearance. The disorder of this surface will be discussed in this thesis. In fact, it is problematic to treat the SiC nanomesh as a single surface reconstruction. Instead, we regard this surface as a collection of the surface rearrangements based on our observations.

1.2 Nanotemplates in nanotechnology research

The concept of utilizing the single molecule as the building block for electronic and other types of nanodevices is well known. It has been proposed that a single molecule could operate as a diode,[62, 63] a transistor[64, 65] or a storage unit.[66] However, to place these molecules discretely at specific atomic sites on the surface is challenging as the molecules tend to aggregate on a surface. The scanning tunneling microscope tip has been demonstrated as being able to manipulate atoms or molecules on the surface to form desired patterns.[67, 68] This serial method is slow as only one molecule can be moved each time, needing sophisticated control and having an extremely low yield. Furthermore, this method cannot eliminate the spontaneous aggregation of molecules on the surface and usually works at cryogenic temperature when the atoms or molecules are effectively frozen.

The alternative strategy is to use nanotemplates to confine molecules at specific adsorption sites and in well-ordered patterns. The advantage of this strategy is that instead of reducing the movement of molecules by freezing them, a local barrier is applied to limit the aggregation of target molecules.

The family of nanotemplates can be divided into two types by fabrication methods: natural nanotemplates and artificial nanotemplates. Many examples of artificial nanotemplates have been fabricated via several methods.[69] In figure 1.5, three typical nanotemplates made via hydrogen bonding, host-guest molecule inclusion and metal-organic coordination are shown. The middle image in figure 1.5 shows guest molecules accommodated into the cavity of host molecules, appearing as

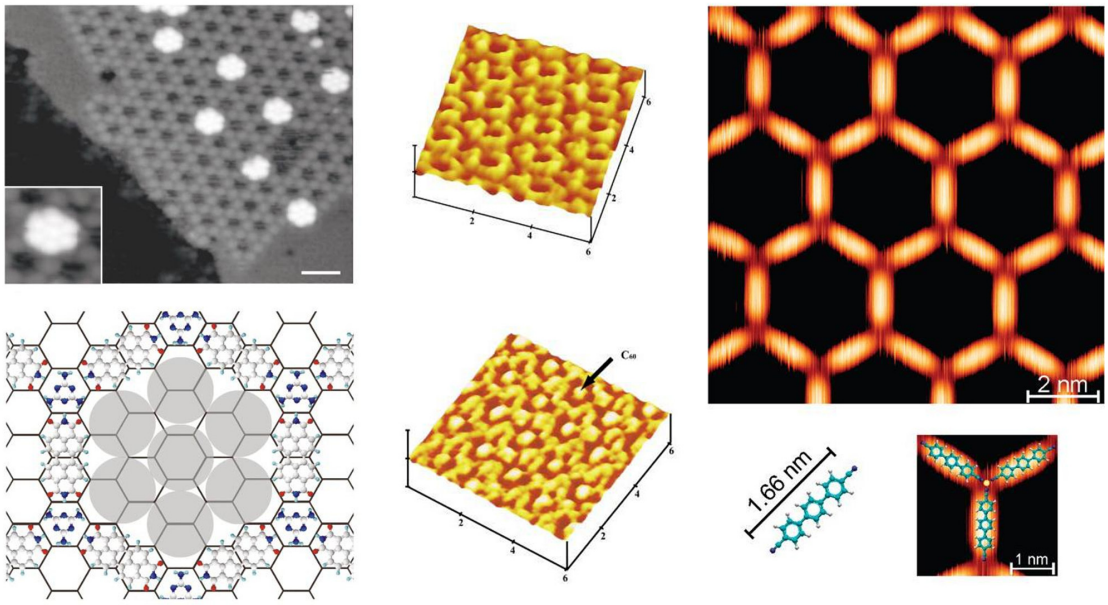

Figure 1.5. Artificially formed nanotemplates. Left, PTCDI-melamine supramolecular network via hydrogen bonding;[70] Middle, Inclusion of fullerene at the cavity of bowl-shaped calyx[8]arene molecules;[71] Right, metal-organic coordination network by Co atoms and ditopic dicarbonitrile-polyphenyl molecules.[72]

the most straightforward method. In this method, strong molecule-substrate interaction is often needed to maintain the cavity open orientation. Thus, the application of porous molecules is limited to particular substrates which are able to maintain the appropriate molecular orientation for guest molecule capture. Furthermore, the synthesis and purification of these cavity-containing molecules are generally complicated and time-consuming. The images at the left side of figure 1.5 show supramolecular networks which are constructed by small molecular components via hydrogen bonding, while images on the right show that it is driven by metal-organic coordination. [70, 72, 73]Holes in these networks are capable of accommodating various guest molecules. For instance, fullerene molecules are accommodated in the networks of perylene tetra-carboxylic di-imide (PTCDI) and

melamine.[70] However, these templates are often volatile, easily changing from one shape to another depending on the coverage and ratio of molecular components.[74, 75] Other kinds of molecular networks based on dipole-dipole interactions and Van der Waals interactions are also observed, but their networks structures are less predictable.[76]

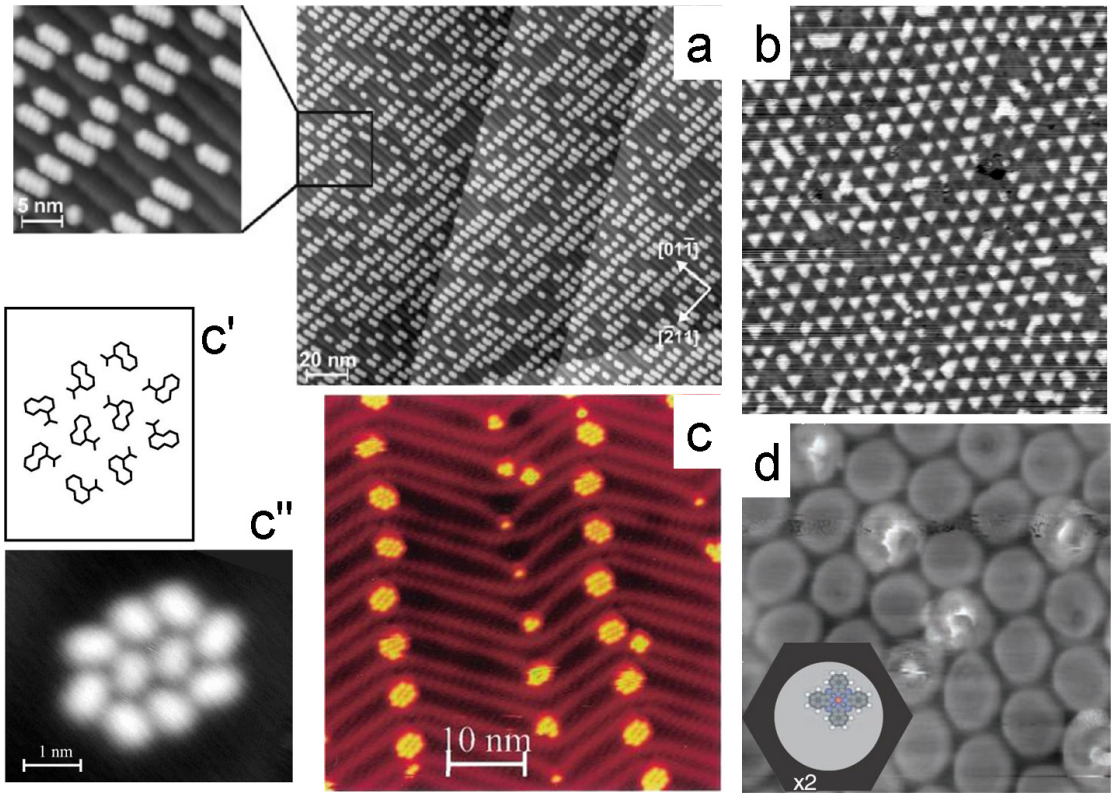

Figure 1.6. Naturally formed nanotemplates for molecular assembly. a. C_{60} chains on Au(788) vicinal surface;[77] b. Fe islands on Cu/Pt(111) strain-relief pattern;[78] c. 1-nitronaphthalene (NN) on Au(111) reconstructed surface;[79] c' and c'' show internal structure of one NN cluster; d. CuPc atoms attracted in BN nanomesh.[80]

Naturally formed nanotemplates have also been studied for a long time. In figure 1.6, several reported nanotemplates including vicinal surfaces,[77, 81] strain-relief patterns,[78] surface reconstructions,[79] and corrugated surfaces[82] are shown. These nanotemplates exhibit good stability compared to supramolecular structures.

One good example is the boron nitride (BN) nanomesh.[82] With the 2 nm hole and the 3.2 nm lattice constant, it is successfully demonstrated as a potential template to trap single molecules or atoms inside its "holes".[80, 82, 83] The SiC nanomesh, which exhibits honeycomb-like surface corrugation in STM images, is a potential candidate as a natural nanotemplate. The pioneering study of the template effect of SiC nanomesh was done by Chen *et al.* in our group who observed a dispersive distribution of Ni clusters on this surface due to dewetting.[84] Poon *et al.* repeated this experiment on a SiC nanomesh/graphene surface using Co atoms.[60] Co atoms also aggregated into dispersive clusters preferentially attached to the SiC nanomesh. These dispersive metal clusters reveal the template effect of SiC nanomesh. However, the template effect via organic molecules has not been carried out prior to this work. In this thesis, the absorption of organic molecules on the SiC nanomesh is studied by STM and XPS. The results reveal that the SiC nanomesh could serve as an effective nanotemplate for selected organic molecules.

1.3 Intercalation and chemical reactions at the graphene surface

The phenomenon of adsorbates intercalating at monolayer graphite/metal surfaces has been known for a long time. Rare earth, alkali metal, noble metal, transition metal and even some organic molecules such as fullerene [85, 86] can be intercalated at various metal/monolayer graphite surfaces. This phenomenon can be partially understood by the weak interactions between EG and metal surface. Several

studies of this phenomenon using angle resolved ultraviolet photoemission (ARUPS), high resolution electron energy loss spectroscopy (HREELS) and Auger electron spectroscopy have been previously reported.[87, 88] Since the recent interest in controlled monolayer epitaxial graphene (EG) growth, intercalation at EG interfaces has been revisited.[89] Due to the outstanding electronic optical, mechanical, and thermal properties of graphene,[35, 90] the engineering of graphene to fit device requirements by fabricating graphene nanoribbons and adding functional layers such as dielectric layers are proposed. The phenomenon of intercalation provides another graphene engineering route by intercalation of an external layer at the bottom of the graphene layer.

Unlike the intercalation of EG on metal surfaces, which is well understood, the intercalation of EG on SiC has been investigated by only a few groups. Riedl *et al.* observed a reversible hydrogen atom intercalation of EG on SiC by means of ARUPS.[52] Furthermore, Virojanadara *et al.* found that monolayer graphene and the nanomesh layer can be transformed into bilayer graphene by atomic hydrogen in a reversible manner.[53] Both studies suggest the chemical reactions between adsorbates and the SiC nanomesh occur after intercalation. Thus, the intercalation and subsequent chemical reactions at the interface should be carefully studied to understand this phenomenon. Our study further reveals that silicon atoms are involved in the chemical reactions with adsorbates at the EG/SiC interface region.

1.4 Research objectives

To understand the atomic structures of a surface is always the primary task in surface science. This understanding serves as the starting point for the studies of other surface related phenomena, such as absorption, reaction, diffusion and etc. Since its discovery from three decades ago, the SiC nanomesh surface has yet to be fully understood. Due to its large unit cell (108 times of the unit cell of SiC) and more critically, the defective appearance in STM observations, the proposed models of this surface has failed to achieve complete agreement with experimental observations to date. According to its carbon richness, most studies ignore silicon atoms and build their models solely based on carbon atoms. However, the richness of carbon atoms does not necessarily preclude silicon atoms in this rearranged layer. In the evolution from the SiC nanomesh to graphene, silicon atoms are continuously desorbed from the surface, which also imply that there should be a certain amount of silicon atoms at the surface for desorption.

In this thesis, special attention has been paid to the Si atoms in the study of the SiC nanomesh structure. In chapter 3, the local environment of silicon atoms in the bulk of SiC and at the surface region is studied by XAS. Complementary XPS and STM studies are also done to give an in-depth understanding of surface disorders. In chapter 4, oxidation of the SiC nanomesh is investigated at elevated temperature. The results show a transition of SiC nanomesh to EG by oxidation which provides a novel way to study the formation of EG. This study also reveals the importance of silicon atoms in the transition from the SiC nanomesh to EG.

In chapter 5, the SiC nanomesh is used as a nanotemplate for the adsorption of three organic molecules, namely fullerene (C_{60}), copper phthalocyanine (CuPc) and pentacene. Two of them (CuPc and pentacene) exhibit regulated growth on this SiC nanomesh but not C_{60} due to its weak molecule-substrate interactions. In chapter 6, the intercalation of graphene layer by oxygen molecules and iron atoms are studied. The results confirm the intercalation effects of both adsorbates. Furthermore, chemical reactions with silicon atoms at the interface are observed, suggesting a reactive intercalation phenomenon of epitaxial graphene on the SiC substrate.

CHAPTER 2 EXPERIMENT

In this chapter, experimental details regarding this work are discussed. Photoemission based techniques including XPS, UPS, and XAS are reviewed in section 2.1. Other surface analytical techniques including STM and LEED are introduced in section 2.2. Experimental systems and synchrotron facilities are described in section 2.3. The sample preparation and other experimental details are addressed in section 2.4.

2.1 Photoemission spectroscopy (PES)

2.1.1 X-ray photoelectron spectroscopy (XPS)

X-ray photoelectron spectroscopy measures the kinetic energy distribution of emitted photoelectrons excited by incident X-ray photons from a substance.[91] The origin of this technique can be traced back to the photoelectric effect, first observed by Heinrich Hertz in 1887. Albert Einstein introduced the quantum concept to explain this effect in 1905 which won him the Nobel prize in 1921.[92] However, measurements based on the photoelectric effect were not extensively utilized to study the materials due to the lack of capability to resolve the kinetic energy of electrons by a spectrometer. Modern XPS techniques appeared in the 1970s when high resolution electron spectrometers became available. XPS is also called electron spectroscopy for chemical analysis (ESCA) in chemistry to emphasize its ability in element

identification. Presently, the XPS techniques have become so widespread that they are used in many research frontiers.

The fundamental principle of the photoemission process is the energy conservation law where incident photon energy ($h\nu$) equals to the sum of emitted electron kinetic energy (E_K), the work function of sample (Φ_S) and the binding energy of this electron (E_b).

$$h\nu = E_b + E_K + \Phi_S \tag{2.1}$$

By the measurement of E_K, the binding energy of photoelectrons can be calculated. The obtained binding energy can be used to determine the elemental identification of atoms and to study the local chemical environment of atoms. However, the real photoemission process is much more complicated than this simple description. First, the emission of core electrons also causes the relaxation of remaining electrons in the same atom, affecting the kinetic energy of photoelectrons. The only exception is the hydrogen atoms or hydrogen-like systems such as He^+, which only has one electron in its system. This many-body effect can be quite complicated when the system has many valence electrons. For example, emitted photoelectrons could liberate another electron from valence band to vacuum (shake-off) or bound state (shake-up) and lose some of its kinetic energy. For solid sample, the excited photoelectrons need to propagate to the surface before ejecting to vacuum. One commonly used model splits the complicated photoemission process into three independent processes: optical excitation between two Bloch states, propagation of excited electron to the surface and escape of electron from the surface into vacuum.[93] As a result, each step can be

treated separately and the total photoemission intensity is given by the product of probabilities associated with each step. The optical excitation of an electron is described by Fermi Golden rule transition probability,[94] which is dependent on $\left|\langle f,k|H|i,k\rangle\right|^2$ where $|i,k\rangle$ and $\langle f,k|$ are initial and final states with negligible change in wavevector *k*. The perturbation operator *H*, is defined as: $H=\frac{e}{2m}(A\bullet p+p\bullet A)$ where *A* is the vector potential of the incident light and *p* the momentum operator. As the final states of photoelectrons are continuum states, their energy distribution is reproduced from the density of state (DOS) of occupied initial states.

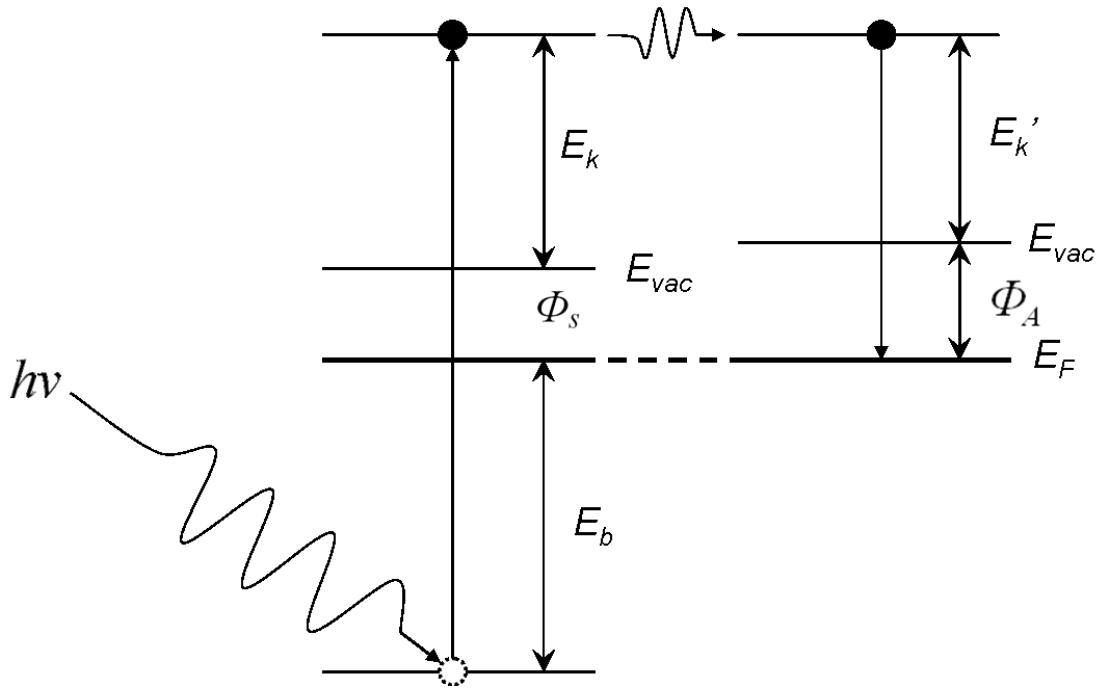

Figure 2.1. Schematic energy diagram for the emission and detection of photoelectron.[95]

In practical measurements, the photoelectron spectrum or energy distribution curve (EDC) is obtained by sweeping the kinetic energy of photoelectrons in a certain range and keeping the photon energy constant. However, the E_k of emitted

photoelectrons relative to sample vacuum level E_{vac} is not reachable; instead, the E_k' relative to electron spectrometer is measured (figure 2.1). Thus, the binding energy of photoelectrons in acquired EDC is revised as:

$$E_b = h\nu - E_K' - \Phi_A \qquad (2.2)$$

In this equation, E_b is the binding energy of emitted photoelectrons defined to be the separation in energy between its initial energy state and the Fermi level in the material; $h\nu$ is the photon energy of incident photons; E_K' is the kinetic energy measured in EDC; Φ_A is the work function of the electron spectrometer. Due to the emission of electrons, the material is positively charged and the kinetic energy of emitted electrons is retarded by this self-generated positive electrical field. Thus, sample grounding or more specifically Fermi level alignment between the sample and the spectrometer is the prerequisite to achieve precise measurement of kinetic energies.

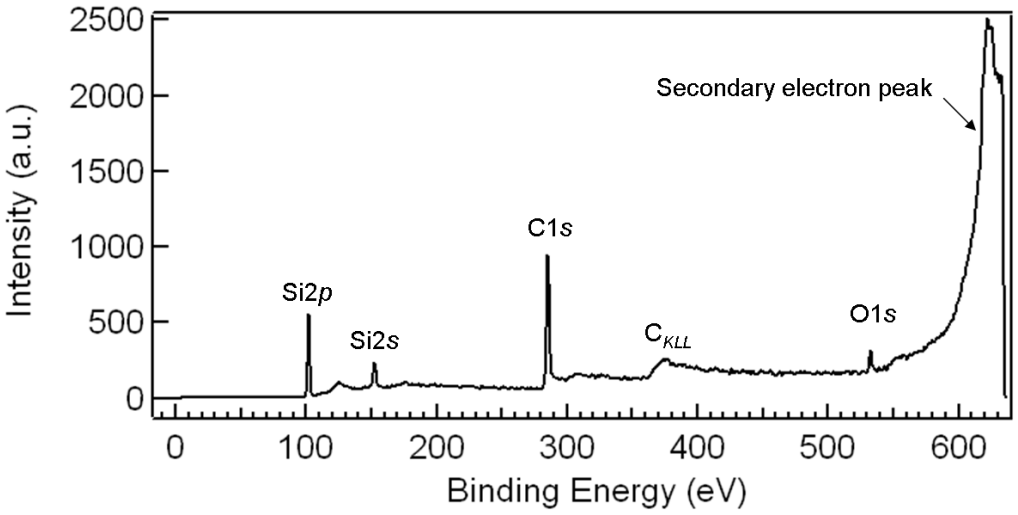

Figure 2.2. An energy distribution curve of SiC nanomesh after oxidation with photon energy set to 650eV.

A typical wide range EDC of an oxidized SiC sample at photon energy 650eV is shown in figure 2.2. This curve consists of three features: a broad featureless peak at high binding energy, several element-specific sharp peaks and one bump indicating the C_{KLL} Auger peak of the sample. The first feature is the secondary electron peak, which is attributed to secondary excited electrons generated by inelastic scattering process during propagation of photoelectrons. The second feature is attributed to the photoelectrons which conserve their initial kinetic energies. These sharp peaks have a *Lorentzian* shape and their intensities are proportional to the photoionization cross section of elements. The last feature is attributed to the Auger process, where relaxation of the excited final state causes one outer shell electron to jump into an inner shell hole, exciting another outer shell electron to vacuum.

The element-specific core level peaks are the focus of XPS studies. First, these sharp peaks are from localized core levels with unique binding energies for different elements. Thus, XPS can be used to verify the presence of different elements. With appropriate considerations of photoelectron escape depths and photoionization cross sections, quantitative information of relative concentration of different elements can be acquired. Second, core-level peaks of the same element situated in different chemical environments show small shifts in binding energy. These binding energy shifts are called chemical shifts reflecting the degree of loss or gain of valence electrons of specific elements in the compound. These shifts may also be observed at the surface due to the symmetry breaking (dangling bonds) and reconstructions. Third, core level shifts also carry information on final state effects. At the high-energy

photoelectron limit, the response of the system to the creation of a hole is very small, and final state effects such as relaxation and screening are neglected. However, if the limit is not satisfied (low energy photoelectron limit), the final state effect can have a strong influence on the core level binding energy. Thus, the photoemission peaks provides information on how system responds to final state perturbations.

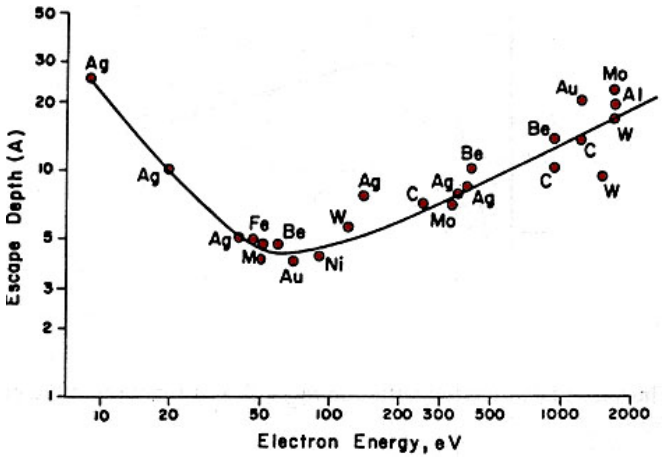

Figure 2.3. The escape depth (IMFP) of electrons in different materials as a function of kinetic energy.[96]

The surface sensitivity of XPS is an important advantage for surface studies. In the three-step model, photoelectrons need to travel to the surface before escaping. During this propagation, the electron has a certain probability to lose energy due to inelastic scattering. This probability is a function of electron kinetic energy and can be described by the energy-dependent inelastic mean free path (IMFP) of the electron, showing as the so-called "universal curve" in figure 2.3. Between 20−200eV, the escape depth of electrons is at a minimum smaller than 1nm, indicating a probe depth of less than several atomic layers. In addition, the surface sensitivity can be further enhanced by collecting photoelectrons at grazing angles.

2.1.2 Ultraviolet photoelectron spectroscopy (UPS)

In principle, X-ray photons which are used to excite inner shell electrons can also excite valence electrons during XPS measurements. However, low-energy photons from discharge lamps or synchrotron storage rings are used more often to obtain UPS spectra due to two notable reasons. First, the high energy photons from an X-ray gun or a storage ring do not achieve high energy resolution compared to low energy photons, which basically hinder the resolving of the fine structures in the valence band. For example, the energy resolution can easily reach a few meV using Helium I (21.2 eV) or Helium II (40.8 eV) in UPS spectra. For synchrotron based UV photons, the energy resolution is dependent on the design of optics; however, resolution better than tens of meV is easily achieved. In this thesis, the synchrotron based UPS measurements have an energy resolution better than 0.05 eV. Second, high photon energy means small absorption cross section, which limits the intensities of UPS signals using X-rays. Therefore, UPS spectra normally refer to measurements using photon energies from several eV to 200 eV.

The inner shell electrons, which sit deep inside the nuclei potential wells, are strongly localized around the nuclei with discrete binding energies. Although they can "feel" the changes in the surrounding electrical field by presenting a small binding energy "shift", the binding energies of core shell electrons are largely determined by the nuclei fields and are thus elemental specific. The outer shell electrons, on the contrary, are weakly bound by the nuclei potential wells and extend far from the nuclei. These electrons lose their elemental characteristics due to heavy hybridization

to form the valence band. As the valence band is sensitive to the chemical reactions and other subtle interactions at surface and interface, the understanding of the valence band structure is very important in many surface related studies such as surface states, charge transfer and chemical reactions. For example, UPS spectra are widely used to probe the DOS of the sample valence band.

According to the band structure of a solid, the binding energies of valence electrons depend on their momenta. Due to the conservations of energy and momentum in the photoemission process inside the solid, the excited photoelectrons from valence bands carry information which can be used to map the band structure of the sample. For that purpose, angle-resolved UPS records the kinetic energy and emission angles of valence band photoelectrons. However, when photoelectrons are emitted into the vacuum from the sample surface, only its momentum parallel to the surface ($k_{\parallel}$) is conserved but not those which are perpendicular to the surface ($k_{\perp}$). Therefore, the band structure measured by ARUPS is actually the 2D k space projected from the real 3D space. In principle, $k_{\perp}$ can be obtained from $k_{\parallel}$ and E(k) using the energy conservation law. Thus, ARUPS is capable of probing the band structures of many crystals, especially for 2D crystals such as graphene[36, 39, 51] and copper-oxide perovskite crystals.[97]

Another simple but important application of UPS is to determine the work function of samples (Φ_S). In figure 2.4, the UPS curves before and after detection is shown in between of E_{vac} and E_{max}. In figure 2.4a, photoelectrons which have a kinetic energy less than Δ (which is the work function difference between the sample and the

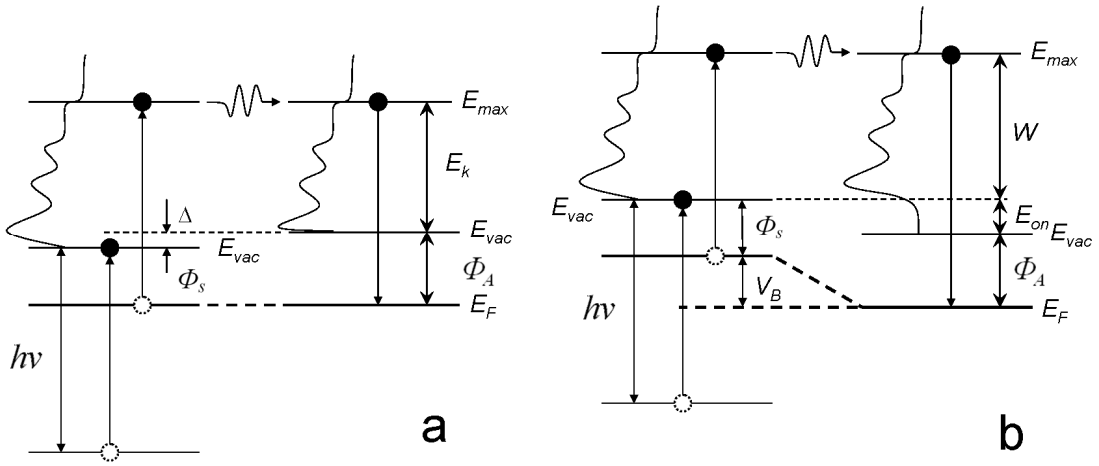

Figure 2.4. The energy diagram in work function measurement. a. energy diagram for unbiased sample and electron analyzer. A work function offset Δ is shown in graph to show the incorrect onset of low energy photoelectrons. b. energy diagram for sample with bias V_B. relative to the electron analyzer The correct E_{on} can be detected by analyzer.

analyzer) will fail to overcome the vacuum level barrier to reach electron analyzer. Therefore, the onset of UPS curve measured by electron analyzer cannot be used to determine Φ_S. If a negative bias (V_B) is applied to the sample, 5 V for example, the energy levels of the sample are upwards shifted (figure 2.4b). The work function of sample shown as the onset of low kinetic energy photoelectrons (E_{on}) becomes detectable for analyzer. Therefore, the work function of sample can be deduced from the following equations:

$$\Phi_S = \Phi_A + E_{on} - V_B \qquad (2.3)$$

For semiconductor samples, which have no DOS at the Fermi level, the work function obtained is relative to the virtual Fermi level. Thus, the determination of the ionization potential (IP) defined as the energy difference between the highest occupied molecular orbital (HOMO) and vacuum level is often needed instead of the

work function. The value of IP can be obtained by the same measurement similar to that for work function as IP = $h\nu$ ─ W, where W is the spectral width. (figure 2.4b)

2.1.3 X-ray absorption spectroscopy (XAS)

Unlike XPS, which only studies the outgoing excited photoelectrons, X-ray absorption spectroscopy exploits the consequence of photon absorption including emission of photoelectrons and other secondary electrons to study sample properties. This absorption probability can be described by the X-ray absorption cross section σ_x, defined as the number of photoelectrons excited per unit time divided by the number of incident photons per unit time per unit area.[98] The cross section can be calculated from the Fermi Golden Rule as follows:

$$\sigma_x = \frac{2\pi}{F\hbar} |< f | \overline{V} | i >|^2 \, Q_f(E) \qquad (2.4)$$

where F is the photo flux, $|i>$ and $|f>$ the initial and final state of electron, $\overline{V}$ the perturbation operator and $Q_f(E)$ the energy density of final states. The final state of photoelectrons can be a bound or continuum state. In the spectrum of σ_x versus photon energy, the cross section generally decreases with the increase of photon energy. However, at certain energies, the cross section suddenly increases, appearing as sharp edges in the spectrum. The presence of the adsorption edges is the response to a new absorption channel. The cross section slowly decreases when the photon energy increases further. In figure 2.5, a typical XAS spectrum is shown. This spectrum can be divided into two parts. From the absorption edge up to about 50eV, strong oscillations can be observed in the spectrum. In this region, structures in XAS

are dominated by the density of final states, e.g. the unoccupied states of a solid, and electron multi-scattering processes. As such, this region of the spectrum is often referred to as the Near Edge X-ray Absorption Fine Structure (NEXAFS). The curve above the NEXAFS region (50eV to 1000eV above the edge) exhibits longer range oscillations with smaller amplitude. This part of XAS is known as the Extended X-ray Absorption Fine Structure (EXAFS). In this region, absorption induced photoelectrons jump to continuum states and only contribute to a monotonically decreasing background. However, forward-propagating electron waves interfere with back scattered electron waves from its nearest neighbors (atoms) giving rise to additional oscillations in the EXAFS spectra. Using a proper mathematical model, structural information such as the bond length, coordination number can be extracted from EXAFS.

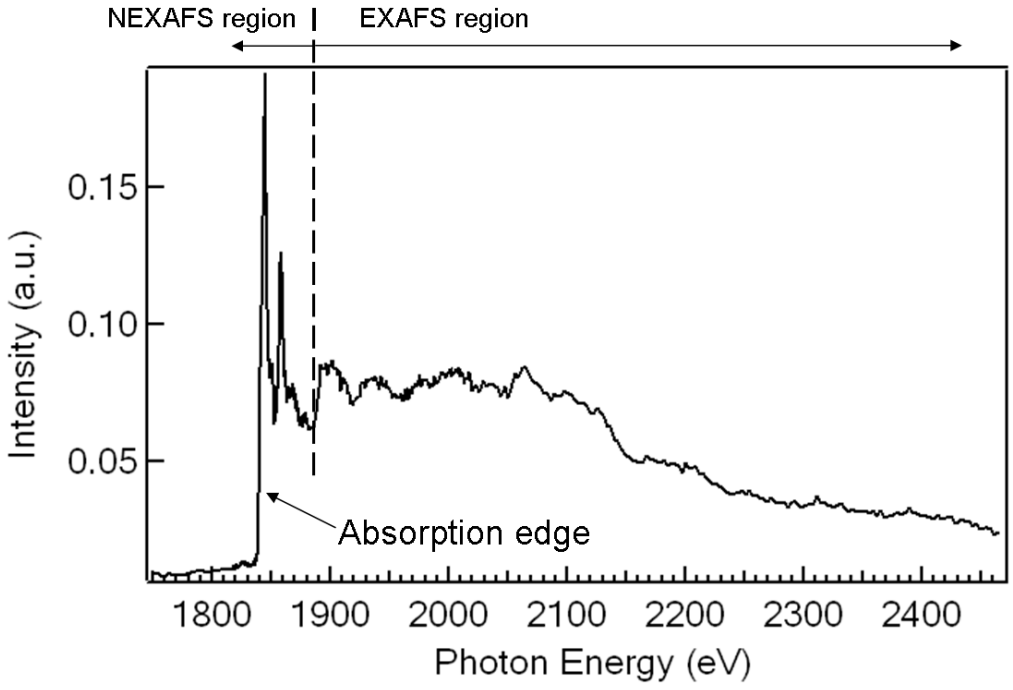

Figure 2.5. XAS spectrum at Si *K*-edge by AEY mode at grazing angle.

In XAS measurements, the change of X-ray absorption cross section (σ_x) is recorded versus the incident photon energy across the adsorption edges. As such, variable photon energy is the prerequisite of this measurement and is only available at synchrotron facilities. In experiments, either electron yield (EY) or fluorescence yield (FY) detection modes can be used to measure the change of σ_x. This is because both signals are the consequence of core-hole recombination which emits either photons or electrons. However, at low energy and for light elements, Auger electron emission dominates the recombination process while photon emission dominates at high energy and for heavy elements. As such, FY is often used in the hard X-ray region and EY is often used in the soft X-ray region. EY and FY modes show different probe depth due to shorter and longer escaping depth of electrons and photons, respectively. In FY mode, probe depth can reach several microns, which is typically dominated by bulk signals. In EY mode, probe depth is limited to several nanometers and basically surface sensitive. Thus, FY mode and EY mode can be combined if signals from different depths are of interest.

The photoelectron signals at three characteristic photon energies (pre-edge, edge and after edge) are shown in figure 2.6. All emitted photoelectrons including Auger electrons, photoemission electrons and secondary electrons contribute to the absorption signals (shown as the area marked by lines in figure 2.6b and 2.6c). However, these electrons have different probe depth and sensitivity. Photoemission electrons, which are emitted only after photon energies above hν2 in figure 2.6b usually is not suitable to be measured alone in XAS. Auger electrons have the shortest

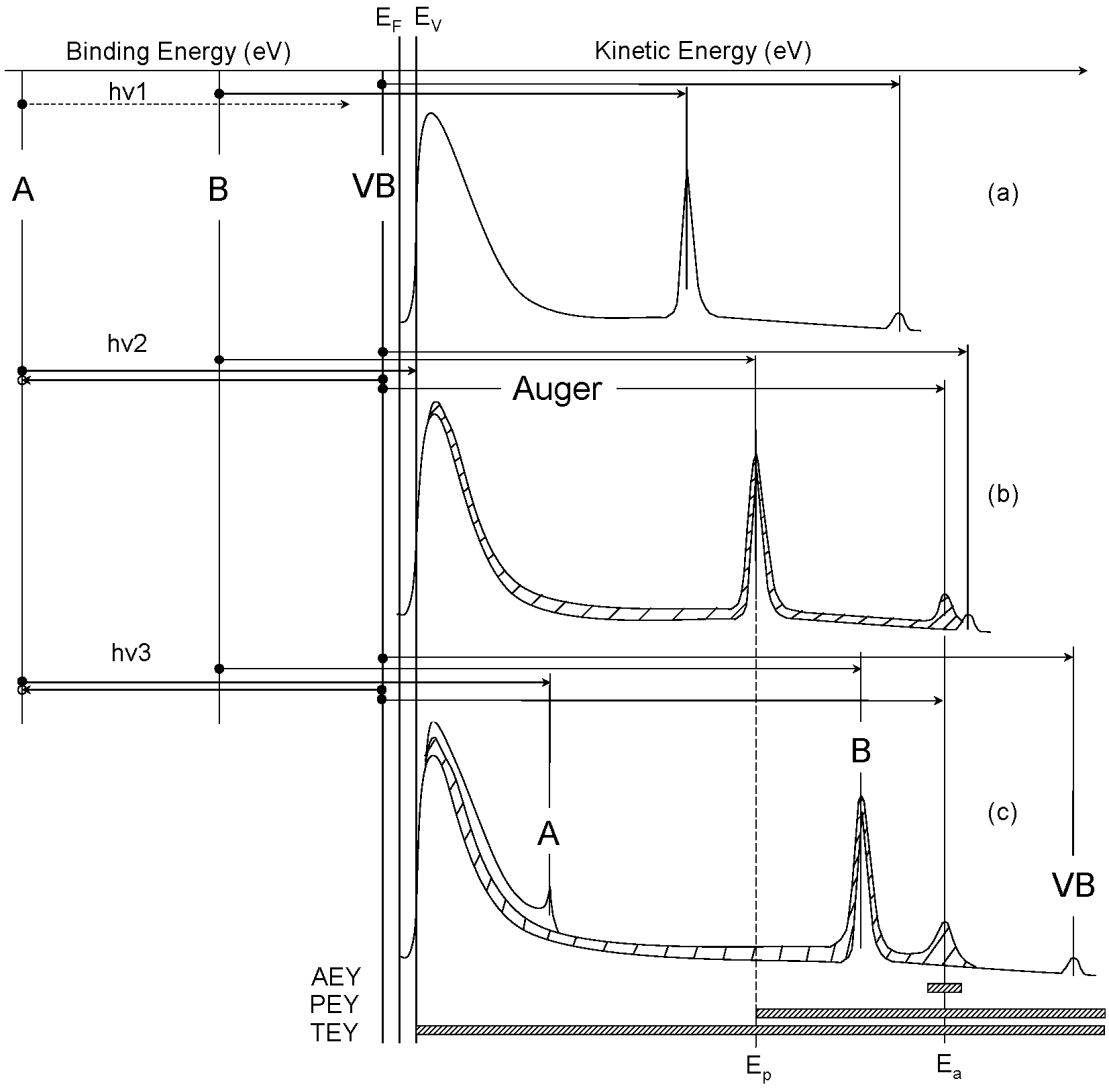

Figure 2.6. Energy level diagram and schematic photoemission spectra at different photon energies for XAS measurements. (energy axis is not in scale) a) hv1 is below threshold of core level A, only core level B and VB electrons can be excited. b) hv2 just above the absorption threshold of shell A. Auger process for core hole at shell A is allowed. c) hv3 far above threshold of shell A. TEY: all electrons are measured. PEY: electrons with higher kinetic energy than E_p are measured. AEY: only auger electrons are measured. [98]

probe depth. Secondary electrons, which are the derivates of above two types of electrons, have larger probe depth than the other two types of electrons. In experiments, three electron collection methods are often used: total electron yield (TEY), partial electron yield (PEY) and Auger electron yield (AEY). The electrons

collected based on their kinetic energies for three modes are shown at the bottom of figure 2.6. Among them, TEY is widely used due to its simplicity. This is because instead of counting all the emitted electrons, the TEY signal is obtained by measuring the photocurrent externally. In contrast, collecting of AEY signal typically involves an electron analyzer. Nevertheless, AEY signal is the most surface sensitive compared to the other two methods. The surface sensitivity of these modes increases from TEY to PEY to AEY. By applying AEY at grazing angle, selective studies of the top few surface layers can be done.

2.2 Surface analytical methods

2.2.1 Scanning Tunneling Microscopy (STM)

The invention of scanning tunneling microscopy by G. Binnig, H. Rohrer at 1981 set a new milestone in the world of nanotechnology.[99] With this technique, sophisticated manipulation, interaction and measurement down to single atoms are achieved.[67, 68] The basic principle of the STM relies on the *tunneling effect* in quantum mechanics. Electrons at the STM tip have a finite probability to tunnel through an energy barrier even if the electrons have insufficient energy to overcome this barrier. This probability is called the tunnel coefficient P and can be expressed as:

$$P = e^{(-2kd)} \tag{2.5}$$

where k is equal to $\sqrt{2m(V-E)}/\hbar$ and d is the width of barrier.

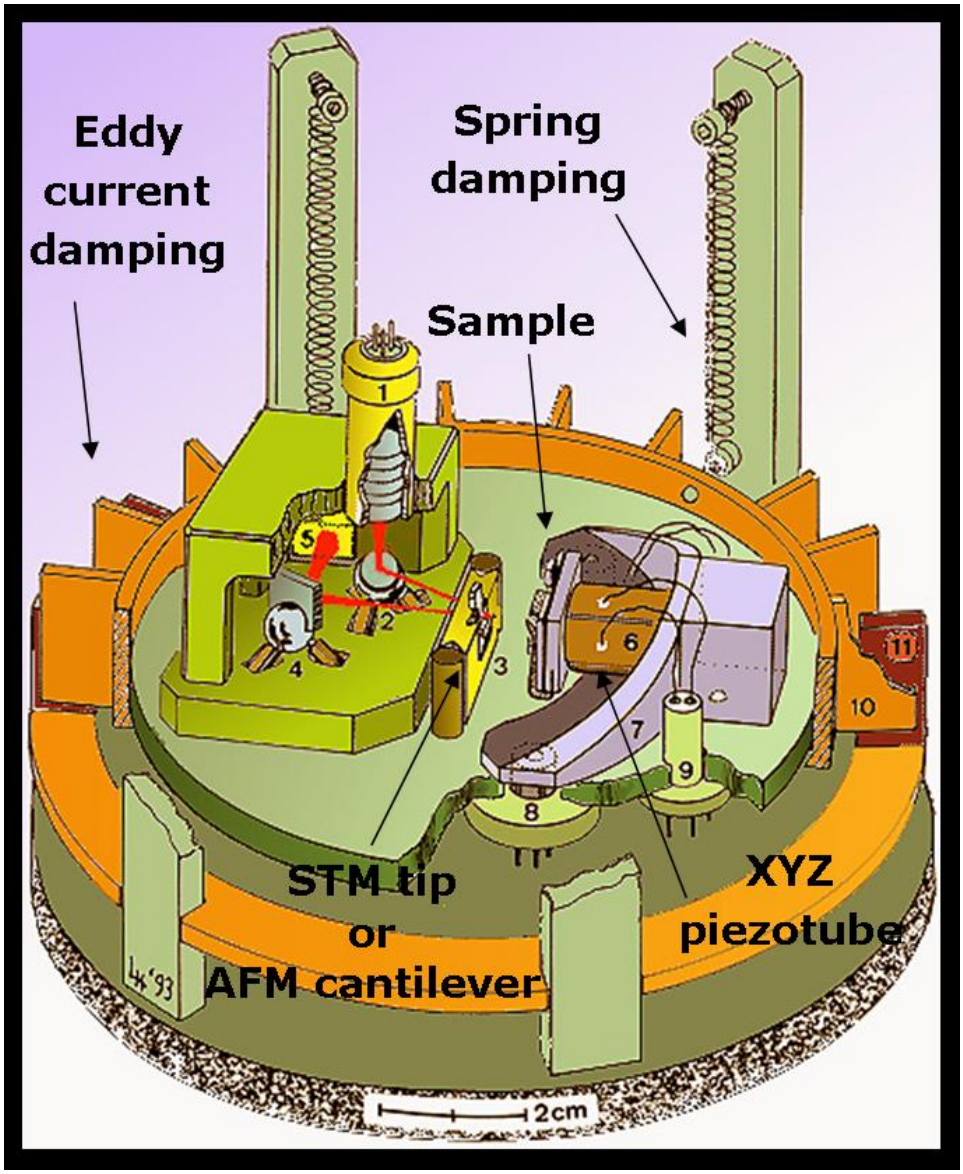

Figure 2.7. A schematic illustration of an Omicron STM/AFM system. (Originated from Purdue university, Reifenberger Nanophysics Lab)[100]

In a typical STM setup, a sharp metal tip is placed a few nanometers away from a conductive sample surface with a small bias applied between them. Electrons can tunnel through this gap to generate the tunneling current. The resulting tunneling current is a function of the width of gap, applied voltage, and the local density of states (LDOS) of the sample. The tunneling current has an exponential relationship to

the gap distance. For example, if the distance is decreased by 0.1 nm, the tunneling current will be increased by approximately one order of magnitude. By scanning the sample or tip in a raster pattern, an image can be generated representing the surface in real space.

Although its principle is simple and straightforward, STM is a challenging technique which requires an extremely clean and stable surface, atomically sharp tips, excellent vibration control and sophisticated electronics. A typical Omicron STM/AFM system used in this work is schematically shown in figure 2.7. The scanning of this STM is realized by the movement of sample instead of tip. An XYZ piezotube is located at the back of the sample holder in charge of precise movement. Peripheral electronics are connected to the metal tip and conductive sample to apply bias, monitor tunneling current and feedback to control the movement of the tip. The sample and tip are fixed to a stage which is isolated from external vibrations by mechanical springs. An eddy current damping system is installed at the side of stage to achieve quick stabilization. Two modes are used in STM scanning: constant current mode and constant height mode. In the constant current mode, the distance of the tip from the surface is kept constant during scanning. To achieve this, tip is moved forward and backward by feedback control to maintain the constant tip-sample separation. In the constant height mode, the tip height is fixed, while the recorded tunneling current changes exponentially with changes of sample morphology. To avoid crashing of tip, a surface with less than 1nm corrugations is required in this mode.

It should be highlighted that STM does not directly probe the real surface topography but maps the LDOS. Due to the polarity of the bias, the images could either reflect the LDOS in filled state or in empty state. If the LDOS equals to zero at certain energies, the STM could fail to probe the topmost atoms on the surface if bias is set into such energy gaps. Thus, STM measurements need to be performed at suitable biases to avoid undesired images. Sometimes, when surfaces are composed by several atomic layers with different energy gaps, the proper selection of bias in measurement could give topographic images of underlying layers. For example, epitaxial graphene on SiC(0001) exhibits such a property. At high bias (typically sample bias at -2V), the epitaxial graphene layer is transparent, and images of the underlying interfacial layer are obtained. The topography of graphene networks becomes visible at low bias (typically less than 0.5V).[101]

The sample temperature in STM acquisition is an important factor. Elevated sample temperatures are used if kinetics of surface structures is the interests of study.[102] Lowering the sample temperature is often needed to minimize thermal vibrations. Although liquid nitrogen temperature (77 K) is usually unable to freeze single atoms or molecules, this temperature is sufficient for self-assembled structures which are stabilized by intermolecular interactions and thus is widely used.[103] If the STM is cooled to liquid helium temperature (4 K), the majority of species on surface can be thermally frozen and single molecules and atoms can be easily imaged.

2.2.2 Low Energy Electron Diffraction (LEED)

From the particle-wave duality principle, the electron possesses a wave-like nature with a wavelength described by the de Broglie equation:

$$\lambda = \frac{h}{p} \tag{2.6}$$

where p is the momentum of the electron. Low energy electrons (typically 10 to 600eV) have wavelengths (0.5 to 4Å) comparable to lattice spacings of crystals. Due to the short escape depth of low energy electrons (about 0.5-1nm), LEED probes a few atomic layers of the surface. Therefore, surface diffraction patterns can be obtained by low energy electrons impinging on the surface of a crystal in UHV.

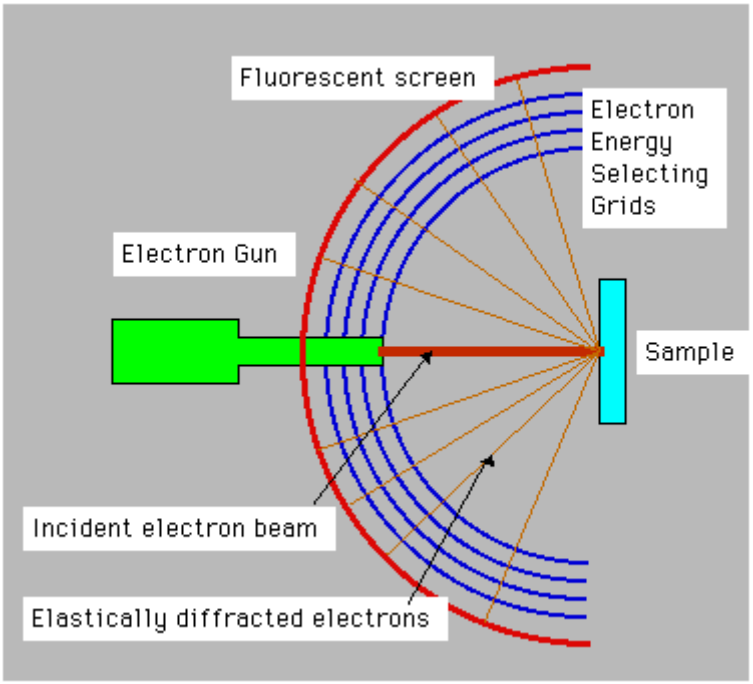

Figure 2.8. A schematic setup of a LEED system. [104]

A typical LEED system is schematically shown in figure 2.8. An electron gun is positioned at the center of the hemispherical fluorescent screen. Incident

monochromatic electron beams are perpendicularly projected onto a sample surface. Several selecting grids are positioned in front of a fluorescent screen allowing the diffracted electrons to reach the screen but blocking inelastically scattered electrons. Diffracted electrons hit the fluorescent screen and can be observed optically. By adjusting the incident electron energy, diffraction patterns can be zoomed in and out on the screen. The LEED system operates in UHV condition, both to minimize scattering of electrons by residual gases and to maintain a clean crystal surface.

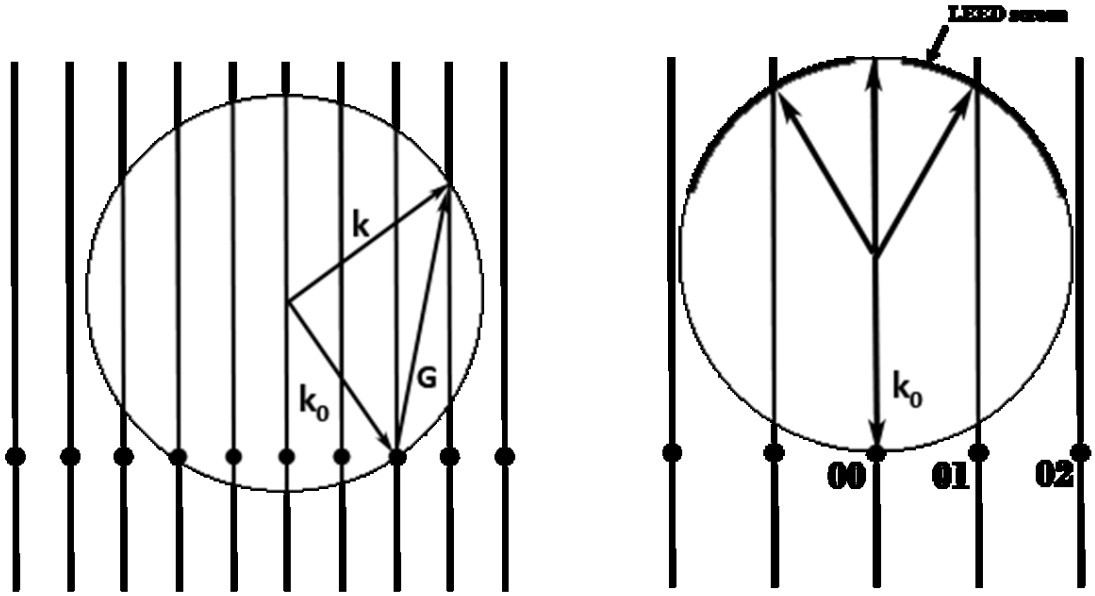

Figure 2.9. Ewald sphere construction in electron diffraction. Left panel, incident electron momentum vector **k** and reflected vector $\mathbf{k_0}$ is enclosed by a vector **G** to fulfill momentum conservation. Right panel, the case of normal incident electrons in LEED.[105]

Similar to the Bragg law in X-ray diffraction, electron diffraction can be described by the Ewald sphere construction in which momentum conservation of electron is considered (figure 2.9 left panel).[106] The size of the Ewald sphere is determined by the momentum of electrons. In this sphere, the incident and reflected electron momentum vectors (**k** and $\mathbf{k_0}$) are vectorially related to the third vector **G**, in

reciprocal space. For instance, the normal incident electrons in LEED show diffraction spots at the intersections of the Ewald sphere and reciprocal lattice rods as illustrated in the right panel of figure 2.9. Thus, LEED patterns directly reflect the reciprocal lattice of a surface structure. The reciprocal lattice vectors $\mathbf{a}^*$ and $\mathbf{b}^*$ are related to the real space surface lattice vectors $\mathbf{a}$ and $\mathbf{b}$ in the following way:

$$\mathbf{a}^* = \frac{2\pi \mathbf{b} \times \hat{\mathbf{n}}}{|\mathbf{a} \times \mathbf{b}|} \tag{2.7}$$

$$\mathbf{b}^* = \frac{2\pi \hat{\mathbf{n}} \times \mathbf{a}}{|\mathbf{a} \times \mathbf{b}|} \tag{2.8}$$

As a result, the real space lattice can be calculated from LEED patterns by equations (2.7) and (2.8). The example in figure 2.10 shows the real space lattice and the corresponding LEED pattern of a $\sqrt{3} \times \sqrt{3}R30°$ superstructure superimposed on the

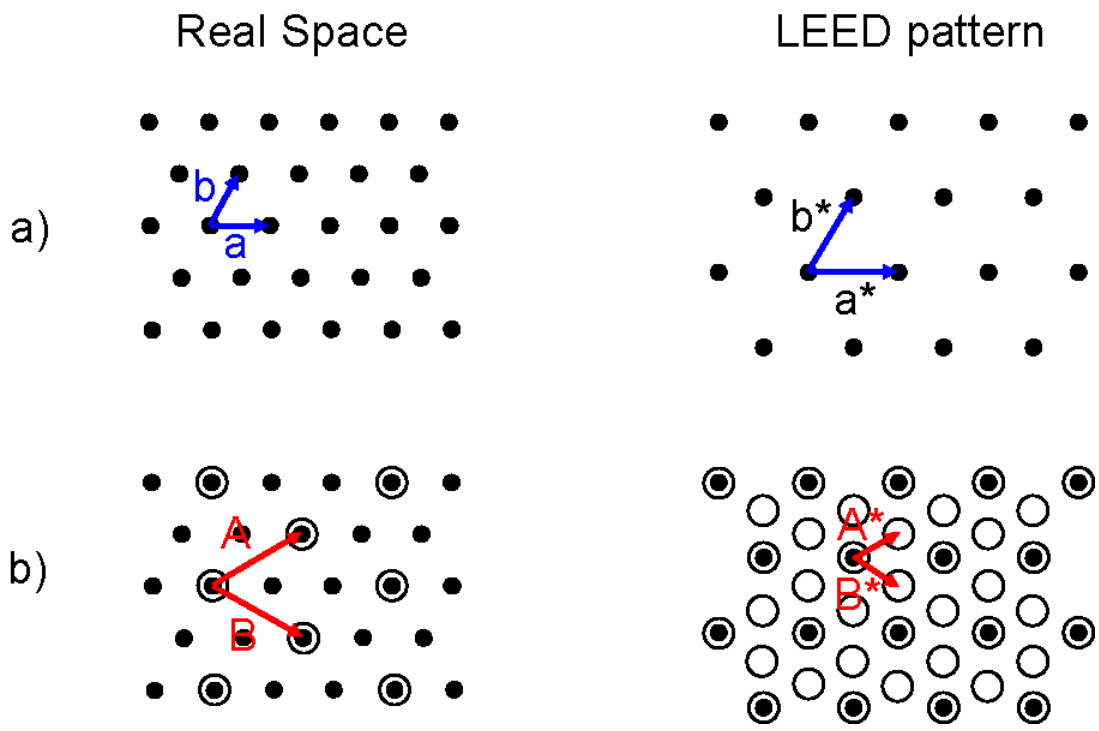

Figure 2.10. Real space lattice and corresponding LEED pattern. a) (0001) surface of a hexagonal lattice; b) a $\sqrt{3} \times \sqrt{3}R30°$ superstructure is superimposed on the lattice in a).

(0001) face of a hexagonal lattice, *e.g.* SiC(0001). This √3 superstructure shows a $\frac{\sqrt{3}}{3}$ lattice constant in LEED according to equations (2.7) and (2.8). From the LEED patterns, qualitative information on the relative size, symmetry and rotational alignment of the surface superstructures with respect to the substrate unit cell can be obtained. Moreover, the diffraction spot intensities versus incident electron beam energies or *I-V* profiles can give quantitative structural information via theoretical multiple scattering calculations. As a result, surface atom positions, interlayer spacings and other important structural information can be quantitatively evaluated.[107]

2.3 Experimental systems

In this thesis, several UHV systems including endstations attached to synchrotron facilities and dedicated STM chamber are used. These systems are described in detail in this section.

2.3.1 SINS Beamline and Multichamber Endstation

The Singapore Synchrotron Light Source (SSLS) is a second generation compact synchrotron facility located at the National University of Singapore (NUS). This facility was previously designed for mass X-ray lithography manufacturing and thus provides a user-friendly working environment (no evacuation required during beam

injection and quench) and long life-time (> 10 hours). The storage ring has a racetrack shape working at 700MeV with two superconducting 4.5T bending magnets. The critical parameters of this facility are listed in Table 2.1.

Table 2.1. Key parameters of Helios 2.[108]

Electron Energy	700MeV	Characteristic photon energy	1.47keV
Magnetic Field	4.5T	Current (typical)	300mA
Circumference	10.8m	Source diameter horizontal	1.45-0.58mm
Emittance	1.37μmrad	Source diameter vertical	0.33-0.38mm
Lifetime	>10h	Horizontal angular aperture of port	60mrad

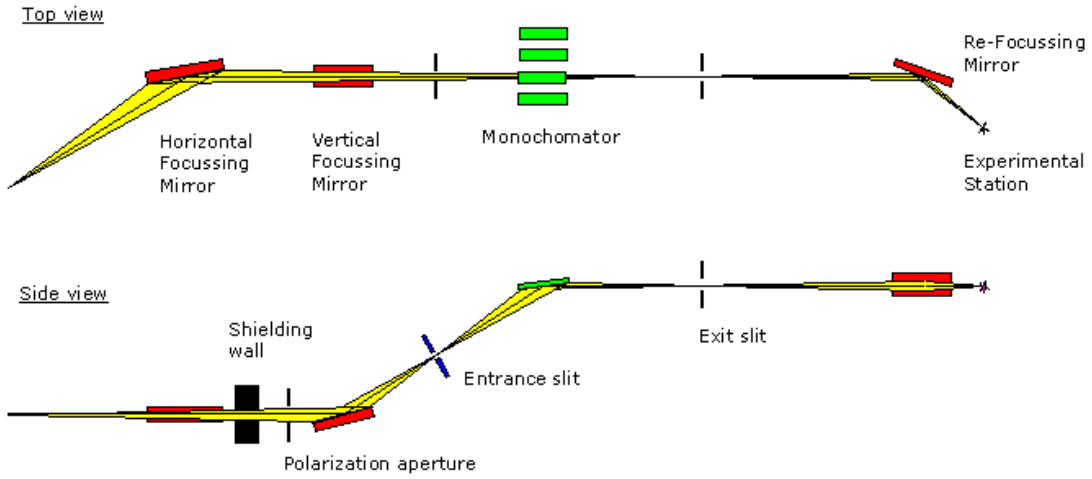

Figure 2.11. Schematic layout of the SINS beamline. [109]

The Surface, Interface and Nanostructure (SINS) beamline works at the soft X-ray region covering photon energies from 50eV to 1200eV via four interchangeable spherical gratings.[110] The layout of this beamline is schematically shown in figure 2.11 from the top and side. The beamline has three focusing mirrors; two mirrors are located before the monochromator chamber for vertical and horizontal focusing, and

one refocusing mirror (RFM) at the end of beamline to focus the monochromatic light to the sample position in the endstation. The incident photon intensity is monitored by the photocurrent on the gold-coated RFM using a Keithley electrometer. The beamline has an energy resolving power better than 2000 at a photon flux of about 10^{10} photons/s at 100 mA storage current. The spot size at sample position is about 1.5×0.2 mm^2 (FWHM).

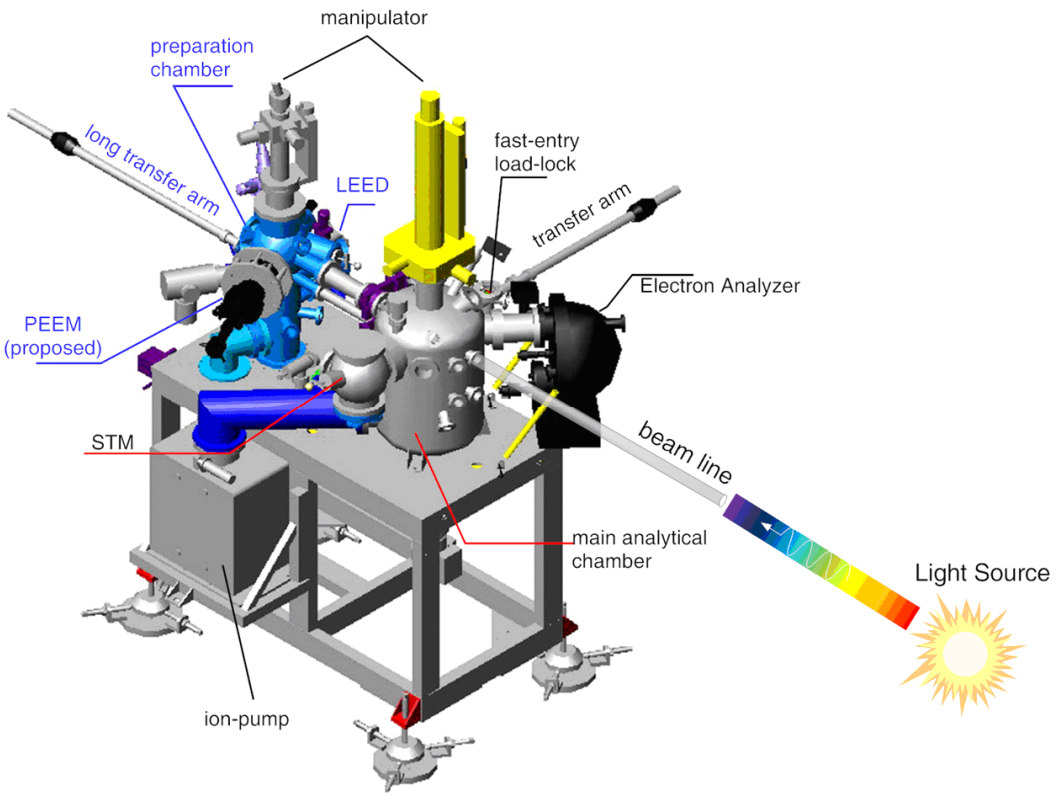

Figure 2.12. Schematic layout of the SINS beamline endstation at SSLS. [111]

The SINS endstation is schematically shown in figure 2.12. The endstation consists of two chambers interconnected by a gate valve. The main analytical chamber is equipped with a hemisphere electron analyzer (*Omicron, EA-125*) which has 7 channeltron electron multipliers with total energy resolution power ($E/\Delta E$)

larger than 1000 at 10^{10} photon flux. A sputter-cleaned gold foil is fixed at the bottom of the manipulator electrically contacted with the sample. The BE of all PES spectra are thus referenced to the Fermi level of the gold foil. *In-situ* molecular beam epitaxy (MBE) growth can be performed in the main chamber by two e-beam evaporators for metal deposition (Co, Ni, Fe and etc.) and one Knudsen cell (*MBE Komponenten*) for the deposition of organic molecules. A sputter gun and a backup twin anode (Al, Mg) X-ray gun are also installed in the main chamber for sample cleaning and checking. A room temperature STM is installed in the main chamber allowing *in-situ* imaging of the surface and adsorbates. A loadlock system is connected to the main chamber allowing fast sample loading/unloading. In addition, a silicon source via direct current heating is installed in this chamber for SiC sample preparation. The sample can be transferred *in-situ* from the main chamber to the preparation chamber using the long transfer arm for further sample preparation. The preparation chamber is equipped with a LEED system, two leak valves for gaseous molecule deposition and one e-beam evaporator for metal deposition. The sample can be either resistively heated or directly heated on both manipulators. Both chambers are equipped with ion pumps, turbo pumps and titanium sublimation pumps to maintain a base pressure better than 1×10^{-10} torr.

2.3.2 Multichamber LT-STM system

Consisting of one loadlock chamber, one preparation chamber and one STM chamber, this system is a dedicated UHV system for low temperature scanning

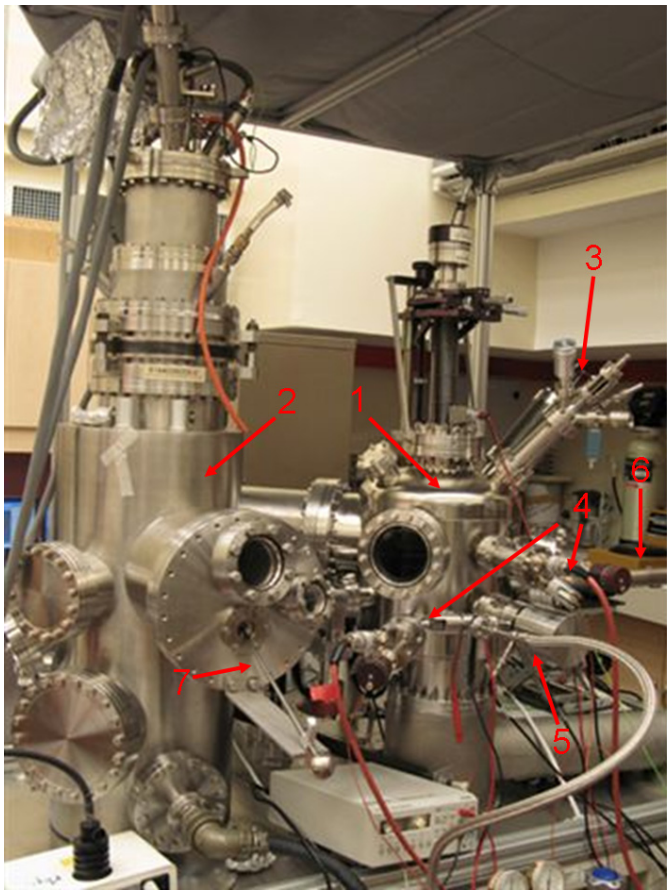

Figure 2.13. The photograph of multichamber LT-STM system located at surface science lab, NUS. [112]

tunneling microscopy studies.[103, 113] A photograph of this system is shown in figure 2.13. The preparation chamber is equipped with two Knudsen cells, one sputter gun and one leak valve for sample cleaning and MBE growth. The growth rate is calibrated either by a quartz microbalance (QCM) or by STM. An Omicron low temperature STM interfaced to a Nanonis controller is installed in the STM chamber. The STM can be cooled to liquid nitrogen temperature (77K) or liquid helium temperature (4K) for scanning. The base pressure for STM chamber is better than 6 ×

10^{-11} torr. The sample holder used in this system is compatible with the SINS beamline allowing *ex-situ* transfer and study of the same sample in both systems.

2.3.3 Surface XAFS beamline (BL3), HSRC

Hiroshima Synchrotron Orbital Radiation (HiSOR) is a second generation synchrotron facility located at the Hiroshima Synchrotron Radiation Center (HSRC), Japan. The storage ring is of a racetrack type with 2.7T conventional dipole magnets. This ring is designed to generate synchrotron light from the VUV to X-ray region. The critical parameters of this facility are listed in table 2.2.

Table 2.2. Key parameters of HiSOR[114].

Electron Energy	700MeV
Circumference	21.95m
Magnetic Field	2.7T
Characteristic photon energy	0.87keV
Current (typical)	300mA
Emittance	0.4π mm mrad
Lifetime	>8h

The Surface XAFS beamline (BL3) is situated at the bending magnet port of HiSOR. This beamline has a double InSb(111) crystal monochromator (DCM), designed to work from 800eV to 4000eV with energy resolution power ($E/\Delta E$) larger than 2000.[115] The endstation houses an x-ray photoelectron spectroscopy (XPS) analyzer, low energy electron diffraction (LEED) optics, ion gun, fluorescence

detector, liquid He cooled manipulator and etc. (figure 2.14) The XAS signal can be measured in AEY (from electron analyzer), TEY (from photocurrent) and FY modes (from fluorescence detector) simultaneously. Samples are measured at normal and grazing angles for AEY mode to enhance surface sensitivity of XAS signals.

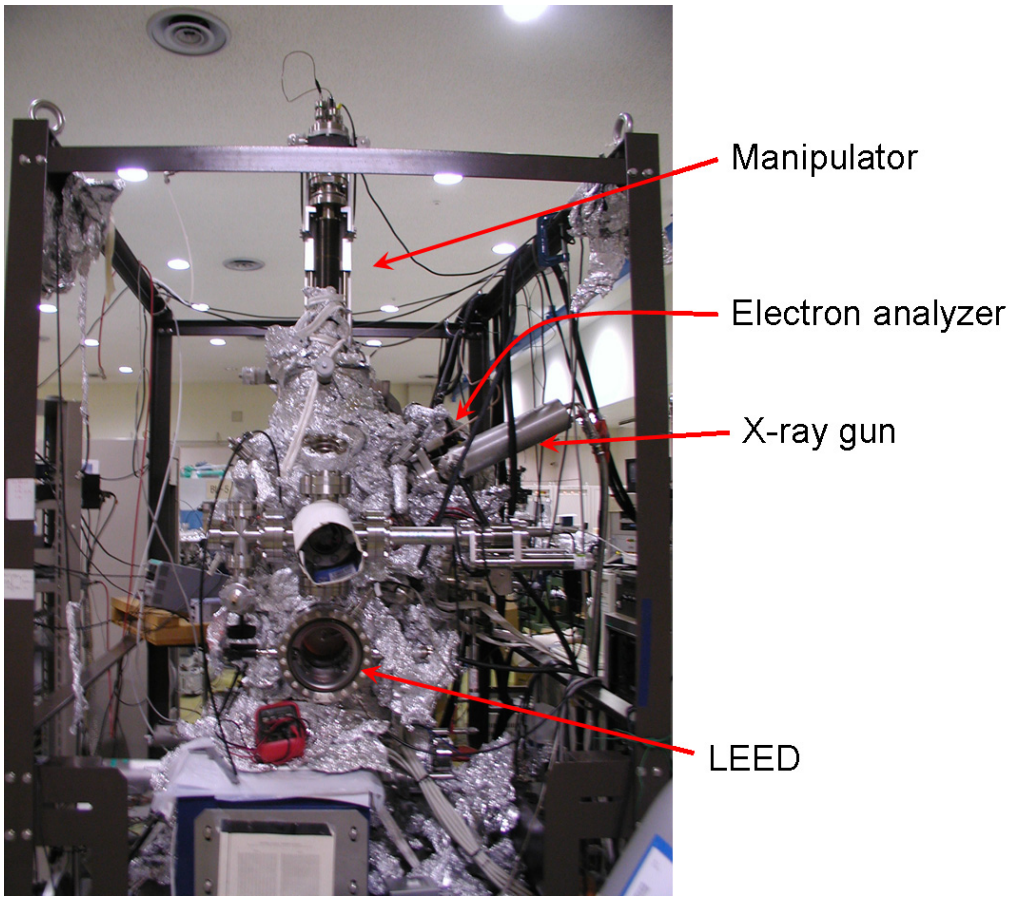

Figure 2.14. The photograph of the endstation of Surface XAFS beamline at HSRC.

2.4 Sample preparation

2.4.1 Annealing of 6*H*-SiC(0001)

The silicon-face 6*H*-SiC(0001) wafer is purchased from CREE Research. The wafer is *n*-type (nitrogen doped) with dopant concentration at 10^{18}cm^{-3}. This wafer is then cut into 1.6mm × 10mm sizes, compatible with the direct heating sample holder.

The sample thickness is 0.25mm. To ensure the uniformity of sample heating, the SiC sample is stacked on a silicon sample of the same size. The samples are carefully placed to avoid misalignment of the silicon sample. After loading into the UHV chamber, the sample is degassed at 600°C overnight and then heated to 850°C in the presence of a silicon flux for about 2 minutes. The silicon flux is generated from a silicon source heated to 1200°C with a sample-source distance of about 1cm. The silicon flux to SiC sample during annealing helps to remove native oxides and generates a silicon-rich 3 × 3 surface reconstruction.[20] The sample is subsequently annealed to 1050°C, 1150°C and 1250°C, revealing √3 × √3R30°, 6√3 × 6√3R30° (SiC nanomesh) and 1 × 1 graphene LEED patterns, respectively (figure 2.15). The sample

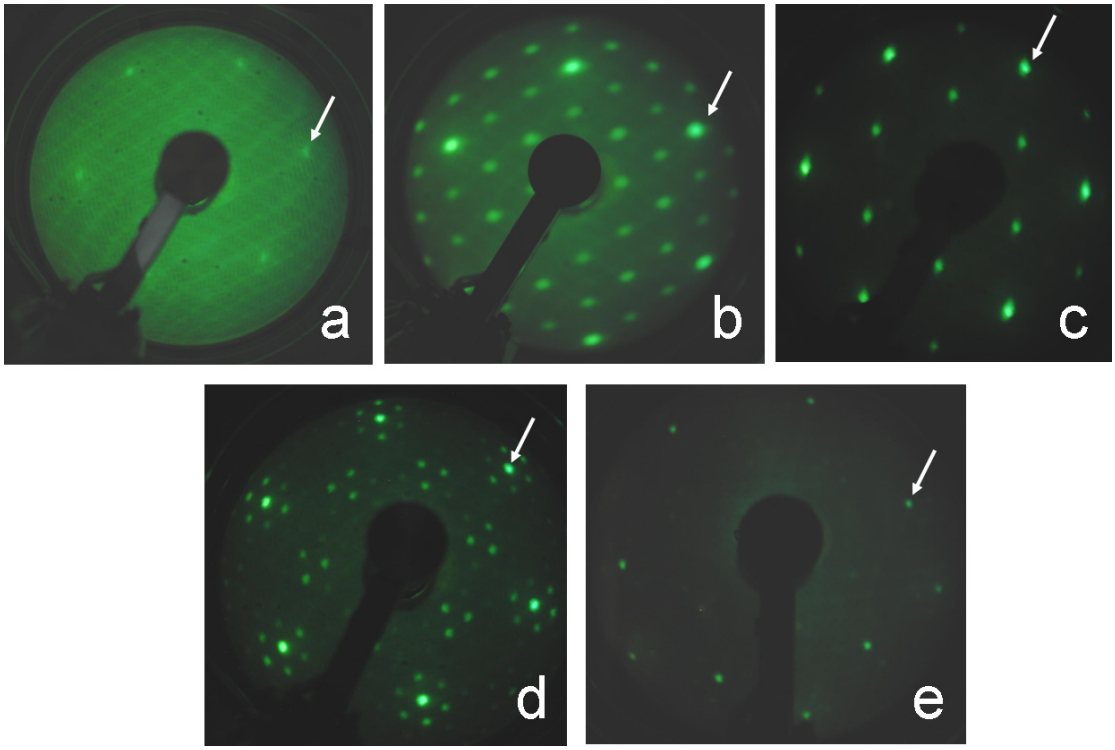

Figure 2.15. The LEED patterns of SiC with different reconstructions. a) 1 × 1, b)3 × 3, c)√3 × √3R30°, d) 6√3 × 6√3R30°, e) 1 × 1 graphene lattice. White arrows in figures indicate the 1 × 1 SiC lattice.

temperature is monitored by a pyrometer. Among these surface reconstructions, the SiC nanomesh and 1 × 1 graphene are stable enough to undergo *ex-situ* transfer. After proper annealing in UHV, clean surfaces of the two reconstructions can be re-obtained as determined by STM.

2.4.2 Deposition of organic molecules

Three organic molecules, fullerene (C_{60}), pentacene and copper phthalocyanine (CuPc) are studied in this work. All molecules are purchased from *Sigma Aldrich* at sublimation grade (>99.9%). The molecules are put into pre-degassed PBN or quartz crucibles of Knudsen cells. Before deposition, the molecular sources are thoroughly degassed at their evaporation temperatures for several hours. During growth, the pressure is always kept better than 2×10^{-9}torr. The evaporation temperatures for the three molecules are listed in table 2.3. During deposition, the sample is kept at room temperature.

Table 2.3. The sublimation temperatures for organic molecule sources.

Molecules	CuPc	C_{60}	pentacene
Temperature	350°C	250°C	190°C

The nominal thicknesses of deposited organic films on SiC nanomesh are estimated from the attenuation of the XPS intensity of SiC Si *2p* substrate peak assuming a near layer-by-layer (Frank-van der Merwe) growth mode for organic layers by the following formula:

$$I(d) = I_0 \exp(-\frac{d}{\lambda \cos\theta}) \tag{2.9}$$

where I_0 is the initial Si 2*p* intensity of pristine SiC nanomesh, *I(d)* is the intensity after deposition, *d* is the nominal thickness of organic films, and θ is the angle between analyzer detecting direction and sample surface normal direction. In most cases, θ is kept zero for simplicity. λ (in nanometers) is the IMFP of photoelectrons in organic films which depends on the KE of photoelectrons (E_{kin} in eV) and the density of organic films (ρ in g/cm^{-3}) according to the following empirical relation[116]:

$$\lambda = (49E_{kin}^{-2} + 0.11E_{kin}^{1/2}) / \rho \tag{2.10}$$

If STM measurements are involved in the experiments, the thickness of organic molecules at submonolayer region is also calibrated by STM images as an alternative method.

CHAPTER 3 INVESTIGATION OF 6*H*-SiC (0001) NANOMESH SURFACE STRUCTURE

3.1 Introduction

Among all surface reconstructions on 6*H*-SiC(0001), the SiC nanomesh ($6\sqrt{3} \times 6\sqrt{3}R30°$ reconstruction) is the most complicated. This surface has been experimentally and theoretically studied in the past two decades.[9, 10, 12, 26, 28, 29, 49, 51, 58, 59, 117] Due to its large unit cell and surface disorder in the STM observations, the atomic structure of the SiC nanomesh still remains controversial. Nevertheless, it is widely accepted that its carbon richness is due to the desorption of silicon at elevated temperature. As the 13 graphene lattice and $6\sqrt{3}$ SiC lattice are commensurate, most researchers believe that this surface has a close relation to the graphene or graphene-like framework. Thus, many structural models are based on the graphene framework and try to explain how the graphene framework is bonded to the substrate. These models include graphene above 1×1 SiC substrate,[49] graphene above $\sqrt{3} \times \sqrt{3}R30°$ reconstruction,[118, 119] graphene islands above 1×1 SiC substrate[28] and graphene covalently bonded to 1×1 SiC substrate,[58] but none of them can fully explain the topography of this surface in STM. In all these models, the graphene network is selectively bonded to the silicon atoms at interface. Therefore, the silicon atoms play an important role in the structure of SiC nanomesh and should be thoroughly studied.

Unlike other reconstructions on 6*H*-SiC(0001), the SiC nanomesh appears much more disordered in STM images and lacks thorough explanations. These disorders have been observed by STM but a consistent explanation has yet to be proposed. One general speculation suggests that the disorders are attributed to the lattice mismatch between the SiC nanomesh and SiC 1 × 1 surface. Some researchers have used the disorder to explain the STM-LEED contradiction by assuming that the cells in STM observation have two different sizes alternatively packed on the surface.[29, 58] However, high resolution STM images reveal the surface is even more disordered than what these models suggested.

In this chapter, the disorder in the SiC nanomesh is carefully studied by XPS, STM and XAS measurements. In core level XPS measurements, both C *1s* and Si *2p* spectra show continuous changes under prolonged annealing period. This suggests that the SiC nanomesh has dynamic silicon to carbon stoichiometric ratio depending on the annealing duration. In STM measurements, the disorder in SiC nanomesh is evaluated at different scales. The surface appears less disordered at larger length scales. In NEXAFS and EXAFS measurements, the silicon atoms are investigated instead of carbon atoms. The results reveal bulk silicon vacancies and surface silicon clusters are present in the SiC nanomesh samples. These observations suggest SiC nanomesh disorder exists both at the surface and in the bulk.

3.2 Results and Discussion

3.2.1 Photoelectron study of 6*H*-SiC (0001) nanomesh surface

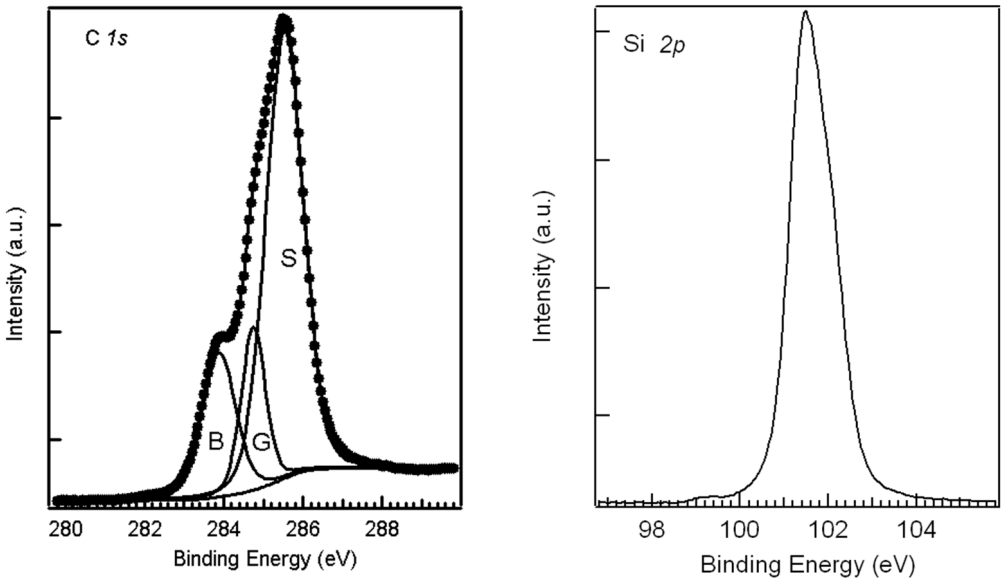

Figure 3.1. C *1s* and Si *2p* XPS spectra for SiC nanomesh sample.

As the C *1s* and Si *2p* XPS spectra have already been investigated by several groups,[9, 28, 51, 117, 120] the XPS studies shown here will focus on the changes observed during annealing. The C *1s* and Si *2p* XPS spectra of the SiC nanomesh are shown in figure 3.1 for reference. The C *1s* spectrum is fitted by three components at 283.8 ± 0.1eV, 284.8 ± 0.1eV and 285.5 ± 0.1eV corresponding to bulk SiC carbon (B peak), graphene-like carbon (G peak) and SiC nanomesh carbon (S peak), respectively. This fitting is consistent with previous studies.[9, 51] In Si *2p* spectrum, one major peak is observed, located at 101.5 ± 0.1eV. This peak is attributed to bulk silicon atoms in SiC. A very weak shoulder at about 99.2eV is observed, possibly related to surface silicon atoms in silicon-silicon bonding configurations. The

existence of silicon-silicon bonding is also supported by the NEXAFS study in section 3.2.3.

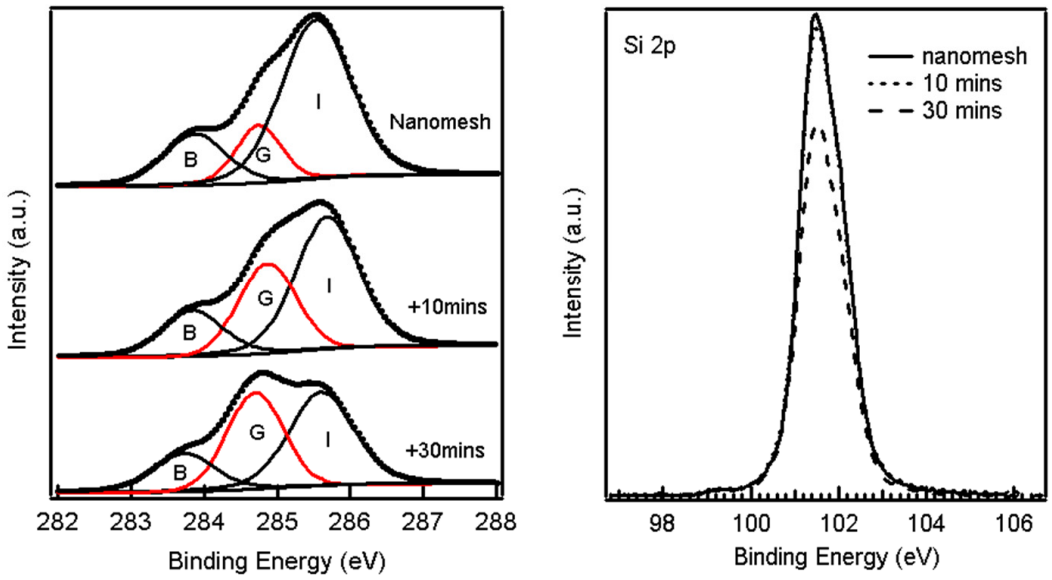

Figure 3.2. C *1s* and Si *2p* XPS spectra after prolonged annealing at 1100°C.

Prominent changes in the spectra are observed after annealing at 1100°C for 10 and 30mins (figure 3.2). In C *1s*, the G peak gradually increases accompanied by a decrease in the S peak. The increase of G peak indicates the graphitization of surface carbon atoms which is a characteristic of the nanomesh-graphene transition. In Si *2p*, the intensity of the main peak exhibits a consistent attenuation, probably due to the increasing coverage of graphene overlayer. Thus, instead of the expected nanomesh-graphene transition at 1200°C or higher, the SiC nanomesh could also undergo this transition at temperatures as low as 1100°C by prolonged annealing. These results suggest that there is no distinct transition temperature for the nanomesh-graphene transition.

3.2.2 STM study of the 6*H*-SiC (0001) nanomesh surface

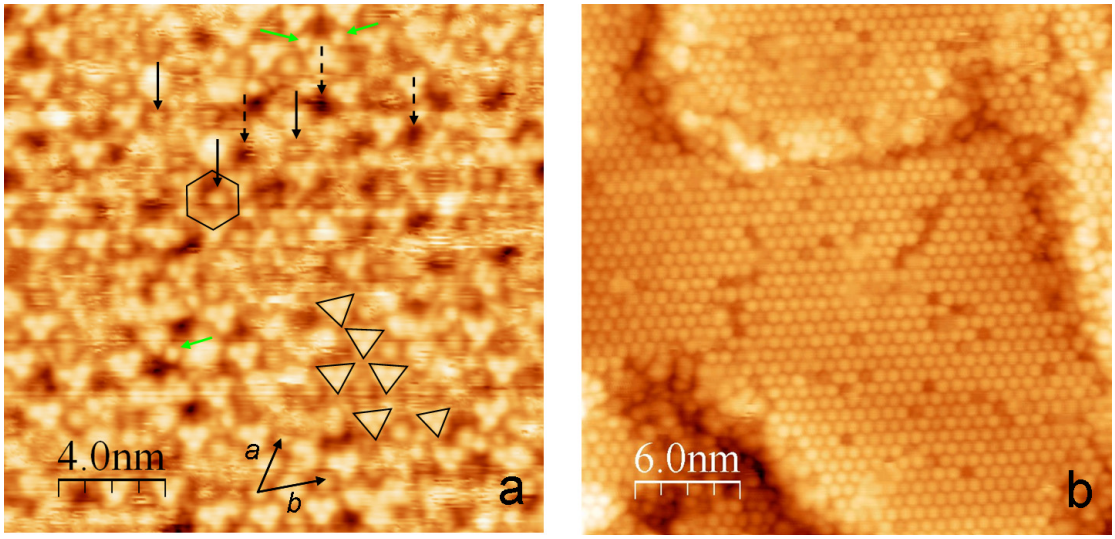

Figure 3.3. The STM images of two reconstructions on 6*H*-SiC(0001) surface. a. nanomesh surface, (V_T= 2.1 V, I_T= 70 pA, 20 × 20nm^2); b. 3 × 3 reconstruction, V_T= 2.5 V, I_T= 0.5 nA, 30 × 30nm^2) .

STM has been proven to be an important technique to probe the local structures of a surface. The images obtained helps to reveal the atomic structure of the probed surface. As shown in figure 3.3a, the SiC nanomesh surface is imaged by STM at a scan size of 20 × 20nm^2. The surface shows a honeycomb-like structure with unit cell size ranging from 1.8 to 2.0nm, close to 6 times the SiC lattice constant. To highlight the honeycomb-like structure, a hexagon is placed on one cell in figure 3.3a. At this length scale, trimeric protrusions at the corners of honeycomb cells (triangles), round protrusions at the center of cells (solid arrows) and the rims of cells (green arrows) can be distinguished. In contrast to the 3 × 3 reconstruction on SiC (figure 3.3b), which appears as highly ordered round protrusions hexagonally packed together, the SiC nanomesh surface has an much more disordered appearance. In some cells, small protrusions can be found at the center, while the center of other cells appears as dark

pits (dashed arrows). Furthermore, the distribution of cells with or without protrusions is random. As highlighted by triangles, the trimeric protrusions have variable orientations. The distance between protrusions is also not constant due to the varying size of cells surrounded by these protrusions. The variations of trimeric protrusions appear as one major source of surface disorders. Other minor features such as protrusions at the rim of the cells (green arrows) also appear randomly and disappear on the surface. Thus, the SiC nanomesh should be regarded as a pseudo periodic structure instead of an ordered reconstruction from the image at 20nm length scale.

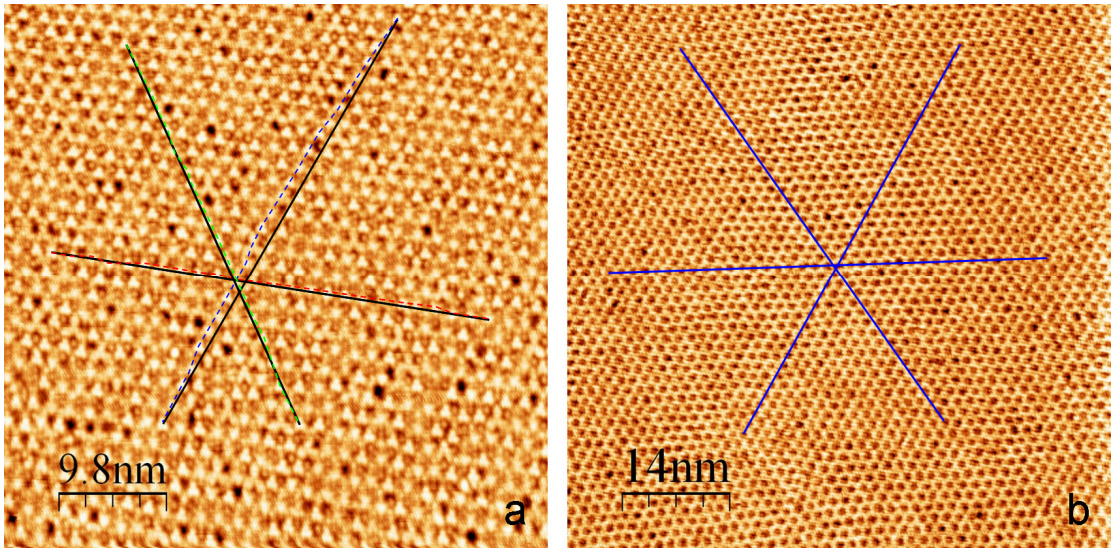

Figure 3.4. Honeycomb cells deviating from translation axes in SiC nanomesh at intermediate length scales. a) (V_T= 2.1 V, I_T= 0.2nA, 49 × 49 nm^2); b) (V_T= 2.1 V, I_T= 0.2nA, 70 × 70 nm^2). Bold black and blue lines indicate the translation axes and the dashed lines indicate the actual honeycomb cell positions.

Although the SiC nanomesh appears nearly amorphous in the short length scale, it displays periodicity when the scale increases. In figure 3.4, STM images of the nanomesh surface at 49 × 49 nm^2 and 70 × 70 nm^2 scan sizes are shown. At such intermediate scales, the disorders appeared in short scale in figure 3.3 become too

small to distinguish, but the disorders originating from the positional deviation of the honeycomb cells from its translation axes remains apparent. In figure 3.4a, the translation axes of surface are highlighted by solid black lines along the triangular clusters. The actual positions of triangular clusters along the translational axes are shown by the dashed lines. The deviation between them indicates the surface translation disorder which could be as large as the scale of cells (about 2nm). This translational disorder reduces when the length scale increases. In figure 3.4b with a size at 70 × 70 nm^2, the deviation from translational axes is less apparent and the transitional order is slightly improved. When the scale further enlarges, this translational disorder also becomes less apparent. In conclusion, the SiC nanomesh surface which is highly defective at the short range can form a highly periodic structure at long range.

The term *self-assembly* has been widely used in many disciplines, but each of them has a different flavor and emphasis. To avoid misunderstanding of this term, a clear definition should be given. Herein, the definition suggested by Whitesides and Grzybowski is used through the thesis, who defined self-assembling systems at global or local equilibrium as static self-assembly.[121] Thus, surface reconstructions, which are a consequence of the transition from non-equilibrium to equilibrium by rearrangement and relaxation, are typical static self-assemblies. The examples include the 3 × 3 and √3 × √3*R*30° reconstructions on 6*H*-SiC(0001), which show highly periodic atomic structures at their global equilibrium states. However, the SiC nanomesh does not behave as a typical static self-assembly. All observations of this

surface include plenty of surface disorders, variable surface structure and variable surface composition suggesting it exists in a non-equilibrium state. Thus, by definition, the SiC nanomesh should not be regarded as a static self-assembly. Instead, we describe the SiC nanomesh as self-organization because the formation of this surface is driven by continuous silicon desorption.

3.2.3 XAS study of the SiC nanomesh surface

As mentioned in chapter 1, most of the studies investigating this surface focus on carbon, mainly due to its richness. However, in their models, carbon atoms only form a graphene network, while the silicon atoms determine how this graphene networks are bonded to the substrate. Thus the silicon atoms are as important as the carbon atoms in the structure of SiC nanomesh. Few studies have paid attention to the silicon atom because surface silicon atoms are few and have similar chemical state to that of bulk atoms, making them difficult to distinguish by XPS.

To study silicon atoms in the SiC nanomesh, special techniques which are able to identify silicon atoms both in bulk and at surface should be chosen. Hence, the XAS techniques with AEY and FY modes are used to study the silicon atoms at the Si *K*-edge of SiC nanomesh sample. Other surface reconstructions including 3×3, $\sqrt{3} \times \sqrt{3}R30°$, and 1×1 EG are also investigated for comparison. Unlike the XPS technique, XAS is sensitive to local structures of the selected element, *i.e.* silicon in SiC nanomesh. The evolution of SiC surface reconstruction studied by XAS at the element absorption edge can be divided into near edge x-ray-absorption fine structure

(NEXAFS) and extended x-ray absorption fine structure (EXAFS) at the Surface XAFS beamline (BL3) at HiSOR. The former technique offers element-specific local chemical and structural information and the latter technique reveals element-specific quantitative local structural information. By combining both techniques, the chemical and structural information of Si atoms in the SiC nanomesh can be obtained. Two detection yields (FY and AEY) are employed in x-ray absorption spectra with probe depths about several micron meters and several nanometers, respectively. In this

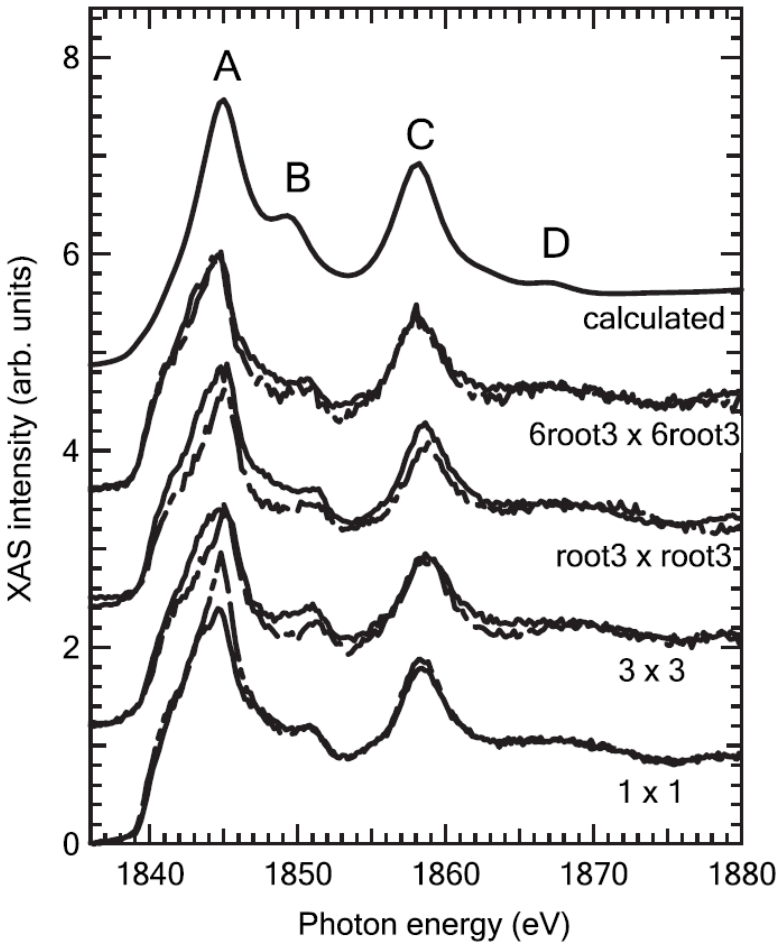

Figure 3.5. Si *K*-edge NEXAFS spectra for different SiC surfaces measured using Si *KVV* Auger-electron yield at normal emission (solid lines) and a grazing angle of 70° (dashed lines). For comparison, the theoretical calculated Si *K*-edge spectrum of 6*H*-SiC is also presented.

experiment, both yields at normal emission angle (0°) and grazing emission angle (70°) are measured to obtain depth-dependent information for silicon atoms.

Figure 3.5 shows the Si *K*-edge NEXAFS spectra for all the reconstructions measured using Si *KVV* Auger-electron yield at both normal emission (solid lines) and at a grazing angle of 70° (dashed lines). For comparison, the theoretical calculated spectrum using the FEFF package (version 8.20, University of Washington)[122] is also shown. In the calculated spectrum, there are four clear features notated as A, B, C, and D as indicated in figure 3.5. All the measured spectra are similar to the calculated one with all the features present, and this is consistent with previous spectra reported for SiC in literature.[123-125]

Unlike the Auger yield, the fluorescence yield spectra in figure 3.6 report clear differences for different surface reconstructions, even though all the features observed in figure 3.5 can be identified in all the spectra in figure 3.6. For the 1 × 1 surface, it is clear that the peaks with high intensity (peaks A and C) in figure 3.5 are broader in figure 3.6, especially peak A, and the weaker features (B and D) in figure 3.5 are stronger in figure 3.6. These phenomena are attributed to saturation effects in x-ray absorption measurements since the escape depth λ_s of fluorescence yield is comparable to the x-ray penetration depth λ_x, *e.g.* in the scale of micronmeters.[126] These effects are not seen in figure 3.5 due to the much short Auger electrons' mean-free path (about 3.7 nm at a kinetic energy of 1850 eV) (Ref. [127]) in comparison with λ_x of over 2 μm.[128] The XAS signal intensity is proportional to the sum of the x-ray intensity multiplied by the x-ray absorption cross section μ(E) over the whole

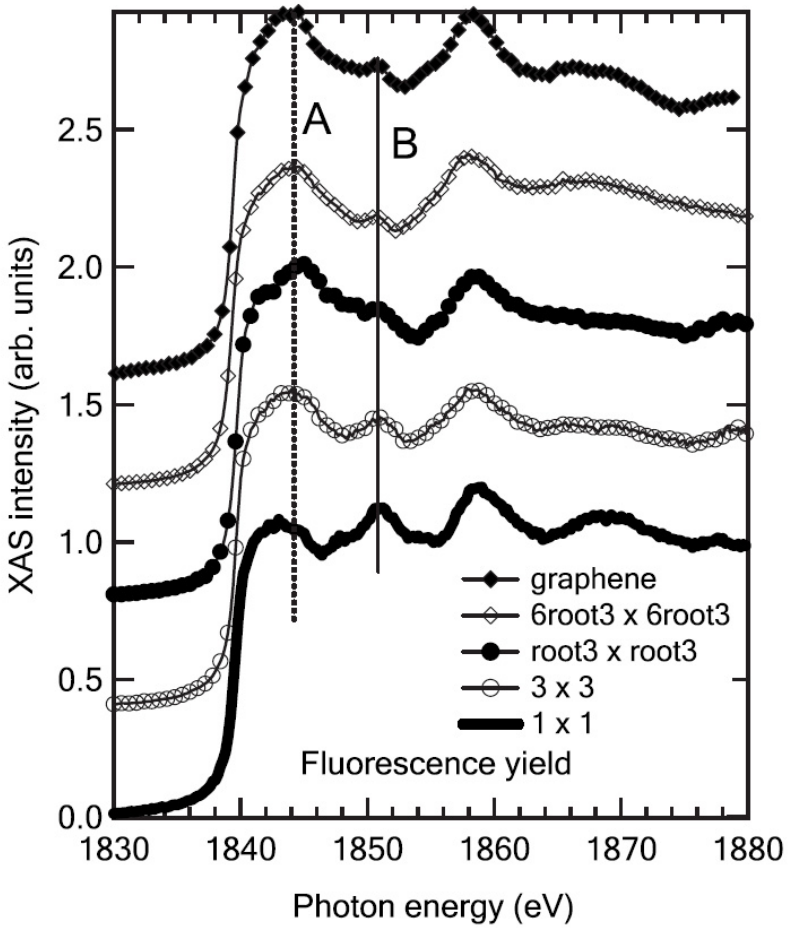

Figure 3.6. Si *K*-edge NEXAFS spectra for different SiC surface structures measured using fluorescence yield. The solid lines, open circles, filled circles, and open diamonds represent the measurements for 1 × 1, 3 × 3, √3 × √3*R*30° and 6√3 × 6√3*R*30°, respectively.

probing depth.[126] To measure the spectrum correctly, λ_s should be much shorter than λ_x [the inverse of μ(E)]: only under this condition is the attenuation of x-ray within λ_s negligible and the signal intensity change directly reflects the change in the x-ray absorption section. When this condition is not satisfied with λ_s comparable to or even longer than λ_x, the attenuation of the x-ray within λ_s is no longer negligible, hence reducing the detected XAS signal with a so-called saturation effect. The high x-ray absorption μ(E) peak will become smaller due to the higher x-ray attenuation

within λ_s, whereas smaller μ(E) features will become relatively larger due to less x-ray attenuation within λ_s.[126] In other words, the small absorption features are amplified due to the saturation effects.

Quantitatively, the XAS signal is given by $C1\times\left\{1/\left[1+C2\times\lambda_s\times\mu(E)\right]\right\}\mu(E)$, with $C1$ and $C2$ being two constants, which is simply proportional to μ(E) only for very small μ(E).[126] Comparing all the spectra in figure 3.6, it is noticeable that the peak at 1851 eV (feature B in figure 3.5) shows substantial variation for different surface reconstructions. With increasing annealing temperature, this peak becomes smaller. This systematic but small change is not seen in the Auger yield because it could be hidden by the experimental uncertainty in AEY measurements. This change is distinguishable only in the fluorescence yield mode with much longer probe depth which enhances this feature due to saturation effects. The intensity change of feature B must therefore be related to the local structural change of Si atoms within the probing depth of fluorescence yield and needs to be addressed.

To understand what causes the intensity drop of peak B, a series of calculated NEXAFS spectra is shown in figure 3.7 (left panel) for SiC clusters of several different sizes. The SiC clusters were extracted from the structure of bulk 6*H*-SiC by taking Si as adsorber and increasing the cluster size shell by shell. The first cluster with notation "Si4C12Si" consists of 1 Si for adsorber, 4 C atoms as the nearest neighbors, and 12 Si atoms as next-nearest neighbors. By adding the atoms in the outer shell to the first cluster shell by shell, the cluster size is gradually increased. Except for the first cluster, the notations in the left panel of figure 3.7 refer to the

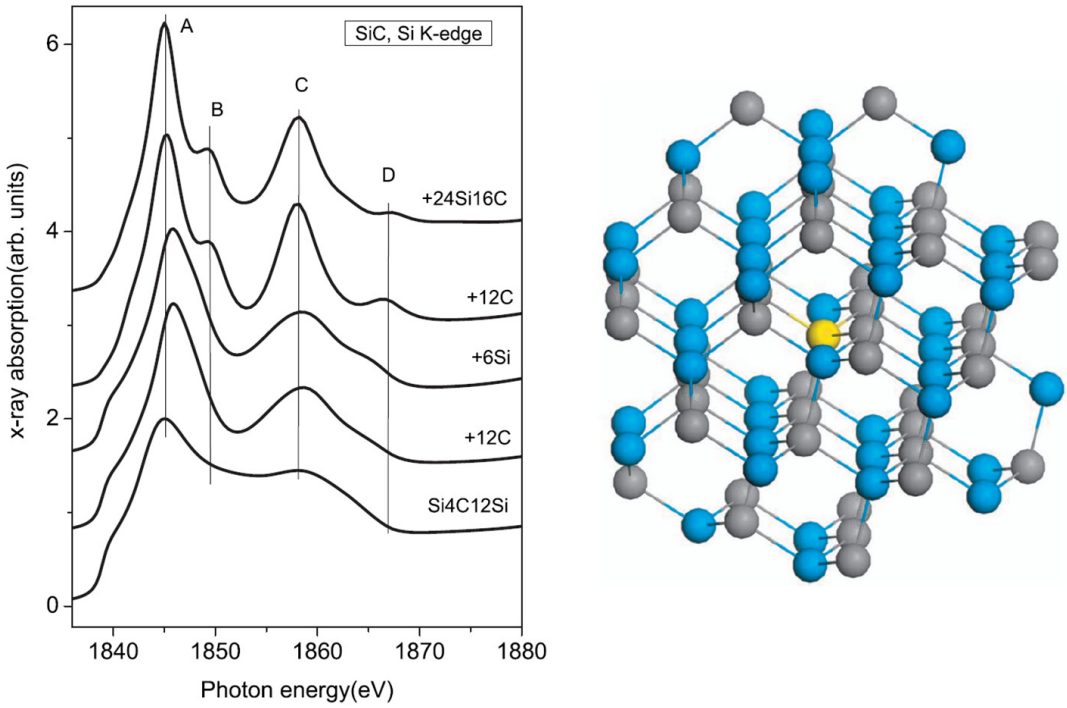

Figure 3.7. Theoretical calculated Si *K*-edge NEXAFS spectra for 6*H*-SiC clusters with different sizes. Left panel, from the bottom spectrum, the cluster size increases by adding atoms in the outer shell as described in the text. Right panel, 6*H*-SiC clusters consisting of 87 atoms, where the yellow, blue, and gray balls represent the center Si atom, other Si atoms, and C atoms, respectively.

atoms in the outer shell added to the previous cluster. Therefore, the last cluster has 1 Si, 4 C, 12 Si, 12 C, 6 Si, 12 C, 24 Si, and 16 C atoms from inner to outer shells (see figure 3.7 right panel). The left panel of figure 3.7 clearly shows that the intensity of peak B increases with the size of the SiC cluster. In other words, the peak B intensity is strongly related to the long-range order of the SiC crystal and decreases with increase in crystal disorder. As the probe depth of fluorescence yield is in the order of several micrometers, this disorder upon annealing at high temperatures occurs much deeper than the first few layers of the SiC sample. Hence we deduce that during annealing of the different reconstructions, surface Si atom desorption does not give

the complete picture.[60] Si atoms from deeper layers also diffuse to the surface with corresponding Si vacancies moving as deep as the fluorescence probing depth (*i.e.*, in the order of several micrometers). It is observed that height of peak D in left panel of figure 3.7 increases first then decreases with increasing cluster size. Thus, peak D has no simple dependence on the disorder. This actually reflects from the data in figure 3.6, where peak D indeed does not simply decrease with increasing temperature (disorder). Therefore, we will follow peak B more closely henceforth.

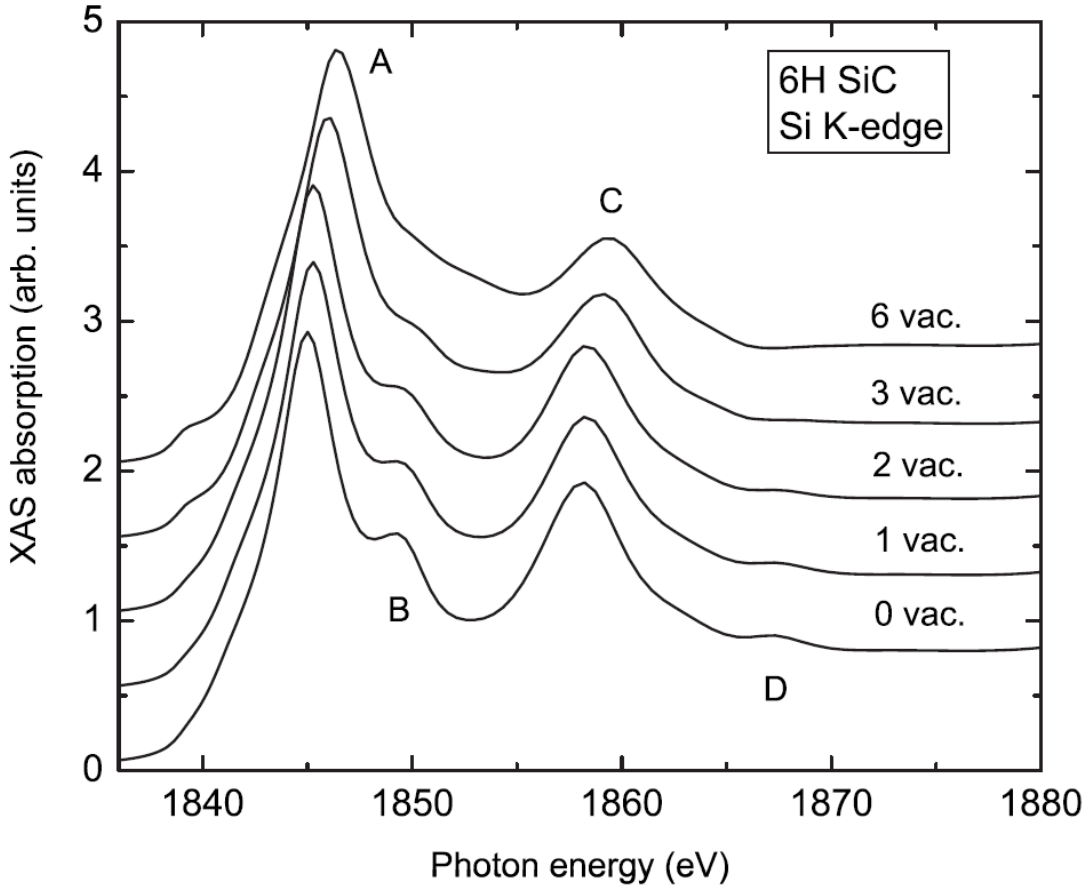

Figure 3.8. Theoretical calculated Si *K*-edge NEXAFS spectra for 6*H*-SiC clusters with 48 atoms and different numbers of vacancy at the next-nearest neighbor of the center Si atom.

To verify Si vacancies as the origin of the disorder and quantitatively estimate its concentration, a series calculated NEXAFS spectra is shown in figure 3.8 for the SiC

cluster shown in right panel of figure 3.7 with different numbers of Si vacancies at the next-nearest-neighbor site from the center Si atom. There are twelve silicon atoms at the second shell of the SiC cluster. Among them, one, two, three and six silicon atoms are selectively removed from the cluster to simulate the silicon vacancies in SiC nanomesh. The decrease in feature B is reproduced by increasing the number of Si vacancies, supporting our hypothesis that Si vacancies are responsible for the observed disorder. It is noticed that feature A shows slight shifts to higher photon energy with increasing numbers of vacancies in figure 3.8, and this is in excellent agreement with what was observed in figure 3.6, where feature A of epitaxial graphene is at higher photon energy than that of the unreconstructed SiC. All the spectra in both detection modes (figure 3.5 and 3.6) show feature B whereas feature B virtually disappears in the calculated spectrum (figure3.8) with three vacancies. Hence we deduce that the experimental spectrum for epitaxial graphene corresponds to the calculated spectrum with one or two vacancies. Thus we are able to estimate the average vacancy concentration for reconstructed SiC to be between one or two vacancies over thirteen silicon atoms (one silicon atom measured and its 12 next-nearest neighbors), *i.e.* between 8% and 15%, with the highest Si vacancy concentrations for epitaxial graphene. It is noted that figure 3.6 shows slightly smaller feature B at grazing angle for all the reconstructed surfaces. Considering that AEY at grazing angles is more surface sensitive, this indicates that the concentration of the Si vacancies decreases from the surface to the bulk, similar to the oxygen profile in diffusion limited silicon oxidation.[129, 130] To explore if high-temperature

annealing induces such a high concentration of vacancy defects to the whole SiC crystal, x-ray diffraction (XRD) measurements on the samples before and after annealing at 1300 °C found no noticeable difference. This indicates that the disorder is basically limited to a certain depth (smaller than the XRD probing depth of hundreds of micrometers) close to the surface and supports the hypothesis that disorders originate from desorption of Si atoms from the near-surface region. It is shown that the concentration of Si vacancies decreases from the surface to the bulk; however, the exact depth profile is difficult to determine using XAS, and future experiments may be needed to resolve this depth profile especially at the interface region beneath the buffer layer.

The existence of Si vacancies in bulk could explain the disorders observed on the SiC nanomesh surface. These vacancies are randomly distributed in SiC bilayers and probably affect the bonding between the top graphene-like layer and the SiC bilayers, giving rise to local disorders in the SiC nanomesh. However, the basic periodicity of SiC bilayers is not affected by the low concentration of Si vacancies. Thus, the long range order of SiC nanomesh is kept. Due to presence of Si vacancies, the crystal structure of SiC should undergo local reconstruction and relaxation. These bulk structure changes may alter the electronic structure of SiC by the introduction of defect states in the band gap. Detailed information about these changes should be investigated by future ARPES studies to provide a better understanding of the effect of Si vacancies on the electronic structure of SiC nanomesh.

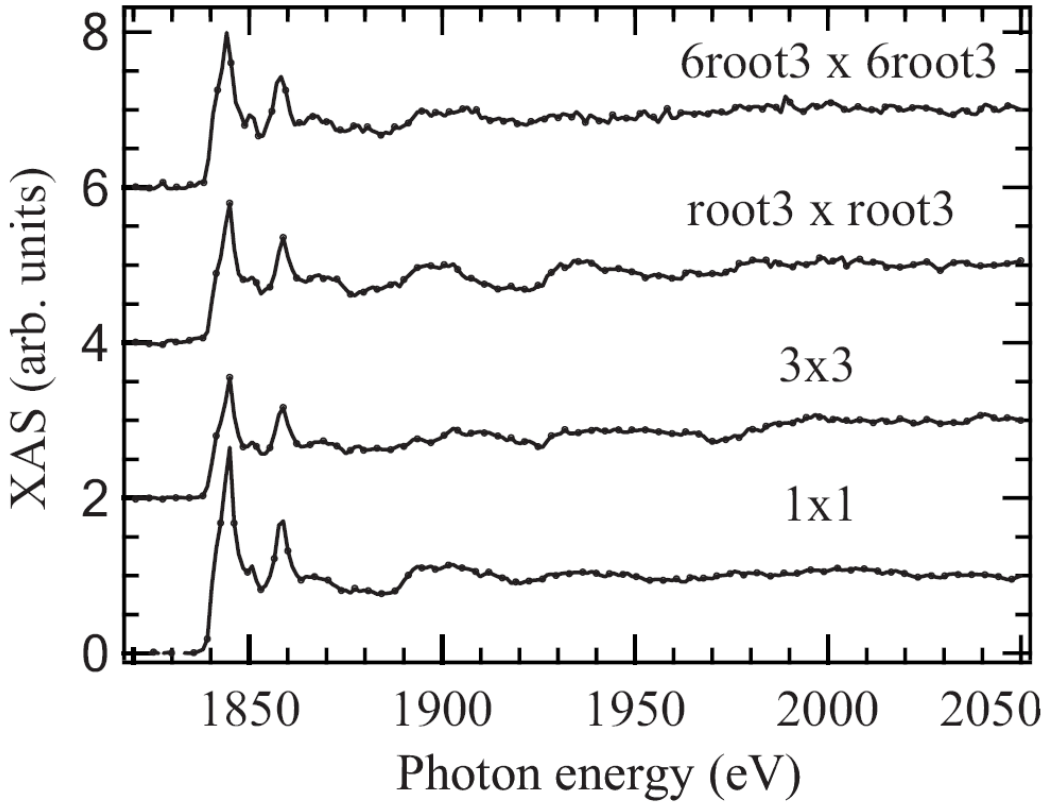

Figure 3.9. Si *K*-edge EXAFS spectra for different SiC surfaces measured using Si *KVV* Auger electron yield at a grazing angle of 70°.

As the fluorescence yield in NEXAFS measurement deviates greatly from the real absorption cross section due to strong saturation effects,[126] Auger yield is applied to measure EXAFS spectra. Figure 3.9 reports the Si *K*-edge EXAFS spectra for different SiC surface structures measured using Si *KVV* Auger electron yield at the surface sensitive grazing angle of 70°. The near edge spectra of Si *K*-edges are consistent with previous reports.[124, 125] In the extended region, distinct oscillations are observed for the different surface reconstructions.[123]

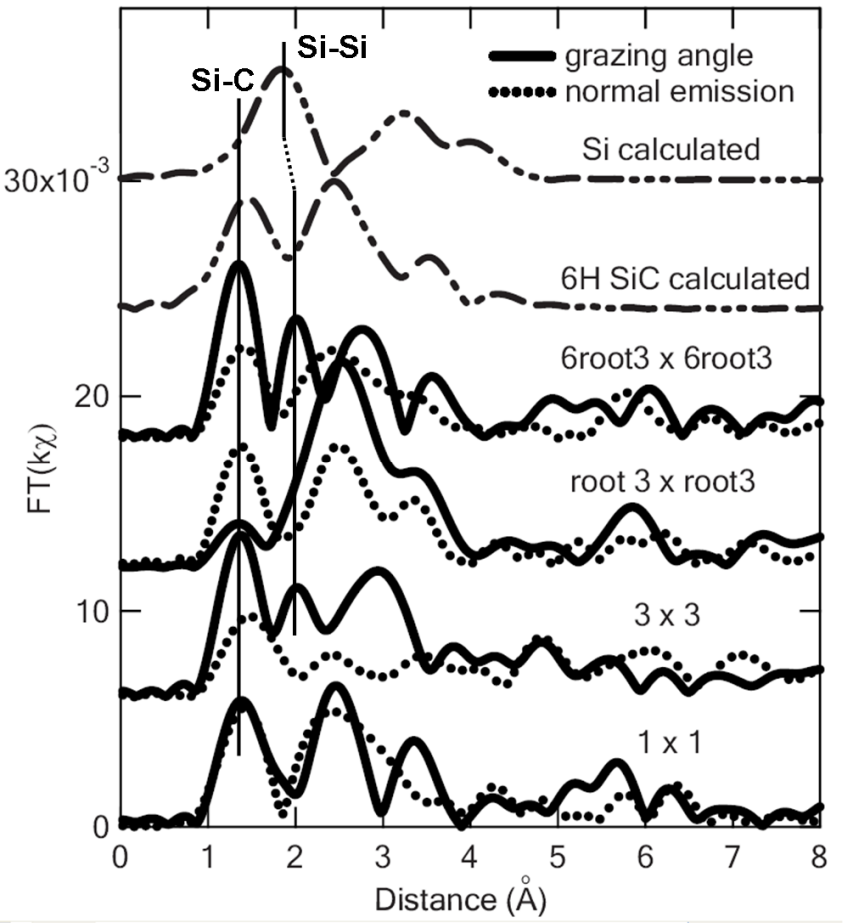

Figure 3.10. . Fourier transforms (not corrected for phase-shift) of the Si *K*-edge EXAFS data for different SiC surface structures measured by using Auger yield at both normal emission (dashed lines) and an emission angle of 70° (solid lines). For comparison, theoretical calculated curves for 6*H*-SiC and Si are also present. The curves from the bottom to the top are 1 × 1, 3 × 3, √3 × √3*R*30° and 6√3 × 6√3*R*30°, calculated 6*H*-SiC, and Si, respectively. The arrow indicates the first coordination of Si atom in Si lattice.

The Fourier transform of the measured EXAFS spectra after k^3 weighting using WINXAS are presented in figure 3.10. The local structural changes around Si atoms upon annealing for different surface reconstructions are clearly resolved. For a clearer illustration, theoretical curves using FEFF are also shown for both 6*H*-SiC and Si in figure 3.10.[124] The first peak in the calculated curve of 6*H*-SiC corresponds to the first Si–C coordination at 1.4 Å, and the second peak at 2.4 Å is from the Si–Si

coordination. In the case of Si which has a diamond-like structure, the first peak of Si–Si coordination is calculated at about 1.9 Å and the second peak for the next nearest neighbor at 3.4 Å. The calculated curves are consistent with the experimental data in the literature.[123, 125, 131] For the primitive 1 × 1 surface, the first two peaks for normal emission and grazing emission are at the same locations with the calculated 6*H*-SiC phase. For the 3 × 3 reconstruction, it is clear that the curve at normal emission has its first two peaks located at the same positions as the primitive surface in figure 3.10. However, the curve at grazing emission angle looks quite different: although the first peak remains at 1.4 Å, the second peak is located at about 2 Å. Compared to the theoretical calculations, the second peak is attributed to Si-Si coordination on the surface due to the high surface sensitivity at grazing emission angle. Our EXAFS results thus indicate the existence of Si clusters on this reconstructed surface. This is consistent with the Starke model where Si tetramers form atop the surface.[18, 19] As the 3 × 3 reconstruction was obtained by Si dosage at high temperature, it is reasonable that Si clusters form on the surface.[19, 59]

For the √3 × √3*R*30° reconstruction, the normal emission curve is almost identical to the calculated one for 6*H*-SiC due to the deeper probing. For the curve measured at grazing angle, the first peak is weak and the second peak become much broader and centered at 2.5 Å. This suggests that the coordination of Si atoms on this reconstruction is more complicated. There could be Si–Si bonds formed on the surface with different bond lengths and different phase shifts, which causes the first peak of the Si cluster to almost vanish and merge with the second peak of primitive

6*H*-SiC. This observation is consistent with the adatom model of this reconstruction, where silicon adatoms at T_4 site bond to silicon atoms in the underlying bilayer. For the $6\sqrt{3} \times 6\sqrt{3}R30°$ reconstruction, the curve for normal emission still resembles the SiC phase. However, for the curve measured at grazing angle, the peak corresponding to Si–Si coordination at 2 Å from Si clusters is very clearly resolved beside the first peak corresponding to the Si–C coordination. As the probing depth of AEY at normal emission is 3.7 nm and that at 70° reduced to 1.3 nm, it can be concluded that Si clusters remain on this reconstructed surface even though the surface is no longer Si rich. This finding is consistent with our XPS data, where a small peak at originated from silicon-silicon bonds is observed.

In conclusion, the investigation of silicon atoms in SiC nanomesh is done by the XAS method. Concrete evidence of Si vacancies in the bulk has been found by NEXAFS studies in FY mode. These observations suggest that Si atoms from deeper layers diffuse to the surface upon annealing leaving vacancy defects as deep as several micrometers. For the EG on SiC substrate, the Si vacancy concentration can reach as high as about 15%. We also found Si clusters in the surface region of SiC nanomesh by EXAFS studies using surface-sensitive AEY mode at grazing angle. The outdiffusion of Si atoms from the interior of SiC contributes to these clusters and creates both surface and bulk disorders in the SiC nanomesh.

3.3 Summary

In this chapter, the structure of the SiC nanomesh is studied by XPS, XAS and STM. In XPS, both Si *2p* and C *1s* spectra show dependence on the duration of annealing, suggesting that the surface should be regarded as the dynamic self-organization as opposed to a static surface reconstruction. In XAS, the silicon atoms in the SiC nanomesh are studied. Bulk silicon vacancies and surface silicon clusters are revealed in the SiC nanomesh and EG samples. These silicon-related defects indicate that the SiC nanomesh contains both surface and bulk disorders. The surface disorders are also studied by STM, where the SiC nanomesh shows apparent topographic disorders at short and medium length scales but has a good long range order. Based on these studies, the disorders in the structure of SiC nanomesh are proposed to be an intrinsic character of its dynamic self-organization rather than due to imperfections during surface preparation.

CHAPTER 4 OXIDATION OF THE 6*H*-SiC (0001) NANOMESH SURFACE

4.1 Introduction

SiC nanomesh is an inert surface which can survive in ambient conditions. Its inertness is an important advantage in nanotemplate applications. This surface is also the precursor layer and the interfacial layer of EG. It can be converted into EG at 1200°C in UHV or at 1650°C in argon atmosphere of about 1 bar.[132] These processes are attributed to the out-diffusion of silicon atoms accompanying the formation of sp^2 bonding of excess surface carbon atoms. Although extensive studies have been devoted to EG on SiC, only a few papers have reported the transition from the SiC nanomesh to EG.[28, 48, 50, 58] Due to uncertainties in the atomic structure of the SiC nanomesh, various models of the transition including bottom-up mode,[42] finger-like growth mode,[44, 48] step edge growth mode,[133] and island growth mode[46] have been proposed based on experimental observations. In all these models, the SiC nanomesh is assumed to be a graphene-like layer covalently bonded to the SiC substrates, and the transition is explained as a bond-breaking and the top layer release process. However, due to the high transition temperature (~1200°C), the generation of graphene is always accompanied by the emergence of a new SiC nanomesh layer below the graphene layer.[42] Thus, it is difficult to directly observe the nanomesh-graphene transition.

Due to the underlying nanomesh layer, EG on SiC nanomesh shows two distinct difference from exfoliated graphene. First, this EG layer has a "6 × 6" modulation in its STM images. Second, this EG layer is also *n*-doped by the nanomesh layer, causing its Fermi level to be 0.3eV higher than its Dirac point.[39, 43] To remove these two differences, the EG layer needs to be electronically isolated from the nanomesh layer. One proposed method is to transfer the EG layer to another substrate. However, this method is time-consuming and may reduce the quality of the EG layer during transfer.[134] Recently, a quasi-free standing graphene layer is generated by the atomic hydrogen intercalation to the SiC nanomesh.[52] However, the intercalation of hydrogen atoms is not stable, as it can be removed by annealing at about 900°C. Herein, we proposed to use oxygen instead of hydrogen to transform the SiC nanomesh into graphene at a temperature lower than the nanomesh formation temperature. This graphene is isolated from the SiC substrate by silicon oxides clusters formed by oxidation of silicon atoms in the SiC nanomesh. The oxidation process is temperature sensitive and occurs at temperatures as low as 600°C, suggesting a viable route to directly study the nanomesh-graphene transition and the formation of a silicon oxide buffer layer.

In this chapter, the SiC nanomesh on SiC(0001) is oxidized at oxygen partial pressures of around 5×10^{-4} torr from 600°C to 1050°C. The oxygen gas is introduced into the UHV chamber via a leak valve. The total dosage of oxygen is measured in Langmuirs (L), where1 Langmuir corresponds to an exposure of oxygen partial pressure at 1×10^{-6} torr for 1 second. XPS and STM measurements were performed to

monitor changes incurred by oxidation. The oxidation transforms the SiC nanomesh into graphene with the formation of silicon oxides at the interface. This oxidation shows a similar intercalation effect to that by hydrogen. However, the silicon oxides can endure higher temperature than hydrogen silicon bonds and decompose at 1050°C.

4.2 Results and Discussion

4.2.1 Photoemission study of SiC nanomesh oxidation

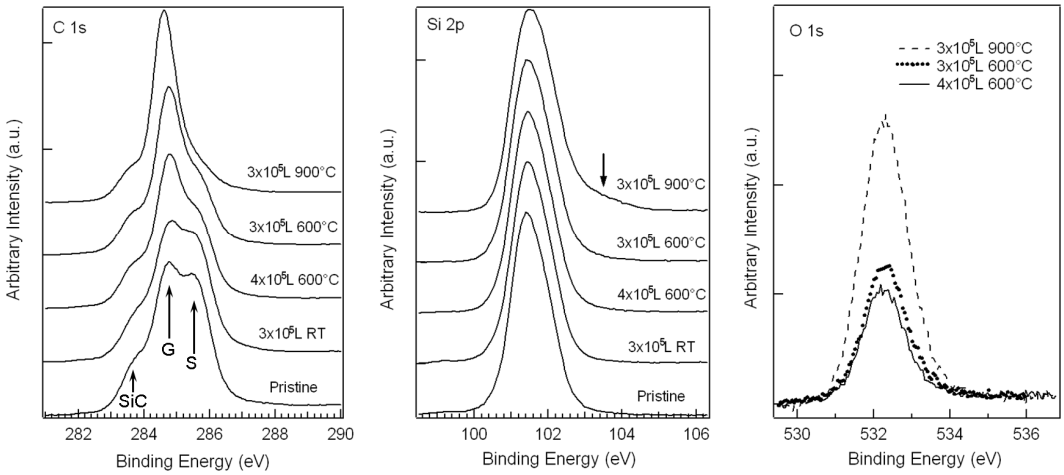

Figure 4.1. XPS spectra of nanomesh sample at successive oxidation steps. Left, C *1s*; Middle, Si *2p*; and Right, O *1s*.

The core level XPS spectra of oxidized SiC nanomesh sample at different temperatures and dosages are shown in figure 4.1. The spectra for pristine sample are in good agreement with figure 3.1 except that the central C *1s* G peak slightly is stronger than its high-binding-energy shoulder. This difference indicates that this sample is slightly over annealed. This over-annealing is desired, because it eliminates

the √3 × √3R30° reconstructions which can react with oxygen at room temperature.[135] The over-annealing of this sample generates small regions of graphene on its surface which is observed in STM images (figure 4.3). However, the EG layer appears inert and does not participate in the oxidation reaction. The pristine sample is exposed to an oxygen dosage of about 3×10^5 L at room temperature. No change in the C *1s* or Si *2p* spectra is observed. The inertness of the sample at room temperature is not surprising as the SiC nanomesh is stable in ambient conditions. The sample is then heated to 600°C with another 4×10^5 L dosage. At this temperature, the central G peak in C *1s* spectrum (blue line) increases with the decrease of high binding energy shoulder (S peak). The emergence of O *1s* peak confirms that the oxidation reaction has occurred. Interestingly, the successive oxygen doses at the same temperature cause no distinct changes in XPS spectra (green line), suggesting that the oxidation is probably saturated at this temperature. When the temperature increases to 900°C, further changes in the C *1s* and O *1s* spectra are observed. In the C *1s* spectrum, the S peak is heavily suppressed and the G peak becomes the dominant peak. The lineshape of C *1s* is now similar to EG on SiC. In the O *1s* spectrum, the intensity increases again, suggesting that the further oxidation occurs at higher sample temperatures. In addition, a small shoulder located at the higher binding energy side of bulk silicon peak becomes prominent. This shoulder indicates that some silicon atoms are oxidized and have higher binding energies.

To further investigate the oxidation reaction, peak-fitted core level spectra of pristine sample and oxidized sample (after oxidation at 900°C) are shown in figure

4.2. After the oxidation, the peak fitting of C *1s* spectrum shows the increase of G peak (284.8eV) and the decrease of S peak (285.4eV). These changes accord with the transition from nanomesh to graphene at 1200°C in the absence of oxygen. The

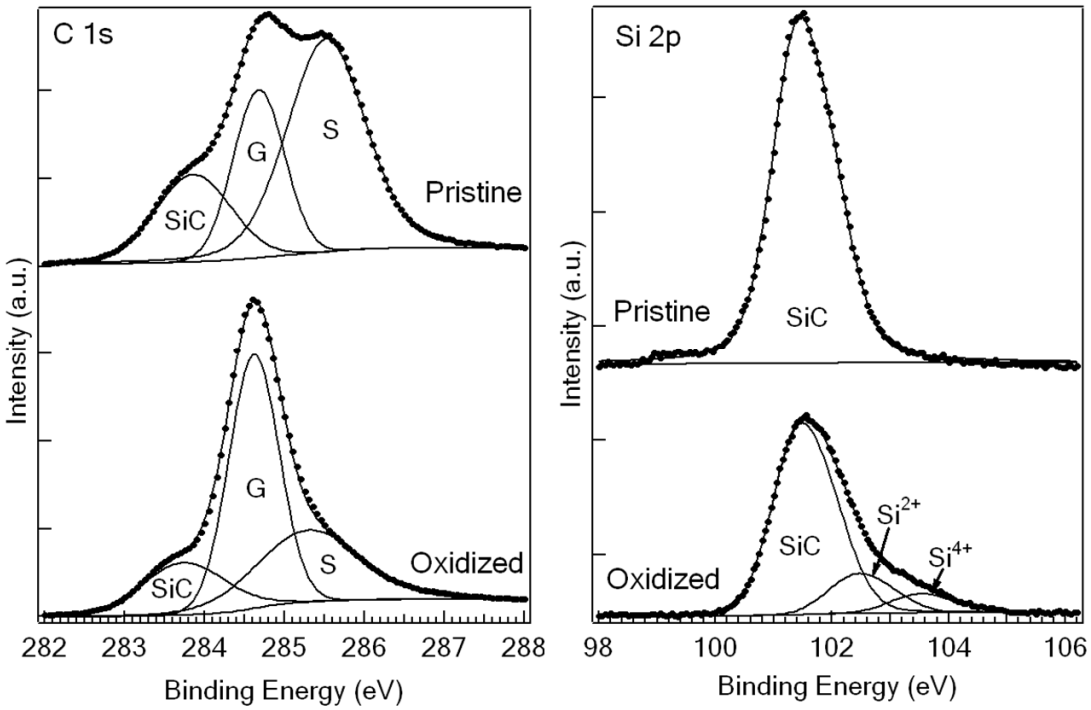

Figure 4.2. Core level photoemission spectra of pristine and oxidized SiC nanomesh sample. Left, the C *1s* spectrum, three components are resolved in this figure. SiC refers to the bulk SiC component, G to the graphene related component, and S to the nanomesh related surface component. Right, the Si *2p* spectrum, shows two additional oxide-related components after oxidation. The inset shows the intensity of O *1s* peak at different oxidation stages.

oxidized sample also shows a similar C *1s* spectrum lineshape as graphene. Thus, the nanomesh oxidation induces the nanomesh-graphene transition. In the Si *2p* spectrum, peak fitting shows two new components at 102.4eV and 103.5eV in addition to the bulk related SiC component at 101.4eV. These two components shifted by 1.0eV and 2.1eV relative to the SiC bulk component are assigned to Si^{2+} and Si^{4+} oxidation states.[21] In the investigation of Virojanadara *et al*.,[136] oxidation of the Si-

terminated SiC surface created Si^{+} and Si^{4+} oxidation states while the C-terminated surface created Si^{2+} and Si^{4+} oxidation states. Their results suggest the surface termination could affect the formation of oxidation states. They concluded that the silicon-rich SiC surface prefers to form Si^{+} and Si^{4+} oxidation states whereas the carbon-rich SiC surface prefers to form Si^{2+} and Si^{4+} states. This conclusion is in good agreement with formation of Si^{2+} and Si^{4+} oxidation states in nanomesh oxidation, as the nanomesh surface is carbon-rich. The thickness of silicon oxides can be roughly estimated by the attenuation of bulk Si *2p* intensity before and after oxidation. From the Si *2p* spectra in figure 4.2, the thickness of the oxide layer is calculated to be about 3.7Å, larger than the size of silicon dioxide tetrahedron (2.2 Å). However, this thickness is overestimated as the decrease of Si *2p* intensity comes partially from the oxidation of silicon atoms in the SiC nanomesh. Thus, XPS attenuation data only provides the upper limit of the silicon oxide thickness.

4.2.2 STM study of nanomesh surface oxidation

To understand how the nanomesh is oxidized, the SiC nanomesh surface is progressively oxidized at 650°C, 750°C, 900°C to 1050°C. The same oxygen partial pressure as in XPS study is used during each oxidation step. The morphology of the oxidized sample at each step is then imaged by STM.

According to the XPS measurements, oxidation of nanomesh at elevated temperature generates silicon oxides on the surface, and the SiC nanomesh surface gradually changes into the graphene surface. The corresponding STM images of the

oxidized nanomesh surface are shown in figure 4.3. After oxidation at 650°C, irregular shaped corrugations (indicated by green arrows) appear on the surface. These corrugations cover about 22% area of nanomesh terraces. The XPS data

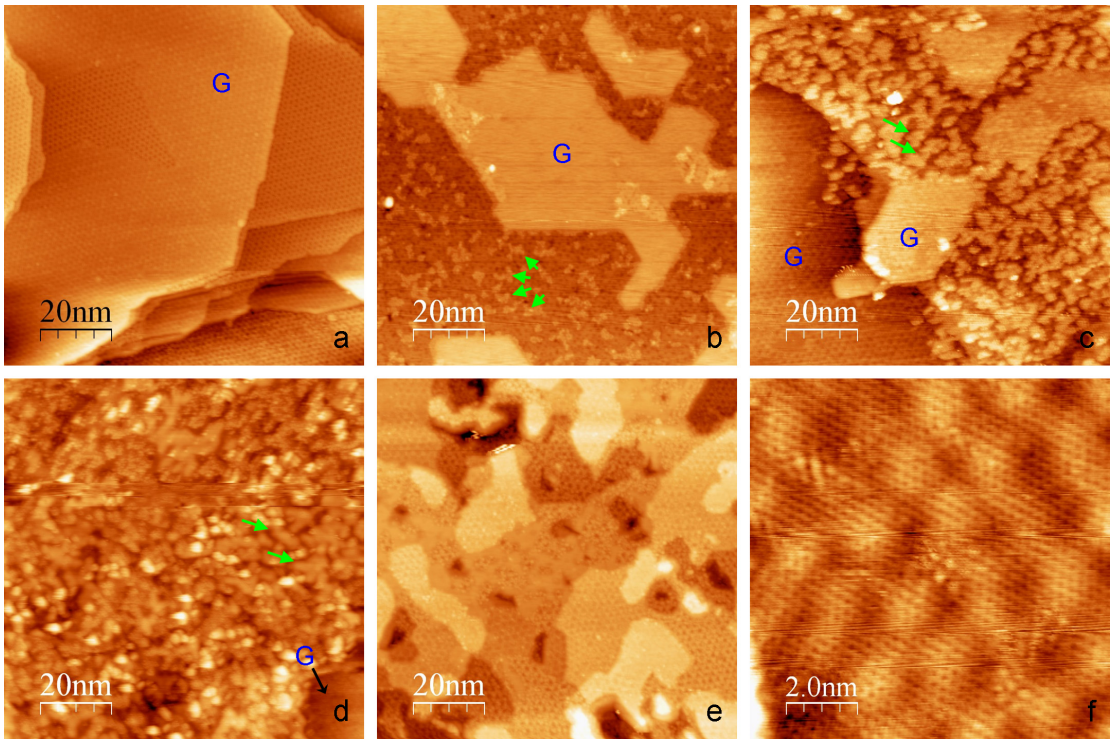

Figure 4.3. The SiC nanomesh surface at different oxidation temperatures. a. pristine SiC nanomesh sample (V_T =2.2V, I_T =0.2nA); b. 650°C (V_T =-2.1V, I_T =70pA); c. 750°C (V_T =2.0V, I_T =70pA); d. 900°C (V_T =1.0V, I_T =70pA); e. 1050°C (V_T =1.9V, I_T =70pA). The size of a-e is 100 × 100nm^2. f. a representative graphene terrace on SiC nanomesh from d (10 × 10nm^2, V_T =0.5V, I_T =70pA).

suggest that these corrugations are the oxidation induced silicon oxide clusters. These clusters grow in size at 750°C, covering 64% of the total nanomesh area. At 900°C, nearly all the nanomesh terraces are covered with the clusters (86% in area). The thickness of these clusters is about several angstroms, consistent with the XPS measurement. However, most clusters disappear when the temperature reaches 1050°C; small flakes and pits appear on the surface. The 6 × 6 lattice is also restored

on most terraces. As Si atoms in the clusters are in the 2+ and 4+ oxidation states, these clusters are metastable SiO_x rather than thermally stable SiO_2. At 1050°C, these clusters are probably dissociated and accompanied by the restoration of SiC nanomesh.

It is worth noting that oxidation only occurs at the SiC nanomesh terrace and not in regions where EG has already formed. The EG surface can be clearly identified in figure 4.3 (terraces marked by blue "G"), as graphene network is observed in STM scan (figure 4.3f). About 5% to 10% of total surface area is covered with EG on the pristine SiC nanomesh surface. Interestingly, no silicon oxide cluster is generated on EG surface at all temperatures. Obviously, the graphene layer is inert to oxidation at the temperature up to 1050°C. Moreover, the "6 × 6" corrugation in EG is also unchanged during oxidation, indicating that the interfacial SiC nanomesh layer is prevented from oxidation due to the protection of the EG top layer. The observed EG on SiC nanomesh sample (figure 4.3a-e) is attributed to the slight over annealing during the preparation of SiC nanomesh, as confirmed by the C *1s* XPS spectrum.

To investigate the oxidation induced clusters, filled state and empty state higher resolution STM images of oxidized nanomesh sample at 900°C are shown in figure 4.4. It is obvious that these clusters are covered with a continuous graphene layer. The continuity of graphene layer can be observed from figure 4.4, where the graphene network is continuous from one bump to another. Despite the graphene layer is slightly distorted by the corrugations beneath it, the graphene in the form of the 1 × 1

graphene lattice area (blue vectors) and √3 × √3R30° superstructures is shown in figure 4.4. Two types of √3 superstructures with complementary shapes

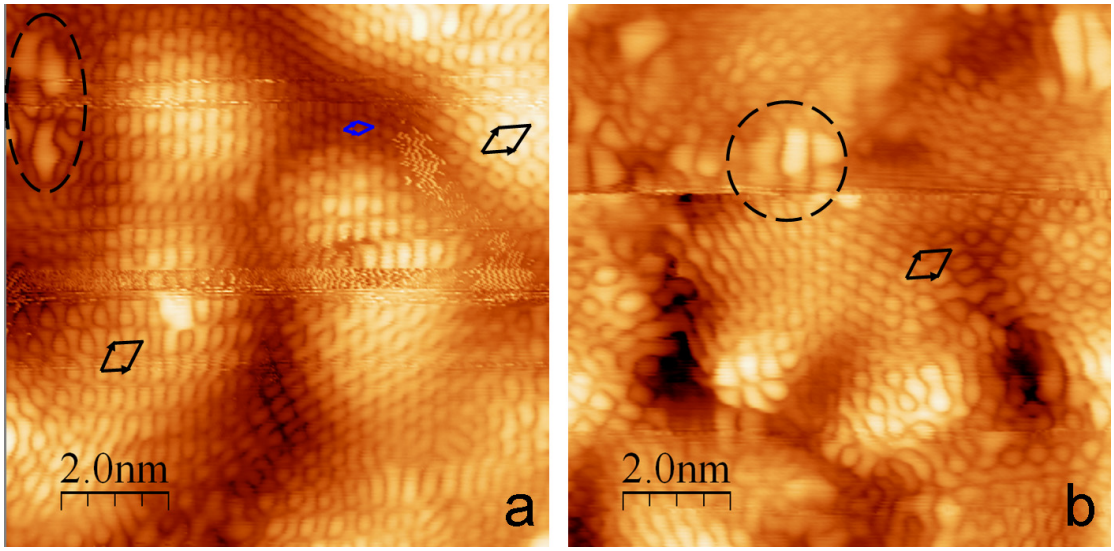

Figure 4.4. Graphene networks on oxidized nanomesh surface. a). filled state image (10 × 10nm^2, V_T = 0.5V I_T = 70pA); b). empty state image (10 × 10nm^2, V_T = -0.5V I_T = 70pA). The blue vectors represent the 1 × 1 graphene lattice and the black vectors represent the √3 × √3R30° reconstructed graphene lattice. Panel a and panel b are not the same locations.

(bright rings and dark rings) are highlighted by the black vectors in Figure 4.4a. Both superstructures have previously been observed close to the defects and boundaries of graphene [137-139] and their origins are attributed to the perturbation of graphene charge density. The √3 superstructure induced by this perturbation has the same physics origin as the Friedel oscillation.[140] Specifically, it can be understood by a phase shift induced by defects to one of the atoms in the graphene basis. This shift causes half the carbon atoms in the graphene sheet to become invisible and the remaining carbon atoms in the graphene to give rise to the √3 superstructure in graphene.[140, 141] Using a conductive AFM tip to simultaneously obtain current

image and topography image of a defective HOPG surface, Ruffieux *et al.* successfully proved that √3 superstructure has a LDOS origin and possesses an identical structure to the undisturbed graphene networks.[139] Thus, the observation of the graphene network confirms the nanomesh-graphene transition by oxidation. On this surface, defects with anomalous electronic structures are observed close to the √3 superstructures (dashed circles in panel a and b of figure 4.4). These defects probably serve as perturbation centers to the graphene superstructures. They also resemble the electronic structure of the SiC nanomesh [29, 42] and can be regarded as residual SiC nanomesh structures due to incomplete nanomesh-graphene transition at low temperature (900°C).

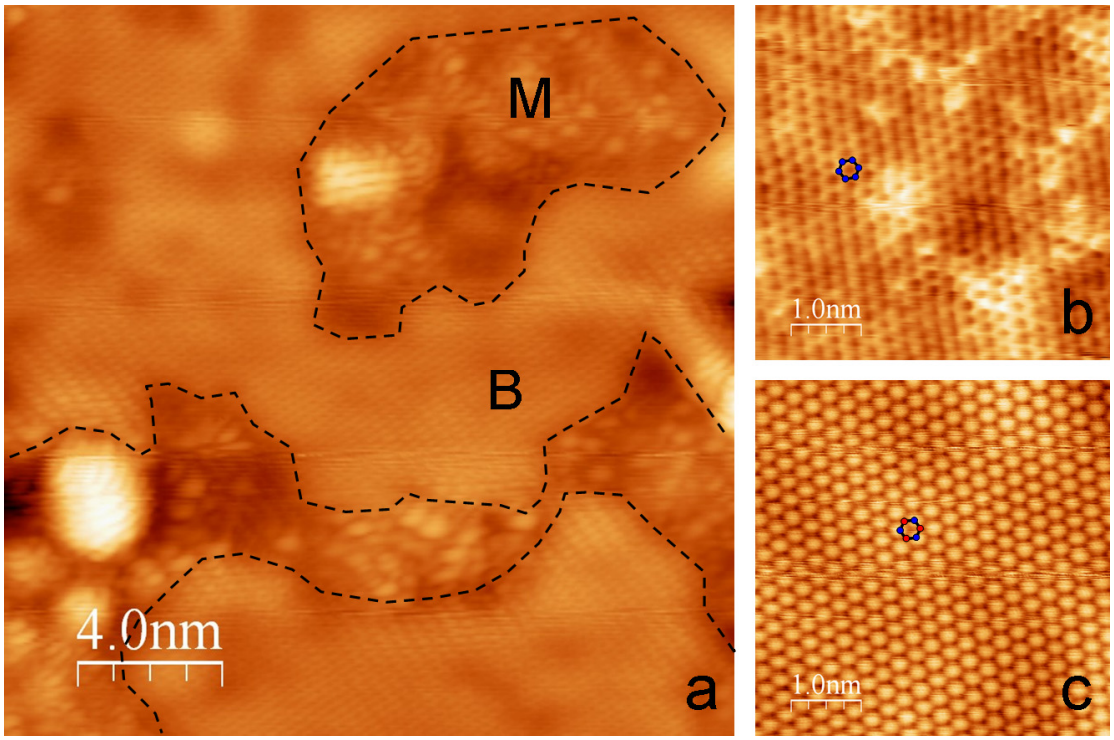

Figure 4.5. Graphene networks on the nanomesh sample oxidized at 1050°C. a. 20 × 20nm^2 image of the SiC nanomesh sample after oxidation (V_T = 1V I_T = 70pA). The surface is covered by monolayer graphene (marked by "M") or bilayer graphene (marked by "B"). One monolayer graphene region is marked by dash line; b. a representative "M" region (5 × 5nm^2, V_T = 0.5V I_T = 70pA); c. a representative "B"

region ($5 \times 5nm^2$, $V_T = 0.5V$ $I_T = 70pA$). A hexagon is shown in panel b and c to highlight graphene lattice. AB stacking can be clearly resolved in panel c.

Unlike hydrogen intercalation,[52] where SiC nanomesh can be restored at 900°C, the partially formed graphene network by oxidation cannot be restored to the SiC nanomesh. This partially formed graphene is transferred into complete single layer or bilayer graphene terraces when the temperature reaches 1050°C. In figure 4.5, the SiC nanomesh related structures are eliminated and the surface is covered by graphene only. Two regions with different surface morphology can be distinguished. The region marked by "M" is covered by monolayer graphene. Due to the high bias (1V), graphene layer appears transparent and electronic structure of SiC nanomesh interlayer is shown. The other region marked by "B" is covered by the graphene network, indicating that this region is covered by bilayer graphene.[42] The transparency of single layer graphene under high bias on SiC(0001) surface has already observed in a previous report.[42]

When bias is reduced to 0.5V, monolayer and bilayer regions can be clearly resolved in figure 4.5b and figure 4.5c, respectively. A hexagon is shown in two panels to highlight the hexagonal graphene lattice. In panel b, all six corners of hexagon are shown in same height (6-fold symmetry). In panel c, these corners are alternatively in high and lower height (3-fold symmetry), confirming the AB stacking of bilayer graphene.[142] The formation of bilayer graphene is probably due to the further transition from SiC nanomesh to graphene, as suggested in chapter 3, while the annealing temperature of 1050°C is high enough for the nanomesh-graphene

transition. The "6 × 6" corrugations reappear below the graphene layer indicating regeneration of the SiC nanomesh. Hence, it can be concluded that oxidation of the SiC nanomesh at 600°C to 900°C induces the nanomesh-graphene transition. When the temperature reaches 1050°C, the SiC nanomesh regenerates below the graphene top layer even with the presence of oxygen. The silicon oxide clusters generated previously are unstable at this temperature and dissociate. The partial graphene layer is converted into a complete graphene layer at this temperature. Thus, oxidizing the SiC nanomesh at temperatures lower than 900°C provides a possible route to study the nanomesh-graphene transition.[44] Due to the continuity of top graphene layer, the detailed information about underlying oxides clusters could not be obtained. Future studies are needed, for example using surface diffraction methods, to elucidate details of this oxidation model.

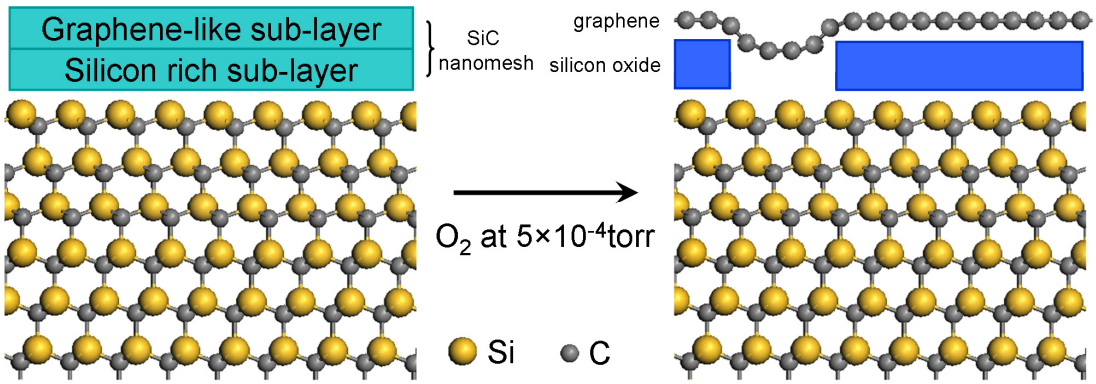

Figure 4.6. Schematic model of SiC nanomesh during oxidation at 900°C. Left, pristine SiC nanomesh surface; right, graphene layer and silicon oxide clusters on SiC substrate. The cluster nature of silicon oxide causes the corrugation amplitude of the graphene layer.

The observation of silicon oxide underneath graphene also provides clues to the atomic structure of the SiC nanomesh. Since the generated graphene is always on top, it can be deduced that the SiC nanomesh is composed by two sub-layers: the upper sub-layer is carbon-rich [28, 58] and is able to transform into single layer graphene during oxidation whereas the lower sub-layer is silicon rich and can react with O_2 to form the silicon oxide clusters (Figure 4.6). The oxidation of the lower sub-layer causes the breaking of the bonds between two sub-layers and leads to the oxidation of silicon atoms. This result could provide an additional clue to the structure models of SiC nanomesh proposed by Hass *et al*.[56] The conclusion that silicon atoms are below the carbon atoms favors their Si-down adatom model or C adatom model, but is not consistent with the Si-up adatom model for the SiC nanomesh.

4.3 Summary

In summary, oxidation of SiC nanomesh at elevated temperature is studied by XPS and STM. Oxidation of the SiC nanomesh converts this layer into graphene networks with silicon oxide clusters formed at the interface beneath at 600°C to 900°C. These silicon oxide clusters probably decompose at 1050°C and disappear from the interface. The graphene network formed between 600°C and 900°C appears as √3 superstructures due to the perturbation of residual nanomesh structures. At 1050°C, the partially formed graphene networks convert into a complete sheet consisting of both single layer and bilayer graphene terraces. On the other hand, no

change is observed on pre-existing graphene terraces, suggesting the graphene layer is not only inert to oxidation but also prevents the underlying nanomesh layer from oxidation. The conversion of nanomesh to graphene by oxidation is slow and temperature-sensitive, providing a route to probe the transition from SiC nanomesh to graphene. The formation of a silicon oxide interlayer between graphene and SiC may hold promise for the fabrication of graphene devices electrically insulated from the substrate.

CHAPTER 5 TEMPLATE EFFECT OF 6*H*-SiC (0001) NANOMESH SURFACE ON ORGANIC MOLECULES

5.1 Introduction

As mentioned in section 1.2, natural and artificial nanotemplates are widely used in the formation of nanostructures. The application of these nanostructures includes tailoring surface properties and surface nano-engineering.[40, 143-145] Before creating a nanotemplate, the molecule-substrate interaction needs to be understood. If the molecule-substrate interaction is too weak, absorbed molecules can easily overcome it and form crystalline or other periodic structures driven by the intermolecular interactions. Examples include atomically flat inert surfaces, such as highly ordered pyrolytic graphite (HOPG)[146-148] and MoS_2[149, 150], or atomic flat metallic surfaces, such as Ag(111)[103, 151, 152] and Au(111)[153-156], have been used as substrates to form molecular thin films or networks by directional (such as hydrogen bonding[70] or metal-organic coordination[73]) or non-directional (such as π-π interaction[146]) intermolecular interactions. On the other hand, if the interaction is too strong, absorbed molecules have very short diffusion length, and are basically trapped at the place where they land. Thus, no long-range order can be generated. Examples can be found on active surfaces such as Si(111)[157-159] or Si(100)[160, 161] where adsorbates are anchored into substrate-induced configurations by covalent bonding. As expected, no lateral long range order can be

found on these surfaces. Thus, the strength of the molecule-substrate interaction should be carefully selected in a useful molecule-nanotemplate system.

Many artificial nanotemplates, such as supramolecular porous networks,[70, 73, 76] are suitable nanotemplates to trap one or more target molecules into the pores to form molecular arrays. However, due to the diffusion barrier caused by the networks, most studies only managed to fill part of surface pores by the target molecules before the condensed phase forms.[70, 73, 76] Only a few papers have successfully reported co-adsorbed planar target molecules including copper phthalocyanine (CuPc), coronene or hexabenzocoronene (HBC) into the host networks built by the star-shaped stilbenoid compound such as 1,3,5-tris[(E)-2-(3,5-didecyloxyphenyl)-ethenyl]-benzene (TSB35) or 1,3,5-tris(10-carboxydecyloxy) benzene (TCDB) to form ordered molecular arrays.[75, 162] However, such arrays could be regarded as 2D binary crystals instead of isolated arrays because the intermolecular interaction plays an important role in the confinement of the guest molecules.

In natural nanotemplates, molecular arrays can be formed by site-selective adsorption due to surface corrugation, such as 2D C_{60} clusters on vicinal gold surface,[77] 1-nitronaphthalene supramolecular clusters and chains on Au(111) reconstructed surface,[79] and C_{60} decoration on BN nanomesh surface.[82] In particular, the nanomesh surfaces with a periodicity of about several nanometers are the most promising template to form single molecular arrays. In this chapter, the template effect of SiC nanomesh surface for three types of organic molecules (C_{60}, CuPc and pentacene) is studied by combining STM and XPS. Lacking strong

molecule-substrate and intermolecular interactions, the geometric differences of the three molecules play important roles in the formation of the different supramolecular structures on this nanomesh surface. C_{60} with a spherical shape and smallest lateral size forms a close packed thin film. CuPc with a planar shape and four-fold symmetry has a compatible lateral size with the SiC nanomesh and forms a highly periodic molecular array. Pentacene, with a two-fold rectangular shape has a smaller lateral size than CuPc, facilitates several adsorption configurations forming a quasi-amorphous array with a mixture of different configurations.

5.2 C_{60} on the SiC nanomesh

5.2.1 STM study of C_{60} on the SiC nanomesh

As reported in the previous work in our group, C_{60} forms close packed islands on the SiC nanomesh at submonolayer coverage (figure 5.1).[163] This observation suggests that the substrate has little effect in constraining the morphology of C_{60} adsorbates. To probe the interaction between C_{60} and the SiC nanomesh, the growth of C_{60} from submonolayer to multilayer region is studied by *in-situ* STM and shown in Figure 5.2. At C_{60} coverages far below 1 ML, C_{60} molecules form irregularly shaped single-layer islands mainly decorating the terrace edges, as shown in figure 5.2(a) for 0.2 ML coverage. Upon increasing the coverage to 0.5 ML, 0.7 ML and 0.9 ML (figure 5.2b, 5.2c and 5.2d respectively), these small islands coalesce to form continuous irregularly shaped single layer islands. At about 1 ML coverage, a complete wetting layer of C_{60} grows epitaxially on the SiC nanomesh, as shown in

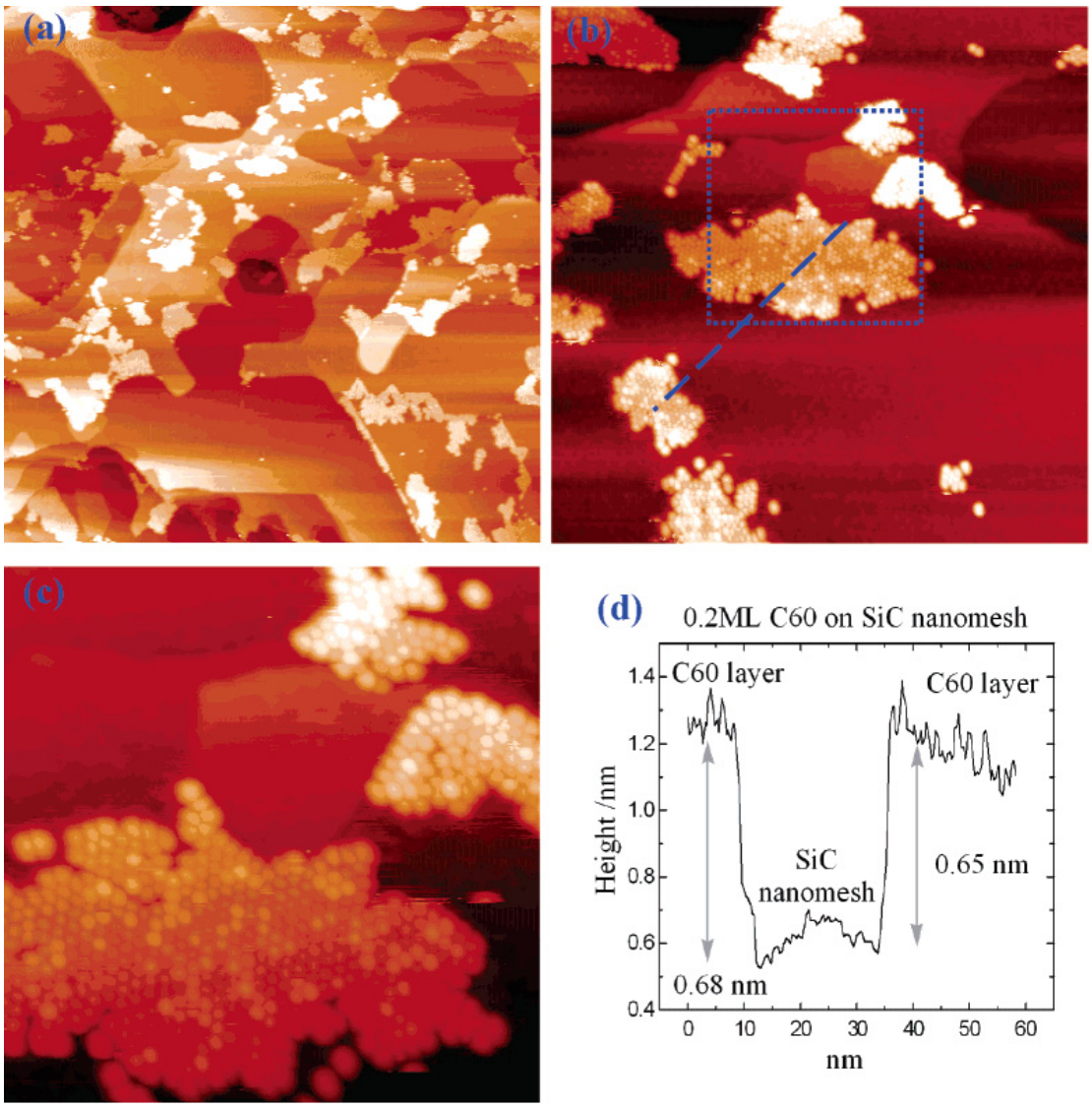

Figure 5.1. C_{60} on SiC nanomesh surface. (a) 500 × 500 nm^2, (b) 100 × 100 nm^2, (c) corresponding detailed 40 × 40 nm^2 image of C_{60} single-layer island as highlighted by dashed squares in panel b, and (d) the line profile as marked by the dashed line in panel b. I_T = 30 pA and V_T = +1.4 V. (Reproduced with permission from [163])

figure 5.2(e). On top of these C_{60} single-layer islands, no second layer C_{60} islands were found in all areas imaged, suggesting a good wetting property of C_{60} molecules on SiC nanomesh. Increasing the coverage to 1.4 ML (figure 5.2f), compact irregularly shaped C_{60} single islands nucleate on top of the wetting monolayer. These islands exhibit some degree of fractal shape instability with a fairly isotropic

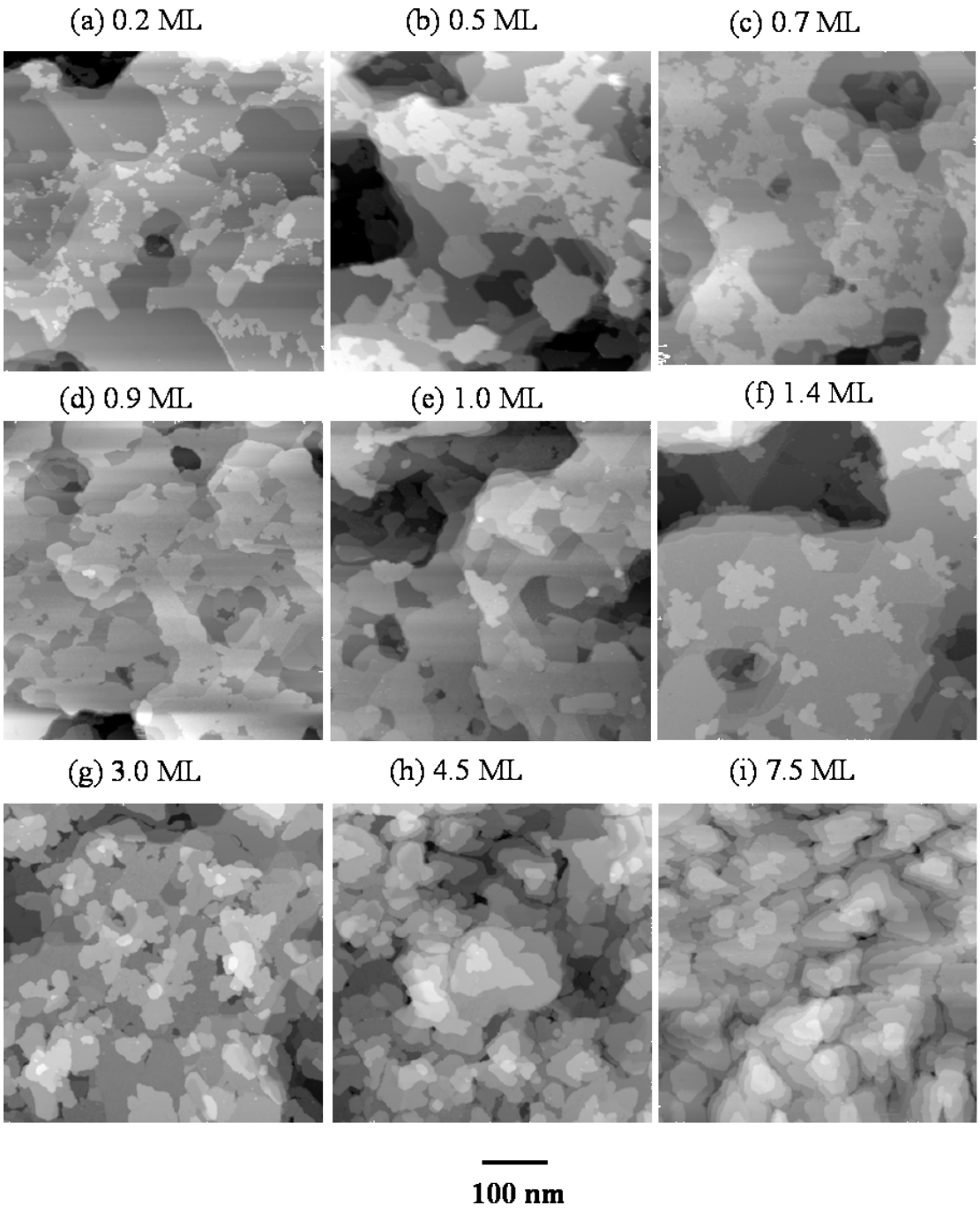

Figure 5.2. 500 × 500 nm^2 STM empty state images of SiC nanomesh with C_{60} coverage of (a) 0.2 ML, (b) 0.5 ML, (c) 0.7 ML, (d) 0.9 ML, (e) 1.0 ML, (f) 1.4 ML, (g) 3.0 ML, (h) 4.5 ML and (i) 7.5 ML.

structure. On top of these C_{60} second-layer islands, no third-layer islands were found in all areas imaged which indicates a layer-by-layer growth. At 3.0 ML, more

compact irregularly shaped islands form (figure 5.2g). Upon further increasing the coverage to 4.5 ML (figure 5.2h) and 7.5 ML (figure 5.2i), the growth of C_{60} on SiC nanomesh was found to transit to island mode, revealing a typical Stranski-Krastanov growth mode (layer plus island).[163]

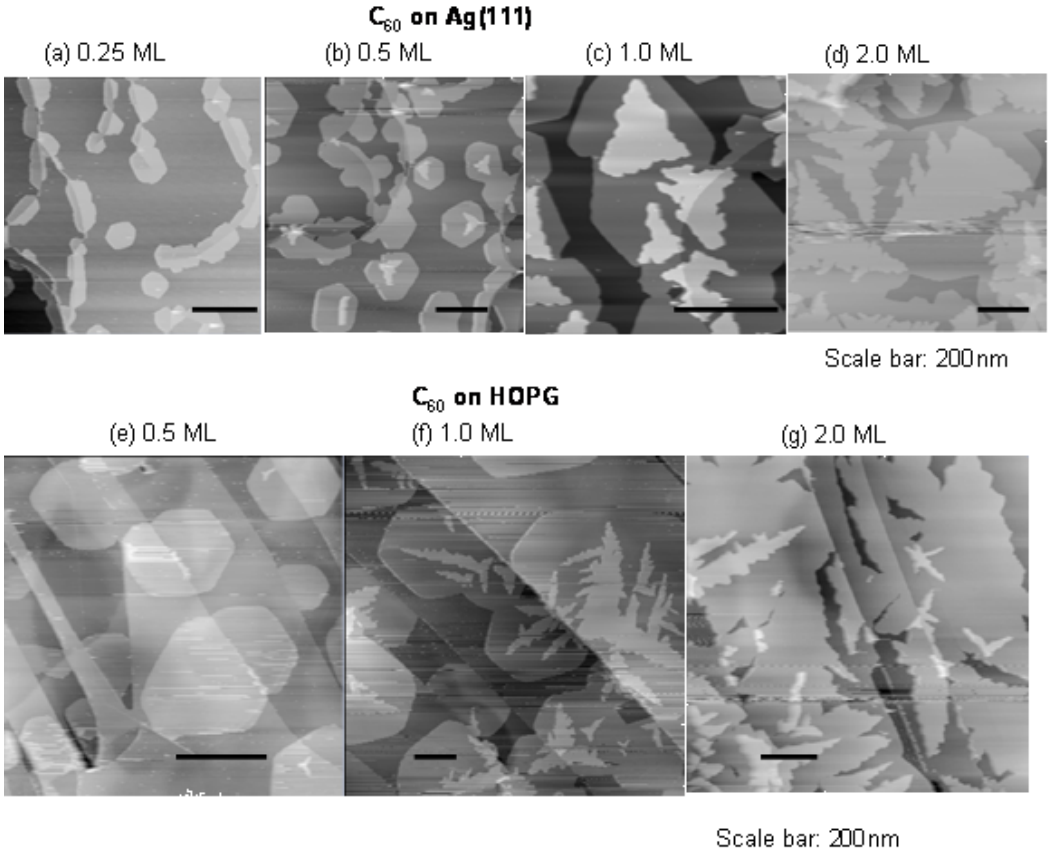

Figure 5.3. STM images of C_{60} on Ag(111): (a) 0.25 ML, (b) 0.5 ML, (c) 1.0 ML, (d) 2.0 ML; and C_{60} on HOPG: (e) 0.5 ML, (f) 1.0 ML, and (g) 2.0 ML. The scale bar is 200 nm in all images.

Although the structure of the nanomesh surface is not fully elucidated, neither proposed models nor experimental results suggest dangling bonds on this surface.[28] As such, a chemical reaction is unlikely to occur at the C_{60}-nanomesh interface (*cf.* Section 5.2.2). In contrast, the Si dangling bonds on clean Si(111) or Si(100) usually

induce the formation of covalent bonds between C_{60} and Si substrates.[164] Thus the growth morphology is determined by non-covalent interactions. For comparison, the growth of C_{60} on Ag(111) and HOPG were also studied. At the interfaces of C_{60} on HOPG and C_{60} on Ag(111), there are no interfacial chemical reactions,[165, 166] similar to the C_{60}-nanomesh interface, but the strength of interaction between substrates and C_{60} varies. At submonolayer coverages, instead of irregularly shaped islands as observed on SiC nanomesh, hexagonally shaped C_{60} single-layer islands with smooth boundaries nucleate on Ag(111) (figure 5.3a for 0.25 ML coverage and figure 5.3b for 0.5 ML coverage) and HOPG (figure 5.3e for 0.5 ML coverage) surfaces. In contrast to a complete wetting layer of C_{60} on SiC nanomesh, the second-layer of C_{60} starts to nucleate on top of those incomplete C_{60} single-layer islands on Ag(111) and HOPG from 0.5 ML. Therefore, the growth of C_{60} on Ag(111) and HOPG at room temperature adopts a 3-D island growth mode (Volmer-Weber growth mode). This indicates the interactions with both substrates are weaker than on the SiC nanomesh. The difference in interaction strengths with the SiC nanomesh and graphene is discussed in section 5.3 and 5.4. From figure 5.3(c) and 5.3(d), the second- or third-layer of C_{60} on Ag(111) shows a rather different morphology that can be described as fractal shape with thick arms. The fractal shape is more pronounced for the second or thick layers of C_{60} on HOPG (figure 5.3f and 5.3g). As previously reported,[165] the observed distinct morphology difference between C_{60} monolayer and thick layers on HOPG is proposed to originate from the significantly different diffusion behaviors of C_{60} on the flat HOPG surface and on the surface of C_{60} islands.

C_{60} displays isotropic diffusion behavior on the flat HOPG and Ag(111) surfaces, but anisotropic diffusion behavior on the highly corrugated C_{60} surface with higher diffusion barrier, leading to the formation fractal-shaped C_{60} islands on top of C_{60} surface. Similarly, the irregularly shaped first C_{60} layer observed on SiC nanomesh can be attributed to the anisotropic diffusion of C_{60} on the highly corrugated nanomesh surface.

As shown in figure 5.2, it is clear that the transition from layer-by-layer to island growth mode of C_{60} on SiC nanomesh occurs at between 2-3 ML coverage. A similar transition has been observed for 3,4,9,10-perylene-tetracarboxylic dianhydride (PTCDA) on Ag(111),[167] which is attributed to the thickness dependent PTCDA interlayer transport barrier (E_{inter}), *i.e.*, for the first two layers, the interaction of PTCDA on Ag(111) lowers the E_{inter}, favoring the transport of PTCDA molecules from top layers to the lower layers closer to Ag(111), leading to layer-by-layer growth. At higher coverage, the influence of this binding is insignificant and E_{inter} is mainly governed by the Ehrlich-Schwoebel barrier (step-edge barrier),[168, 169] leading to 3-D island growth. The very similar growth mode transition of C_{60} on SiC nanomesh could, therefore, be attributed to the different binding strength of C_{60} molecules to the substrate and to neighboring C_{60} molecules, *i.e.*, the binding of C_{60} molecules to the substrate is stronger than to C_{60} molecules. As such, the absorbed C_{60} molecules in first two layers tend to wet the substrate, leading to a layer-by-layer growth. At higher coverage, the intermolecular interactions of the absorbed C_{60}

molecules begin to dominate, giving rise to a transition from layer-by-layer to 3-D island growth mode.

5.2.2 PES study of C_{60} on the SiC nanomesh

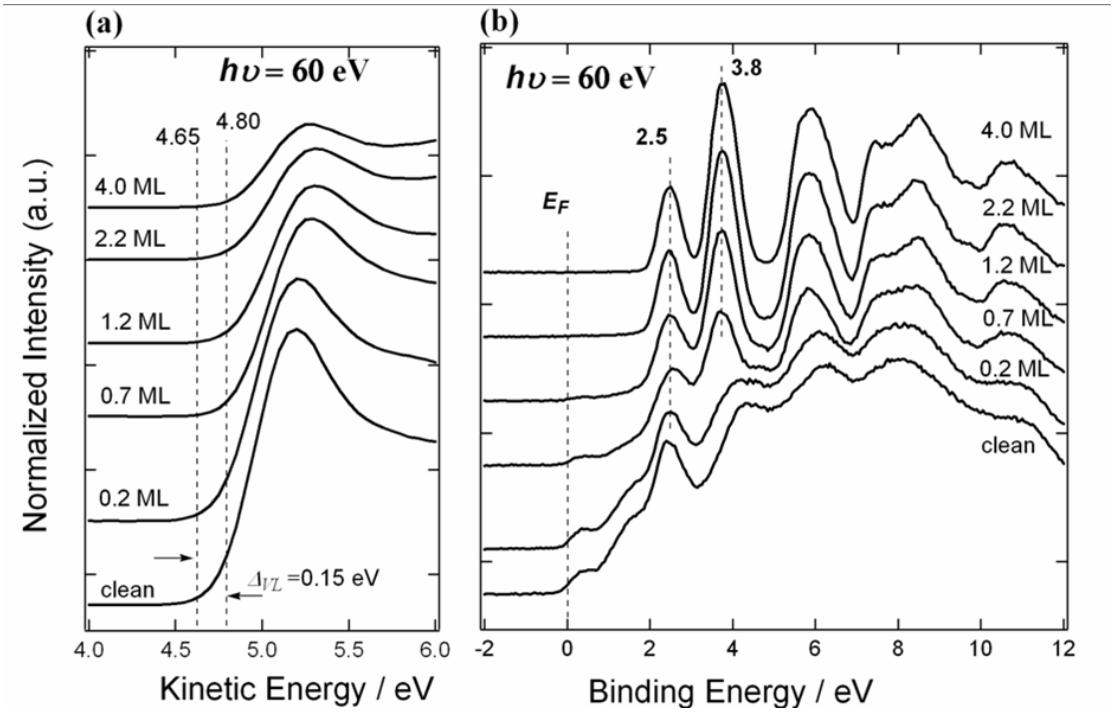

Figure 5.4. Synchrotron UPS spectra for C_{60} on SiC nanomesh with different coverage at (a) the low-kinetic energy part and (b) at the low-binding energy part. All spectra are measured with photon energy of 60 eV.

To identify the nature of the interfacial interaction for the wetting of C_{60} on SiC nanomesh, synchrotron-based photoemission spectroscopy is used. In figure 5.4a and 5.4b, representative PES spectra at the low kinetic energy region and the low binding energy region are shown as a function of C_{60} thickness, respectively. To determine the low kinetic energy onset, a negative 5 V sample bias is applied. The vacuum level (E_{vac}) of SiC nanomesh upon deposition of C_{60} is measured by linear extrapolation of

the low-kinetic energy onset (secondary electron cut-off) of PES spectra.[170] It is well known that the vacuum level of the substrate is extremely sensitive to the interface charge transfer after deposition, *i.e.*, an upward shift of the vacuum level occurs if electrons transfer from the substrate surface to the adsorbate overlayers, a downward shift occurs if electrons transfer from the adsorbate overlayers to the underlying substrate surface, or the vacuum level remains unchanged if no interface charge transfer takes place.[163, 170, 171] As shown in figure 5.4a, an upward shift of the vacuum level by 0.15 ± 0.05 eV is clearly observed after deposition of 0.7 ML C_{60}, revealing that a weak charge transfer occurs at the C_{60}-nanomesh interface involving electrons transferring from nanomesh to the C_{60} overlayer. The C_{60} HOMO (highest-occupied-molecular-orbital) is observed at 2.50 ± 0.05 eV (figure 5.4b). At 4 ML C_{60} coverage, the typical valence band spectrum of fullerene is observed without any apparent contribution from the SiC nanomesh substrate.[172, 173] It is found that the C_{60} HOMO peak position at 2.50 ± 0.05 eV, as well as the peak shape, remains unchanged with increasing thickness, suggesting that no chemical interactions occur at the C_{60}-nanomesh interface. In contrast to the van-der-Waals type interactions dominant at the C_{60}-HOPG interface,[174, 175] the interface interaction due to weak charge transfer at the C_{60}-nanomesh interface is stronger than the C_{60} intermolecular interaction[176] (e.g. van-der-Waals). Such relatively strong binding of C_{60} to SiC nanomesh lowers the E_{inter}, favoring the transport of C_{60} molecules from top layers to the lower layers closer to SiC nanomesh, facilitating the wetting of C_{60} on SiC nanomesh and leading to a layer-by-layer growth for the first two layers.

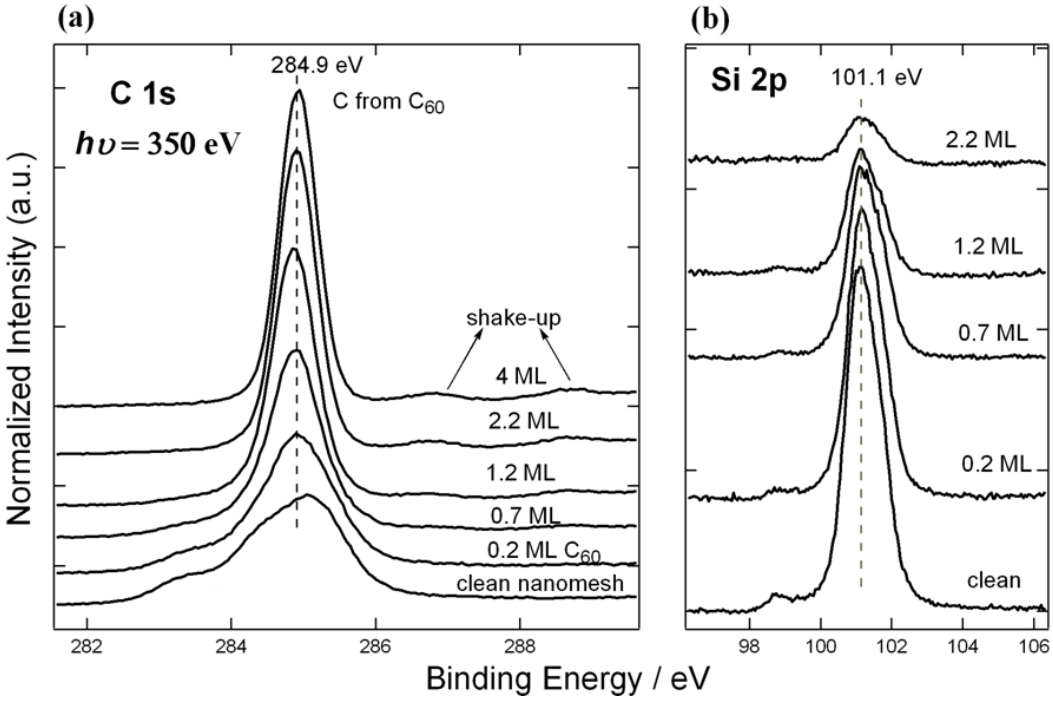

Figure 5.5. Synchrotron based core level PES spectra for (a) C *1s* and (b) Si *2p* of C_{60} on SiC nanomesh at different coverages (binding energy is relative to E_F of the electron energy analyzer). All spectra are measured with photon energy of 350 eV.

Figure 5.5 shows the evolution of C *1s* and Si *2p* peaks during the deposition of C_{60} on SiC nanomesh. The photon energy of 350 eV is chosen to enhance the surface sensitivity. Prior to deposition, the C *1s* spectrum of the clean SiC nanomesh can be found at the bottom of figure 5.5a. Two SiC nanomesh related peaks, with the stronger one located at 285.1 ± 0.05 eV, the weaker one at 284.0 ± 0.1 eV, and one bulk related weak peak at 283.0 ± 0.1 eV are shown in this spectrum. The lineshape of these three components is identical to our observations in chapter 3 (*c.f.* figure 3.1) and previous reports.[28, 51] Upon deposition of 0.2 ML C_{60}, the C *1s* main peak is shifted to lower binding energy at 284.9 ± 0.05 eV, which is attributed to the photo-excitation of C_{60}.[174, 177] This C_{60}-related component becomes dominant after increasing the coverage to 1.2 ML, indicating the surface was fully covered by C_{60}.

Upon increasing the coverage to 4 ML, the binding energy of C *1s* remained constant at 284.9 ± 0.05 eV. At the same time, neither a binding energy shift of Si *2p* nor a new Si *2p* component at all C_{60} coverages was observed (figure 5.5b). This suggests that no covalent or ionic bonding occurs at the C_{60}-nanomesh interface, which confirms that nanomesh can serve as a barrier layer to prevent the interaction between C_{60} and the underlying bulk SiC.

In summary, C_{60}-SiC nanomesh interface is studied using synchrotron-based PES and STM. A layer-by-layer followed by island growth mode (S-K mode) is identified for C_{60} deposition, suggesting that the adsorbate-substrate interaction is stronger than the adsorbate-adsorbate interaction. As no covalent bonding is observed in PES measurement, the weak charge transfer indicated by the work function changes of about 0.15 ± 0.05 eV is probably the origin of adsorbate-substrate interaction. Such binding of C_{60} to SiC nanomesh lowers the C_{60} interlayer transport barrier (E_{inter}), favoring the transport of C_{60} molecules from top layers to the lower layers closer to SiC nanomesh, facilitating the epitaxial growth of a complete wetting layer C_{60} on the SiC nanomesh and leading to a layer-by-layer growth for the first two layers, as observed by *in-situ* STM investigations.

5.3 CuPc on the SiC nanomesh

5.3.1 STM study of CuPc on the SiC nanomesh

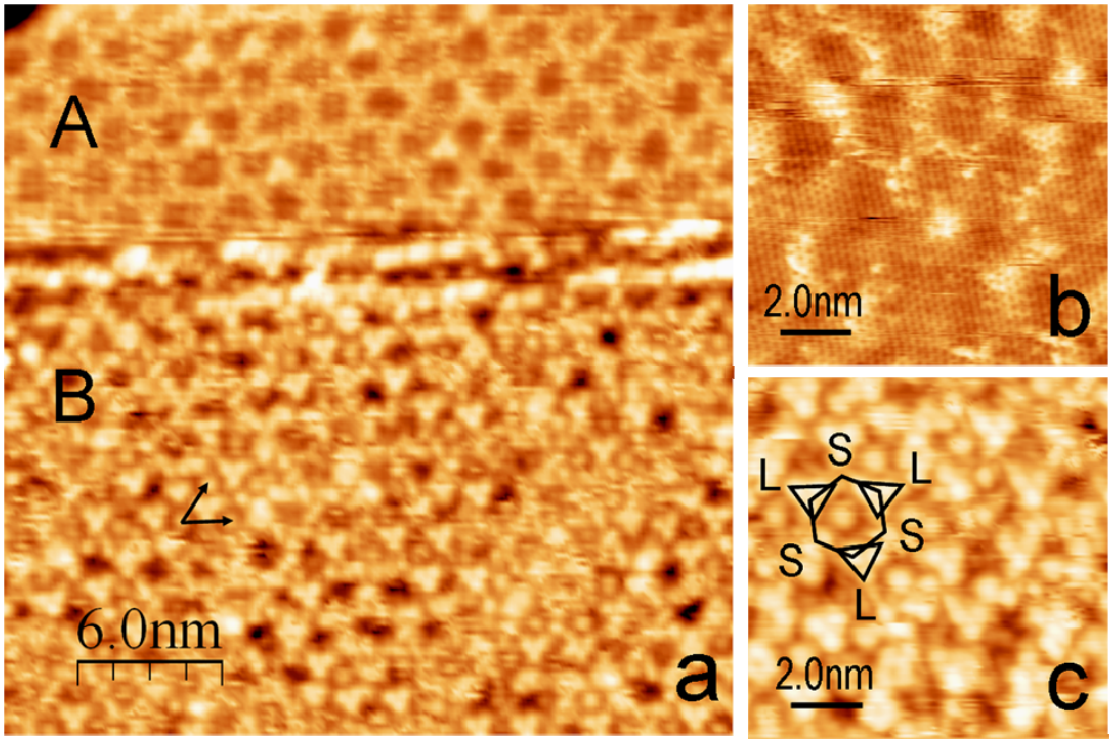

Figure 5.6. STM images of SiC nanomesh/graphene mixed phase surface. (a) Large area scan (30 × 30 nm^2, V_T = 2.1 V, I_T = 70 pA) (b) Enlarged image of terrace A (10 × 10 nm^2, V_T = 0.5 V, I_T = 70 pA), (c) Enlarged image of terrace B (10 × 10 nm^2, V_T = 2.1 V, I_T = 70 pA)

The SiC nanomesh surface prepared for CuPc deposition is slightly over annealed to transform a small portion of SiC nanomesh terrace into EG terrace. The existence of the EG terrace allows a direct comparison of the morphology differences for the same molecule deposited on the two different surfaces. The clean nanomesh surface is shown in figure 5.6. Terrace A is a typical EG terrace, as shown in the corresponding zoom-in figure 5.6b. Terrace B, which comprises 1.95nm honeycomb-like cells, is a SiC nanomesh terrace as shown in figure 5.6c. In this image, the cells of this honeycomb-like structure can be distinguished. These hexagonal cells are

alternatively surrounded by large vertices (trimeric protrusions) and small vertices (rims) shown in figure 5.6c. Herein, we denote the two structures as 'L' and 'S' respectively. Both features are used as references to identify the adsorption geometry of molecules.

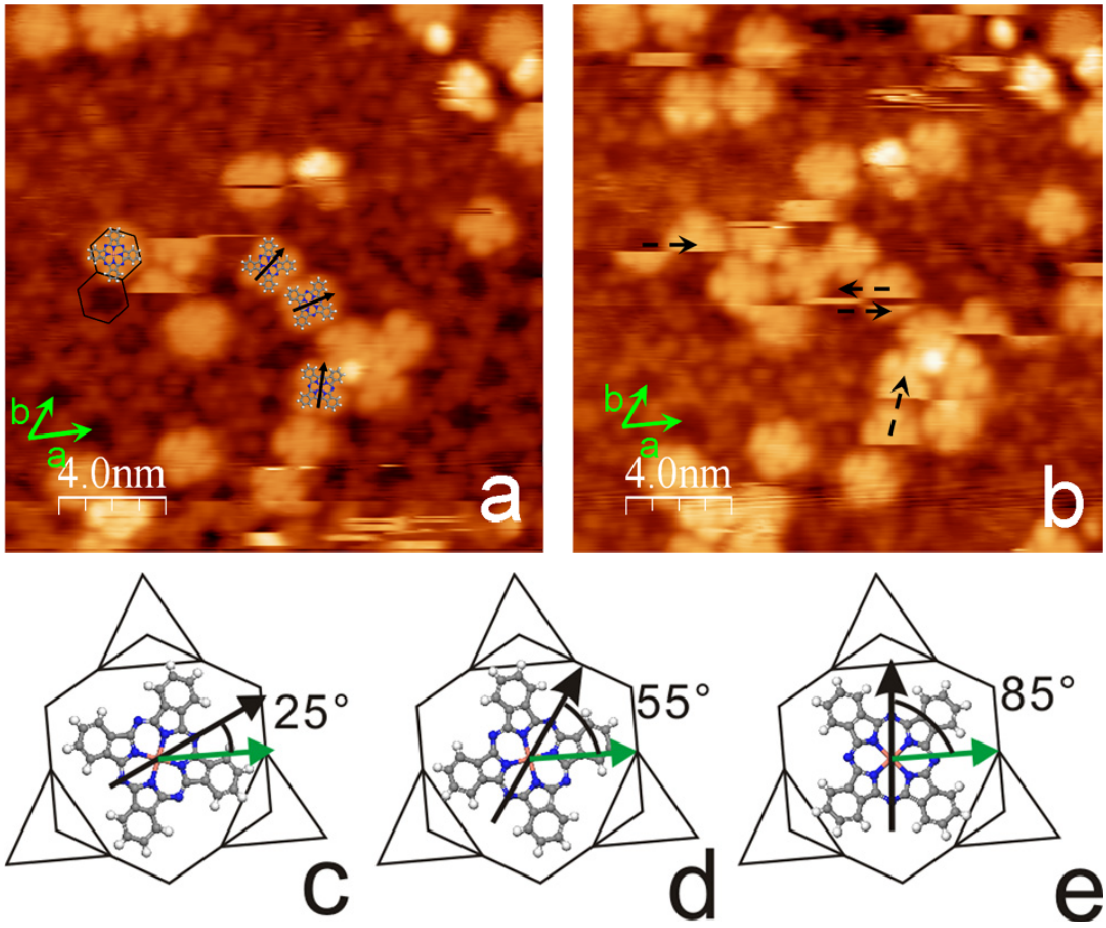

Figure 5.7. CuPc molecules on SiC nanomesh. (a) Adsorbed CuPc molecules. (b) hopping of single molecules under tip perturbation. (parameters for (a) and (b) 20 × 20 nm^2, V_T = 3.4 V, I_T = 40 pA) (c) to (e) schematic models of the three CuPc orientations on SiC nanomesh cells. Black arrows indicate the orientations of CuPc; green arrows indicate the a axis of SiC nanomesh.

After a nominal dosage about 0.1 monolayer (ML), single CuPc molecules which appear as four-leaved clovers as shown in figure 5.7. This dosage is estimated by the size of the CuPc molecules in its closed packed form on highly oriented pyrolytic graphite (HOPG).[146] The simultaneously resolved L vertices are used to as a

reference grid to determine the adsorption configurations of CuPc. In figure 5.7a, CuPc molecules lie directly above the nanomesh pores with their four lobes extended to the rims of the nanomesh cells. This is a clear indication that the growth of CuPc is directed by the SiC nanomesh. Furthermore, adsorbed CuPc molecules follow the orientation of the substrate. To clarify the orientations of CuPc, a vector pointing from the center copper atom outwards in-between of two lobes is used to indicate the in-plane orientation of CuPc (Black arrows in figure 5.7a). The reason for defining the vector as such is because the dark valley in-between two lobes can be clearly and accurately determined. Three orientations (25 ± 3º, 55 ± 3º and 85 ± 3º) relative to the substrate a axis are shown in figure 5.7a. The orientations of molecules are slightly varied from one image to another, and the errors are estimated by statistical average of molecules in several STM images. To elucidate these orientations, schematic pictures of CuPc with three different orientations as well as the SiC nanomesh cells (hexagon indicating the cell, triangles representing the L vertices) are shown in the panel c to e of figure 5.7. Taking the 3-fold symmetry of the substrate into account, the three orientations shown in figure 5.7c-e are identical. Only when multiple CuPc molecules absorb on this template do these three orientations become distinguishable in figure 5.7a and b. Due to the 4-fold symmetry CuPc, any orientation angle larger than 90º can be automatically reflected back to the first quadrant. As the result, the angles determined by 3-fold substrate symmetry (θ, θ + 120º and θ + 240º) are reduced to (θ, θ + 30º and θ + 60º). This deduction successfully explains the 30º angular difference of the three orientations.

As adsorbed CuPc molecules show three substrate-derived orientations, it is logical to deduce that these molecules are confined by the substrate as is the case on SiC 3 × 3.[23] However, this is incorrect. As shown in figure 5.7b, some CuPc molecules appear as complementary fragments at several locations, due to molecular hopping by either thermal activation or tip perturbation. The average hopping time (T_h) of CuPc on SiC nanomesh is experimentally estimated. About 17 fragmental images of CuPc molecule are distinguished over 34 molecules during the acquisition time (471 seconds). The hopping time is therefore estimated at around 1×10^3 seconds at low dosage. No rotation of the static CuPc molecules in sequential STM images is observed, but molecules may change their orientations during hopping. In a few cases, CuPc molecules may hop back to their original sites (back and forth dashed arrows in figure 2b), or new molecules may hop to previously occupied sites in sequential images. These molecules adopt the same orientation of the previous molecules at these sites, implying that in one cell, only one out of three symmetric in-plane orientations is favorable.

At 0.4 ML coverage, CuPc molecules are evenly distributed on the SiC nanomesh surface forming an ordered single-molecular array, as shown in figure 5.8a. This array possesses a 1.95 nm periodicity and 3-fold symmetry of the substrate. The periodicity of the CuPc array is not only larger than the CuPc size in its closed packed form (about 1.4 nm),[146, 178] but also larger than the calculated maximum size of the CuPc molecule (1.68 nm in diagonal length).[179] The large distance (2.7Å or larger) and arbitrary orientations of adjacent molecules suggests a negligible interaction

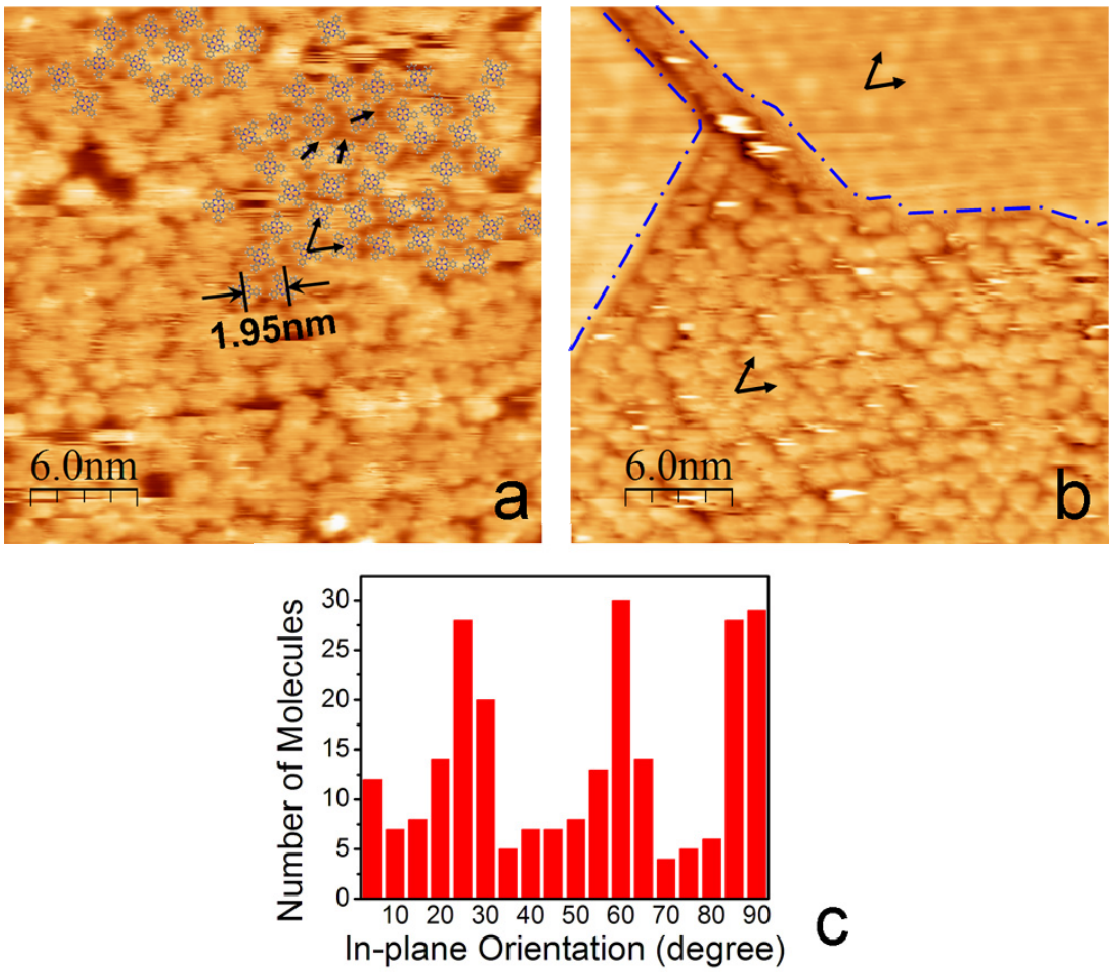

Figure 5.8. The CuPc single-molecular array on the SiC nanomesh surface. (a) 30 × 30nm^2 STM image of the CuPc molecular array (V_T = -1.9 V, I_T = 40 pA). (b) 30 × 30 nm^2 STM image of the CuPc molecular array on a nanomesh terrace (V_T = -2.2 V, I_T = 40 pA). (c) Statistics of the in-plane orientations of CuPc molecules.

between them. As most molecular orientations can be distinguished in figure 5.8a, a statistical analysis is performed to study the distribution of these orientations, as shown in figure 5.8c. Three peaks at 25º, 60º and 90º are observed, indicating the preferred in-plane orientations of CuPc molecules. These angles are similar to the orientation of CuPc molecules at low coverage. Thus, both spatial locations and orientations of CuPc are confined by the substrate to form an ordered single molecular array.

In figure 5.8b, the CuPc array is observed to cover the lower terrace uniformly, while the upper two terraces covered by single-layer graphene (SLG) are empty, suggesting the preferential adsorption of CuPc on SiC nanomesh instead of on graphene. The formation of this molecular array is not limited to selected nanomesh terraces; on the contrary, this array is observed on all SiC nanomesh terraces forming a wafer scale single molecular array. The molecular density of this array is estimated to be about 3.0×10^{13} molecules/cm^2.

At high coverage, the hopping of CuPc happens less frequently than at low dosage. About 12 hopping events (fragmental images of CuPc molecule) are found in the CuPc array with more than 200 molecules in figure 5.8a. Thus, T_h at 0.4ML coverage is about one order of magnitude larger than T_h at 0.1ML coverage. This observation suggests that the hopping possibility of molecules depends largely on the coverage.

In general, when weak Van-der-Waals forces predominate on surfaces, *e.g.* on HOPG or on MoS_2,[146, 178] CuPc molecules prefer to arrange into 4-fold symmetric close-packed islands due to stronger intermolecular interaction. However, on reactive surfaces such as Si(111)[180] or SiC 3×3 reconstruction,[23] CuPc molecules are covalently bound by the dangling bonds of the substrates with one or several possible adsorption configurations. Although CuPc molecules thus follow the symmetry of substrate, it hardly forms a highly periodic array due to low diffusivity of deposited molecules. Herein, the adsorbed CuPc molecules adopt the symmetry of SiC nanomesh instead of its internal symmetry indicating that this site-selective attraction

force between CuPc and SiC nanomesh dominates the intermolecular interaction. However, dangling bonds have never been observed in experiments or proposed in theoretical calculations[28, 58] which implies that this interaction is unlikely to be covalent bonding. Thus, synchrotron-based photoemission experiments were needed to clarify the origin of this interaction.

5.3.2 PES study of CuPc on the SiC nanomesh

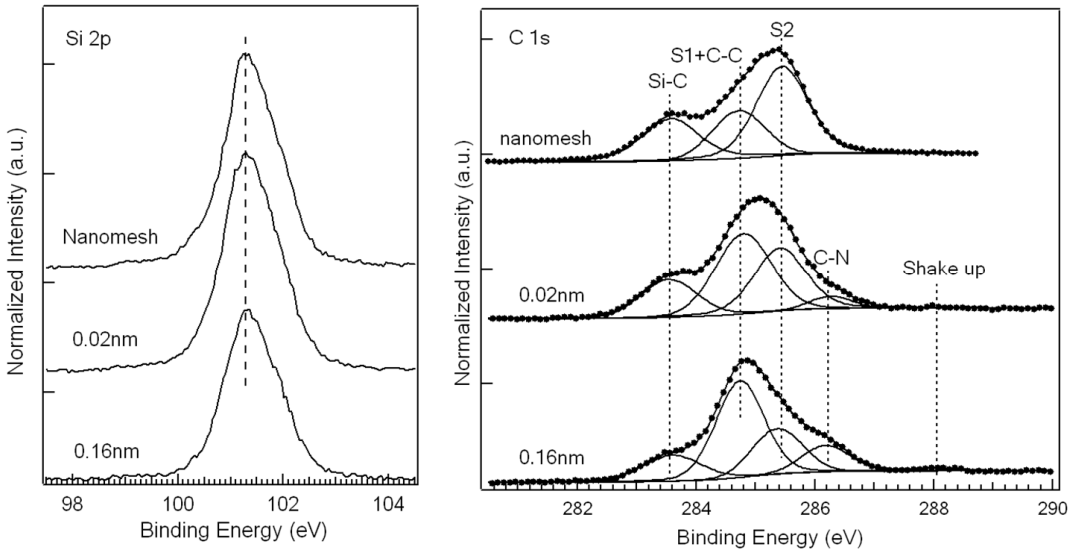

Figure 5.9. Core level photoemission spectra of Si *2p* and C *1s* of CuPc on SiC nanomesh.

The core level spectra of the Si *2p* and C *1s* peaks before and after submonolayer CuPc deposition are shown in figure 5.9. Before and after CuPc growth, there is no discernible shift in Si *2p* peak, suggesting no chemical interaction between molecules and substrate. The C *1s* peak for clean SiC nanomesh has three components as discussed before.[28, 51] After deposition of CuPc, the position of three substrate-related peaks show no discernable shift except that two additional components appear

in the C *1s* spectrum. The peak positions at 286.2 ± 0.05 eV and 288.1 ± 0.05 eV are attributed to carbon in C-N bond and its shake-up transition respectively. The increase of G peak is attributed to the superimposed C-C peak originated from CuPc. The C *1s* binding energy of CuPc molecules are consistent with previous reports.[181, 182]

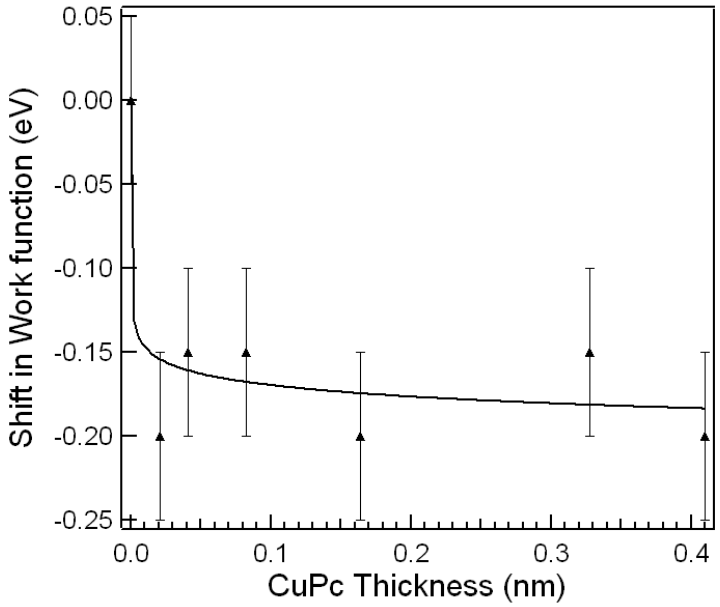

Figure 5.10. Work function change due to absorption of CuPc.

Thus, there is no indication of surface chemical reaction. However, a small work function reduction of 0.15 ± 0.05 eV is observed after CuPc deposition (figure 5.10), suggesting a vacuum level shift relative to Fermi level due to the formation of interface dipole. The origin of this dipole could be either due to the electron transfer from adsorbate to the SiC nanomesh or electron density redistribution along the z direction to form an induced dipole in the adsorbates.[170] As a result, the formation of such a weak interface dipole should be responsible for the selective confinement of CuPc molecules on SiC nanomesh.

In conclusion, an ordered single molecular array of CuPc is observed on SiC nanomesh. The array has the dictated periodicity and symmetry of the substrate. Furthermore, the CuPc molecules in the array have three in-plane orientations regulated by the substrate. Since the intermolecular separation of adjacent molecules (1.95 nm) is larger than the Van-der-Waals envelop of CuPc (1.68 nm), the strength of intermolecular interaction is negligible. Photoemission experiments reveal a weak interface dipole between the adsorbates and substrate which could be responsible for the selective adsorption of CuPc. Meanwhile, the size of CuPc could be important for the formation of molecular array, as the Van-der-Waals envelop of CuPc (1.68 nm) is slightly smaller than the size of SiC nanomesh cells (1.95 nm) which allows a one-molecule-in-one-cell configuration, beyond which, it is too large to accommodate more than one molecule.

5.4 Pentacene on the SiC nanomesh

5.4.1 STM study of pentacene on the SiC nanomesh

The two molecules studied in the previous sections exhibit totally different behaviors. C_{60} forms hexagonally closely packed layers whereas CuPc forms single molecular arrays. From these studies, we hypothesize that the SiC nanomesh surface only exhibits the template effect for planar molecules. Thus, another planar molecule, pentacene, is tested in this section. This molecule consists of five fused benzene rings and exhibits a two-fold symmetry in its geometry. Figure 5.11a shows the STM

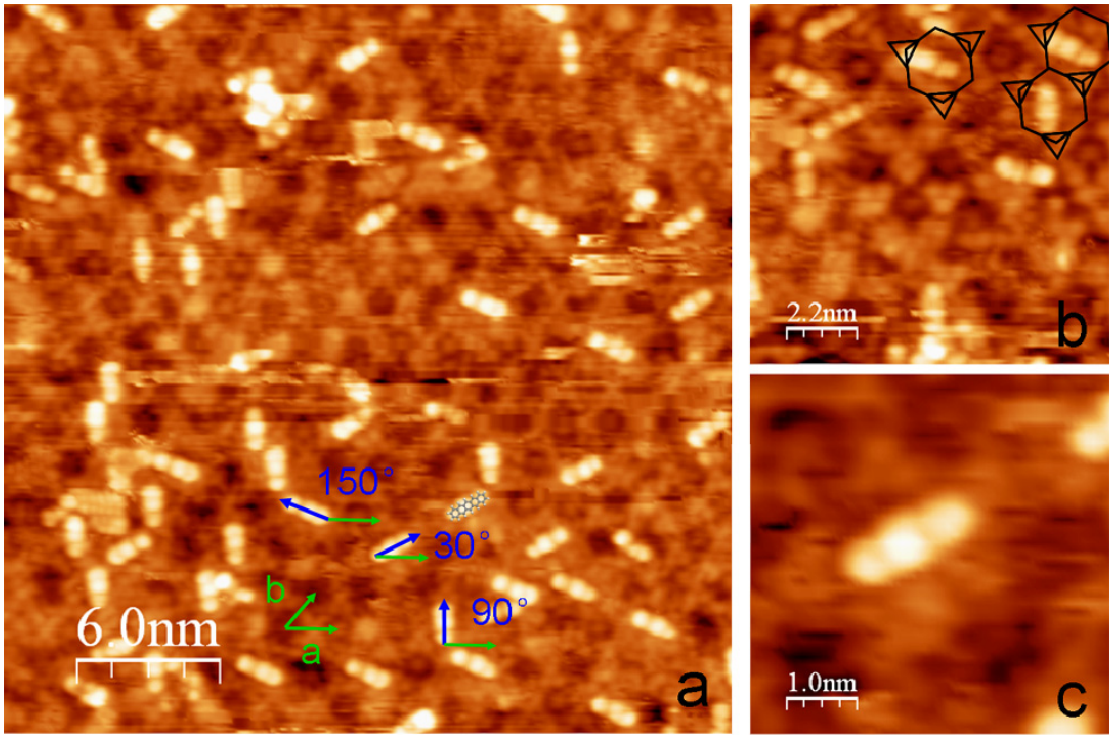

Figure 5.11. Pentacene molecules on SiC nanomesh. (a) 30 × 30nm^2 STM image of pentacene on SiC nanomesh (V_T = 1.7 V, I_T = 40 pA). Blue arrows indicates the orientation of pentacene molecules and green arrows indicates the a axis of the substrate. (b) The enlarged image shows the location of pentacene on the SiC nanomesh. The hexagons indicate the SiC nanomesh cells and the triangles indicate the L vertices. (c) The enlarged image of a single pentacene molecule.

image of pentacene deposited on SiC nanomesh at low coverage (~0.2 ML). The rod-like feature represents a single pentacene molecule lying flat. Due to the different molecule-substrate coupling, the submolecular feature of pentacene varies from one substrate to another.[160, 161, 183, 184] Herein, the submolecular feature of pentacene appears as three bright protrusions in figure 5.11c.

As with the CuPc molecules, pentacene adsorbs within the cells and points to the corners of these cells. The magnified image (figure 5.11b) shows that the pentacene molecules deviate slightly from the center of the cells with one phenyl end closer to the L vertex. The orientations of adsorbed pentacene molecules are coincident with

the direction from the cell center to L vertex and about 30º, 90º and 150º degrees to the substrate *a* axis. In figure 5.11, the hopping of pentacene is rare (less than 1 hopping event over 100 molecules in one scan), indicating the trapping of pentacene on SiC nanomesh is much stronger than in the case of CuPc. The hopping time estimated for pentacene is about 4×10^4 seconds using the same way for CuPc.

From the STM studies, both molecules are trapped in the cell with substrate-determined orientations. These observations imply that these molecules are trapped not only by the cell centers but also by the vertices of the cells. In the case of pentacene, the L vertex appears to interact more strongly with pentacene than the S vertex. In the case of CuPc, the molecular lobes are lying in-between the L and S vertices; possibly due to the competing interactions between the molecule with the L and S vertices. Although the atomic structure of these nanomesh features are not fully understood, these cells and vertices effectively trap CuPc and pentacene molecules to form molecular arrays.

When the dosage of pentacene increases to 0.8 ML, molecules reside on the SiC nanomesh with less order. However, three types of adsorption configurations can be distinguished on this surface. First of all, small numbers of molecules maintain the 3-fold symmetric configuration which has been shown at 0.1 ML dosage (black arrows in figure 5.12a). The second configuration is where the molecules pack in parallel (figure 5.12c). In this configuration, intermolecular distance is about 0.85nm, much less than the periodicity of SiC nanomesh (1.95nm), implying that two molecules reside in one SiC nanomesh cell (figure 5.12d). The last distinguishable configuration

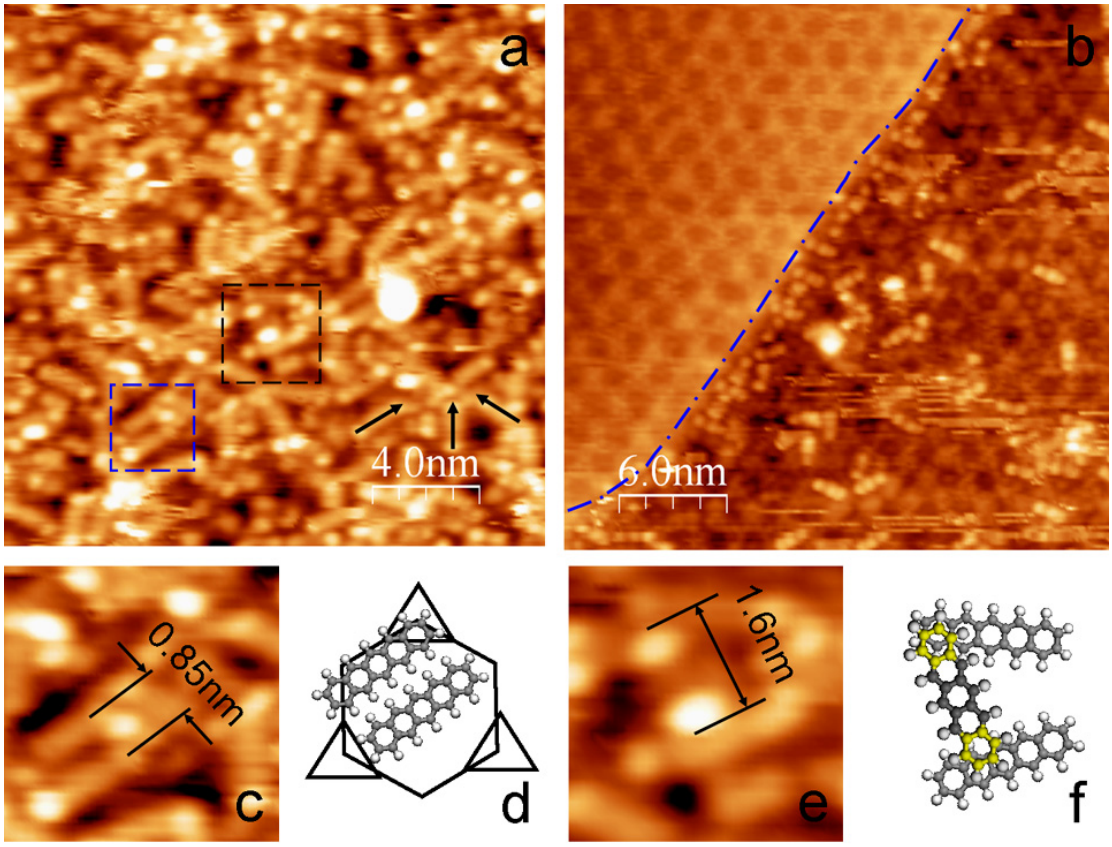

Figure 5.12. Quasi-amorphous pentacene layer on SiC nanomesh. (a) 0.8 ML pentacene on SiC nanomesh (20 × 20 nm^2, V_T = -1.9 V, I_T= 40 pA) (b) Pentacene at the domain boundary (30 × 30 nm^2, V_T = 1.9 V I_T = 40 pA). (c) Enlarged image shows the parallel configuration from the blue square in (a). (d) Schematic of parallel configuration in honeycomb cell. This two-in-one configuration is geometrically possible. (e) Enlarged image shows the bridge configuration from the black square in (a). (f) Schematic of bridge configuration. The two ends of upper pentacene are colored in yellow to indicate the bright dots in (e).

is the bridge configuration, whereby the molecules appear as two bright dots separated by a gap (figure 5.12e). Although the pentacene in the second layer shows similar appearance on Ag(111), the contrast of pentacene in figure 5.12e is much stronger than the pentacene on Ag(111).[185] Therefore, the appearance could be regarded as one molecule bridging above two underlying molecules (figure 5.12f). The two ends are contacted by the underlying molecules and have short path for tunneling current. On the contrary, the middle area is suspended above a void and

requires an additional intramolecular path for tunneling current. As a result, the bridged molecules give a dark middle area with two bright ends. The similar pentacene bridge configuration above two silicon dimers has been observed by Kasaya *et al.*[186] The mixture of these configurations at high coverage could be explained by two reasons. The first is the small size of pentacene (1.66 × 0.74 nm)[187] relative to the nanomesh cell. The space between two pentacene molecules in neighboring cells is large enough to accommodate additional molecules in metastable configurations, *i.e.*, the parallel and bridge configurations. Therefore, the small size of pentacene allows disorder in the molecular array at higher coverage. The second reason is attributed to the limited diffusivity of pentacene molecules on the SiC nanomesh. In figure 5.12b, a domain boundary between graphene and SiC nanomesh is indicated by the dashed line. It can be clearly observed that no pentacene molecules adsorb on graphene, and that the population of pentacene increases on the SiC nanomesh close to this boundary. The increase in population is due to the unidirectional diffusion of pentacene from graphene to the nanomesh surface. The same diffusion trend was suggested in CuPc deposition, but the diffusivity of CuPc on SiC nanomesh is large enough to distribute the excess molecules away from the boundary (*cf.* figure 5.8b) and form periodic molecular arrays. Pentacene therefore forms a random array at high coverage due to multiple adsorption configurations and low diffusivity.

5.4.2 PES study of pentacene on the SiC nanomesh

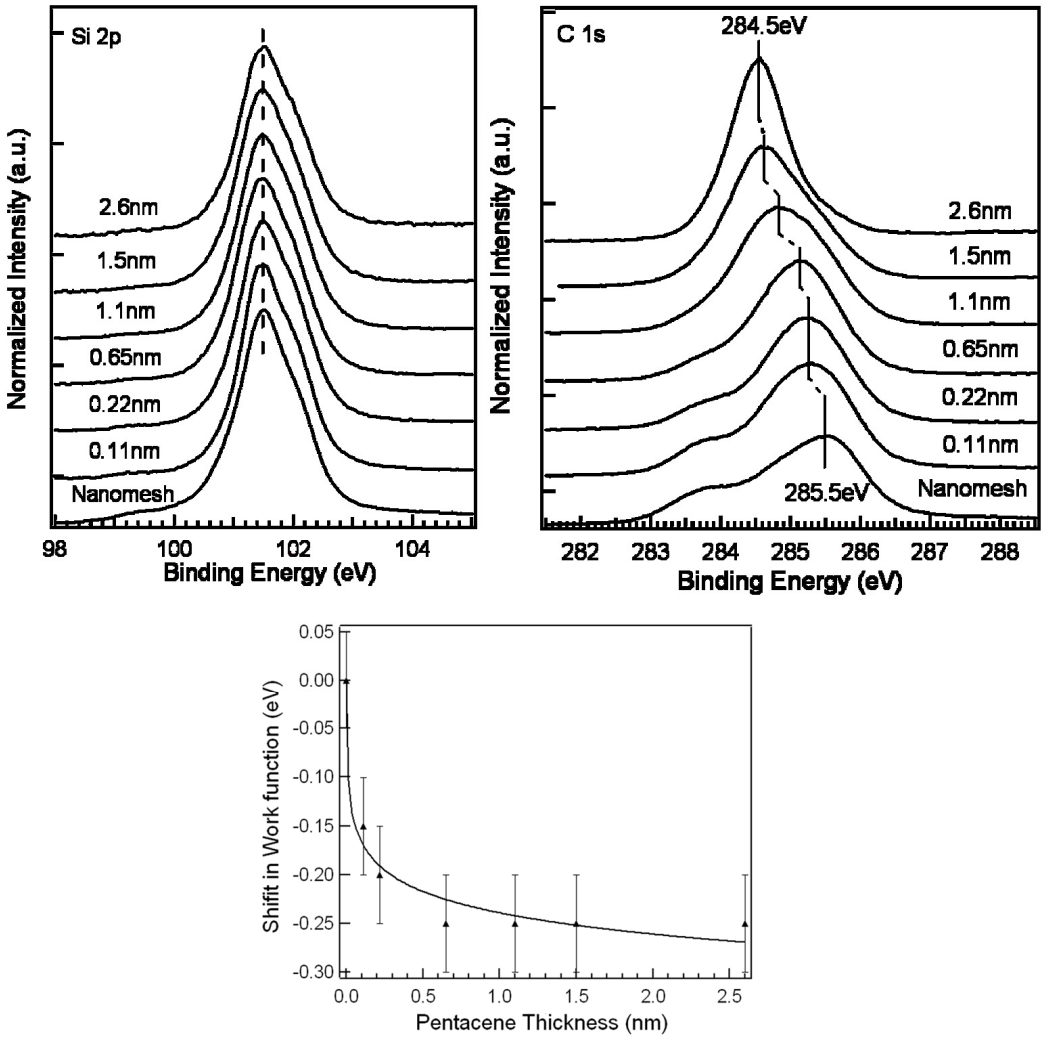

Figure 5.13. PES spectra of Si *2p* in a , and C *1s* in b from pentacene/nanomesh; c. shift of work function as a function of pentacene thickness.

Absorbed pentacene molecules exhibit longer hopping time than CuPc molecules. This phenomenon suggests that the substrate attraction to pentacene is stronger than the attraction to CuPc. To compare these attractions to two molecules, photoemission spectra of pentacene on SiC nanomesh are measured (figure 5.13). A work function reduction (0.25 ± 0.05 eV) is observed after pentacene deposition. This reduction is larger than the other two molecules. From figure 5.13, no discernible energy shift is

observed in the core level spectrum of Si *2p* implying no covalent bonding between adsorbates and substrate. The main peak in C *1s* spectrum (figure 5.13) is shifted from 285.5 ± 0.05 eV for SiC nanomesh to 284.5 ± 0.05 eV for pentacene at 2.6nm. This shift is explained by the increased intensity of pentacene C-C peak at 284.5 ± 0.05 eV.[188, 189] Thus, the interaction between pentacene and SiC nanomesh surface is also attributed to charge transfer at the interface.

In conclusion, pentacene molecules are confined by the SiC nanomesh and mainly adopt the L vertex to pore configuration. However, pentacene forms a random array at 0.8 ML due to the mixture of three types of pentacene absorption configurations. These configurations are the consequence of the much small size of pentacene in comparison with the unit cell of the SiC nanomesh. From photoemission experiments, a stronger interface dipole (0.25 ± 0.05 eV) than that in the case of CuPc or C_{60} is observed. This interface dipole appears as a large diffusion barrier which reduces the diffusivity of pentacene and hinders the ordering of this molecular array.

5.5 Summary

In summary, we investigated the template effect of the SiC nanomesh surface for three organic molecules. The template induced growth was successfully observed in CuPc and pentacene deposition, whereas C_{60} could only lead to the hexagonal close packed wetting layers. While CuPc formed an ordered single molecular array with topographic properties governed by the substrate due to its compatible size relative to the nanomesh superstructure, pentacene with its 2-fold rod-like shape formed a

dispersive array with 3-fold symmetric in-plane orientations. At higher coverage, two additional adsorption configurations were identified and resulting in a quasi-amorphous pentacene overlayer.

Photoemission results indicate that the molecule-substrate interaction for all three cases originated from charge transfer at the interface. The magnitudes of the interface dipoles for three molecules are small (-0.15 ± 0.05 eV, 0.15 ± 0.05 eV and 0.25 ± 0.05 eV for C_{60}, CuPc and pentacene respectively (negative value for upward shift)); C_{60} received electrons from the substrate while the other two molecules donated electrons. Therefore, the small dipole interactions allow other factors such as geometry of molecules affecting the assembled structures. C_{60} that is smaller than the nanomesh cells and spherical shape is unable to be selectively trapped by the SiC nanomesh, resulting in a molecular wetting layer due to the charge transfer at the interface. Pentacene with a planar shape is successfully trapped by the template but with several substrate-determined configurations. CuPc with a planar shape and compatible lateral size (1.68 nm in diagonal) achieved the most ordered single molecular array. As a result, without strong substrate-molecule interaction and intermolecular interaction such as covalent bonding or hydrogen bonding, the size and the shape of the target molecules can play a decisive role to the configurations of adsorbed molecules on the SiC nanomesh.

The achieved CuPc single molecular array is distinctly different from molecular arrays in supramolecular porous networks. The molecules in the present array are well isolated from each other, and only interacting with the substrate. This isolated single

molecule CuPc array with extremely high density has potential applications in data storage and chemical sensors.

The template effect of SiC nanomesh also provides some clues about its atomic structures. Both molecules (CuPc and Pentacene) are found preferentially adsorbed at the center of nanomesh cells indicating the stronger molecular-substrate interaction there. As both molecules are planar with conjugated π orbitals, the cell center probably also contains delocalized π orbitals thereby generating π-π interactions. Thus, the graphene-like sublayer of the SiC nanomesh may show sp^2 hybridized carbon bonds at the nanomesh centers while the nanomesh edges may contain more sp^3 hybridized carbon bonds. However, the details of the atomic structures of this sublayer need further investigations. Meanwhile, the CuPc single-molecule arrays may contain interesting magnetic properties which need further investigations by means of magnetic force microscopy (MFM) or spin polarized scanning tunneling microscopy (SP-STM).

CHAPTER 6 INTERCALATION AND CHEMICAL REACTIONS OF EPITAXIAL GRAPHENE ON 6*H*-SiC(0001)

6.1 Introduction

In the previous chapters, the structure, oxidation and template effect of the SiC nanomesh were discussed. However, the SiC nanomesh could also serve as a buffer layer below the EG. In principle, this buffered SiC nanomesh layer is believed to be identical to the uncovered SiC nanomesh layer, although the EG layer serves as a protecting layer to prevent oxidation of the underlying SiC nanomesh layer (*c.f.* chapter 4). If this covered SiC nanomesh can be modified by intercalation of adsorbates without creating significant changes to the EG layer on top, it could provide a possible *in-situ* route to alter the properties of the EG layer, *e.g.* opening a band gap in EG. Thus, the possible chemical reactions of adsorbates with the covered SiC nanomesh need to be investigated.

Due to the small lattice constant of graphene (2.45Å), atomic penetration of the graphene network along the out-of-plane direction is energetically unfavorable. DFT calculations suggest the energy barrier for the helium atom could be as large as 10eV, prohibiting penetration along this direction.[190] Nevertheless, the graphene layer is not covalently bonded with the substrate, and the typical interlayer distance between graphene and substrates is usually quite large (about 3.35Å for graphene-graphene

distance[48]), implying that diffusion of atoms at the interface could be quite easy. Intercalation of metal atoms such as Cu, Ag and Au has been achieved for epitaxial graphene (EG) on Ni(111)[191, 192]. Dedkev *et al.*[89] has shown that the iron adlayer on epitaxial graphene/Ni(111) can be intercalated below the EG layer after 200°C annealing. The inserted Fe forms a thin interlayer and is protected by the graphene top layer from oxidation under ambient conditions. Intercalation of molecules such as C_{60} is also reported at the EG/Ni(111) interface[86].

Most intercalation studies have focused on EG on metal, and only a few studies have been done on EG on SiC(0001),[52, 53] although graphene on SiC has promising practical applications.[193, 194] With a unique interfacial nanomesh layer, the intercalation of graphene on SiC should behave quite differently from graphene on metals. For instance, the nanomesh layer is an active layer, which can react with O_2 at 600°C and form graphene and silicon oxides. This observation implies the nanomesh layer could be involved in the reactions with intercalated molecules/atoms. In this chapter, the intercalation of EG on SiC(0001) by oxygen molecules and iron atoms is studied by synchrotron-based XPS and STM. The purpose of this study is two-fold. The first is to investigate the intercalation of adatoms on graphene on SiC(0001); the second is to probe possible reactions at the interface.

6.2 Oxidation of epitaxial graphene on SiC(0001)

As mentioned in chapter 4, the EG layer can be transformed from the SiC nanomesh layer with O_2 (4×10^{-4} torr) exposure at 600°C. In this section, instead of nanomesh layer, the EG layer is exposed to O_2 at different temperatures using different oxygen dosages. As the graphene layer generated on SiC nanomesh can inhibit further oxidization at temperatures lower than 1000°C, higher oxygen pressures and temperatures are applied to oxidize the graphene sample.

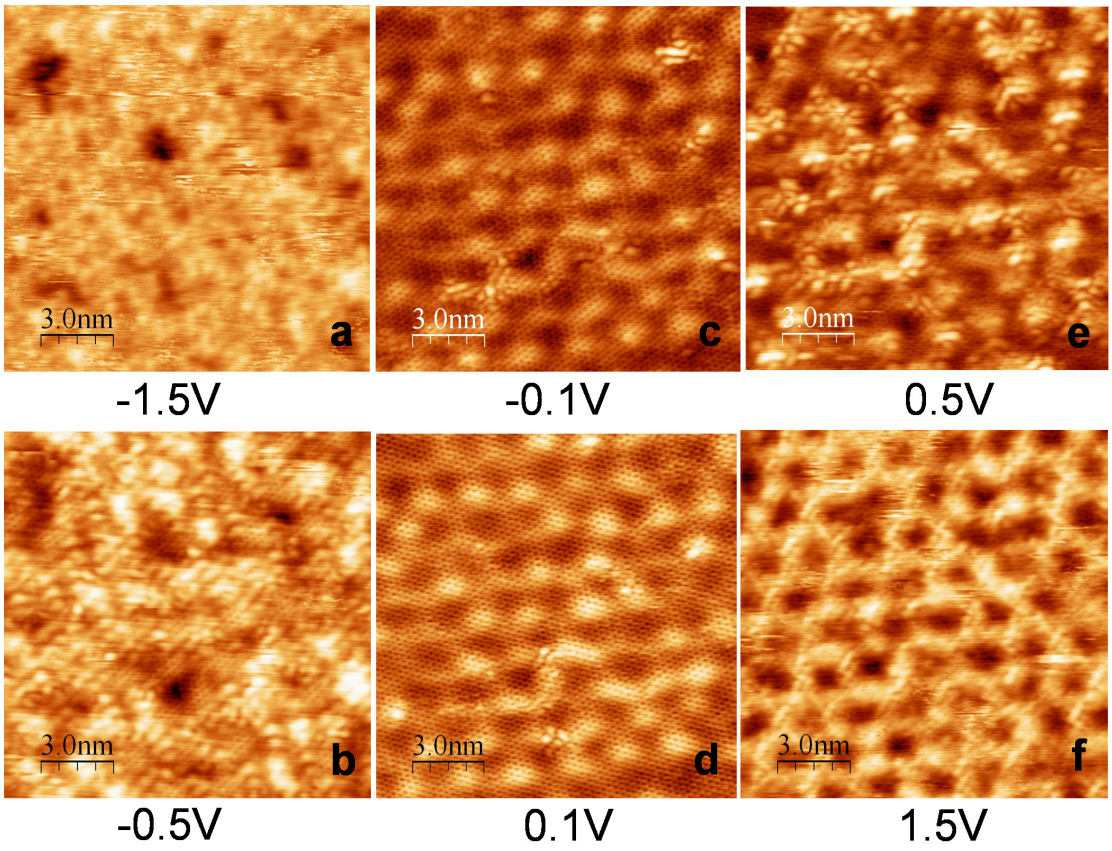

Figure 6.1. $15 \times 15nm^2$ images of epitaxial graphene at different tip biases (I_T = 70pA). The graphene atomic lattice is apparent at low scanning bias (± 0.1eV), partially observable at ± 0.5eV, but not distinguishable at ± 1.5eV.

Clean epitaxial graphene on SiC nanomesh is shown in figure 6.1 as reference. The graphene network exhibits a "6 × 6" modulation originated from the SiC nanomesh layer. Both the graphene network and the superimposed modulation are bias-dependent. The graphene network is apparent only at low bias (± 0.1eV). When the bias increases, the graphene network becomes transparent.[195] The "6 × 6" modulation is apparent in filled state images (positive bias); the contrast of this modulation is suppressed in empty state images (negative bias). The bias-dependence of the SiC nanomesh was previously observed, but its origin is still unclear.[26] If the reaction of oxygen on this surface happens under the graphene network, direct observation of structural changes is usually prohibited. Therefore, the "transparency" of graphene network under high bias provides an alternative way to monitor sub-EG adlayer changes.

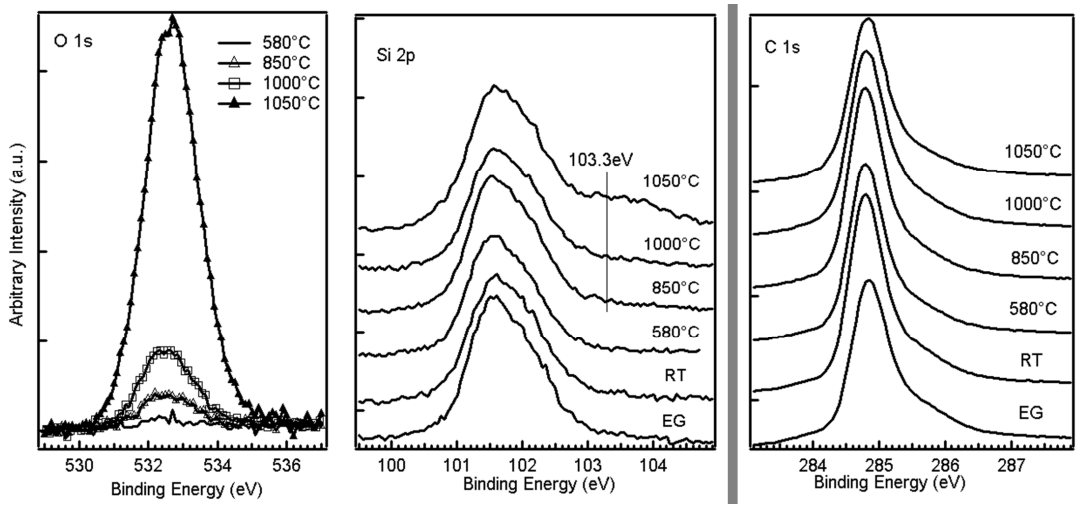

Figure 6.2. XPS spectra of O *1s*(left), Si *2p*(middle) and C *1s*(right) for oxidized EG at different temperatures and oxygen dosages. The colors of spectra in three figures are kept same for same condition.

The photoemission spectra of EG at different temperatures and O_2 dosages are shown in figure 6.2. The O *1s* peak, which is the major indicator of sample oxidation, appears at 850°C with a dosage about 2.2×10^5L, but this peak becomes prominent only at 1050°C with 3.8×10^6L dosage. Correspondingly, a small component at 103.3 eV in the Si *2p* spectra is observed at this temperature. This component is attributed to Si atoms in its 4+ state.[21] No prominent change in the C *1s* spectra is observed, indicating that carbon atoms do not react with oxygen. Therefore, we attribute the appearance of oxygen peak and new silicon component to the formation of silicon dioxide. The EG layer on top probably serves as a barrier to the penetration of oxygen molecules, and hinders the oxidation process except at higher temperatures.

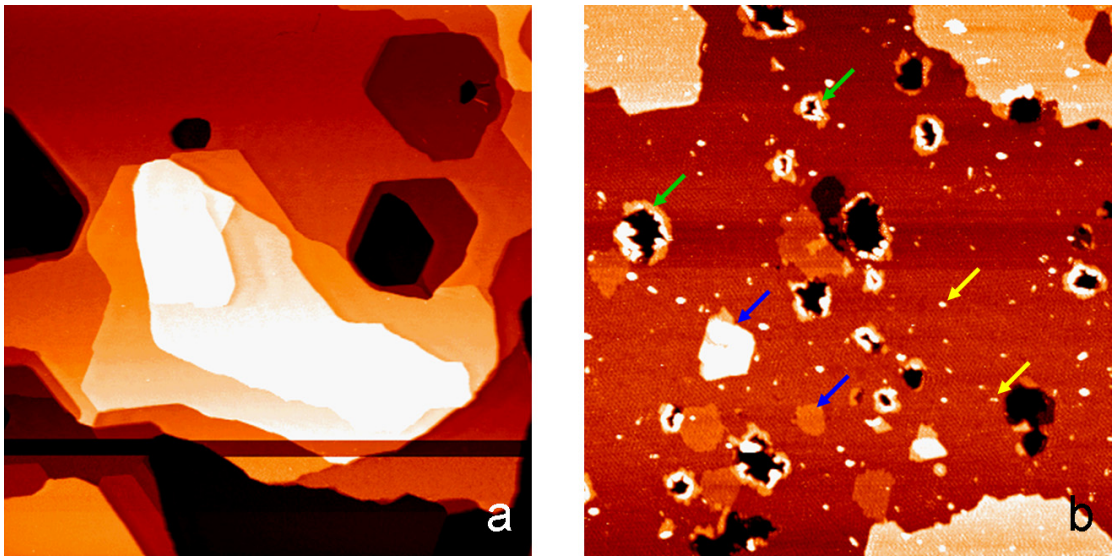

Figure 6.3. STM images of EG before and after oxidation, a) Before oxidation(2.0V, 170pA, $500 \times 500 nm^2$); b) After oxidation at 1050ºC (2.0V, 100pA, $200 \times 200 nm^2$).

To better understand the oxidation process, the images of the sample before and after the oxidation are recorded by STM. Figure 6.3 shows the large scale STM images of pristine and oxidized EG (1050°C, oxygen partial pressure at 1×10^{-3}torr).

It can be clearly observed that oxidation of EG creates several nanostructures, including flakes (blue arrows), clusters (yellow arrows) and pits (green arrows). Flakes are small pieces of graphene layer (~10nm in diameter) on nanomesh terraces. Their heights are variable: the smallest height observed is about 0.07nm, close to the step of monolayer graphene to bilayer graphene;[42] the largest height exceeds 0.4nm, larger than the height of silicon carbide bilayer (0.25nm) and should have different origin from the graphene layers or SiC bilayers. Clusters are small bumps on the surface. Their typical size is less than 5nm, with a height ranging from 0.3nm to 0.6nm. These two structures were also observed in the oxidation of SiC nanomesh at 1050°C. (*c.f.* section 4.2.2) Their formation on SiC nanomesh is related to the underlying silicon oxide clusters. Herein, XPS spectra suggest that the formation of similar structures on EG surface could be linked to the intercalated silicon dioxide.

The last generated nanostructures, pits, are not observed in the nanomesh oxidation. These pits have irregular shapes decorated by bumps and flakes. These pits are probably the consequence of the etching of EG layer. Similar pits due to etching of exfoliated graphene by oxidation at 450°C with oxygen partial pressure at 260 torr have been also observed.[196] The isotropic etching of exfoliated graphene gives rise to round holes about one graphene layer deep. Herein, higher temperatures are needed to initiate the etching due to the lower oxygen partial pressure used (10^{-3} torr). The complicated structure of the etch pits indicate that multiple interactions are involved in pit formation. Silicon oxidation probably results in the bumps and flakes around the pits. The size of pits varies from less than 5nm to more than 20nm and the depth of

pits increases with increasing pit size. As most pits are deeper than the terrace they sit on, the SiC substrate may also be etched. These three structures on the surface are discussed in detail in the following paragraphs.

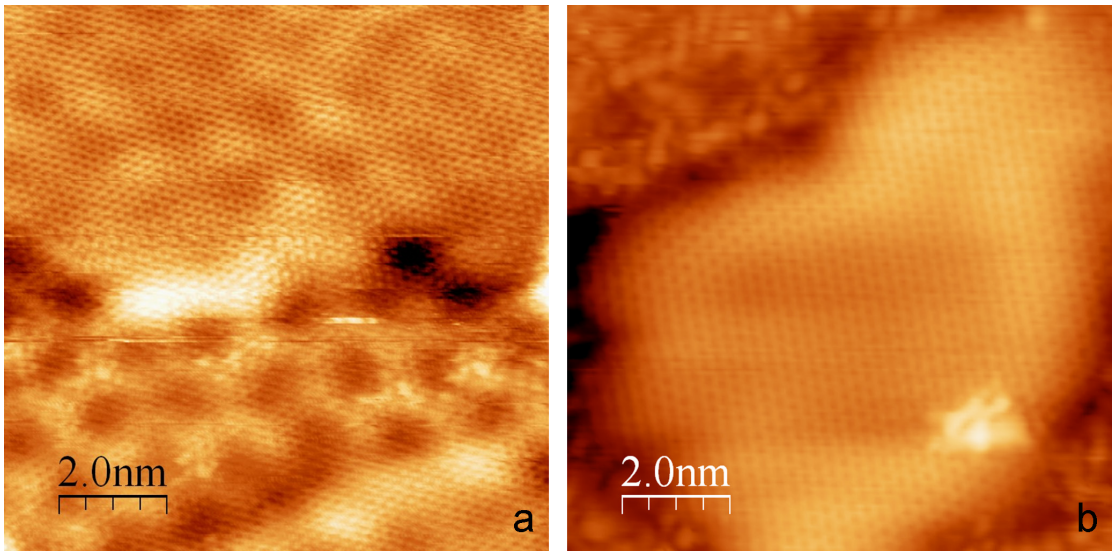

Figure 6.4. Two types of flakes on oxidized EG sample, a) The flake with the "6 × 6" modulation, upper part of image (0.3V, 30pA, 10 × 10nm^2); b) the flake without the "6 × 6" modulation (1.5V, 70pA, 10 × 10nm^2).

The flakes on oxidized EG are shown in figure 6.4. The flake in upper part of panel a has the smallest height (0.07nm), whereas the flake in panel b has a height about 0.18nm. Both flakes are covered by a continuous layer of graphene crossing the boundary of flakes. However, the flake in panel a shows the underlying "6 × 6" nanomesh modulation, while in panel b, the modulation is absent. Thus, the flake in panel a can be understood as bilayer graphene sitting on the substrate with one missing silicon carbide bilayer relative to the adjacent monolayer graphene.[42] The large height of the flake in panel b suggests an intercalated layer below it. Due to the high bias used in figure 6.4b (1.5V), the graphene network around the flakes become

invisible. However, the graphene network above the flake is unusually visible at this bias. Thus, this intercalated layer is capable of decoupling the nanomesh-graphene interaction enabling the EG layer to be visible at high bias. This intercalated layer is probably the silicon dioxide layer suggested from the XPS observations.

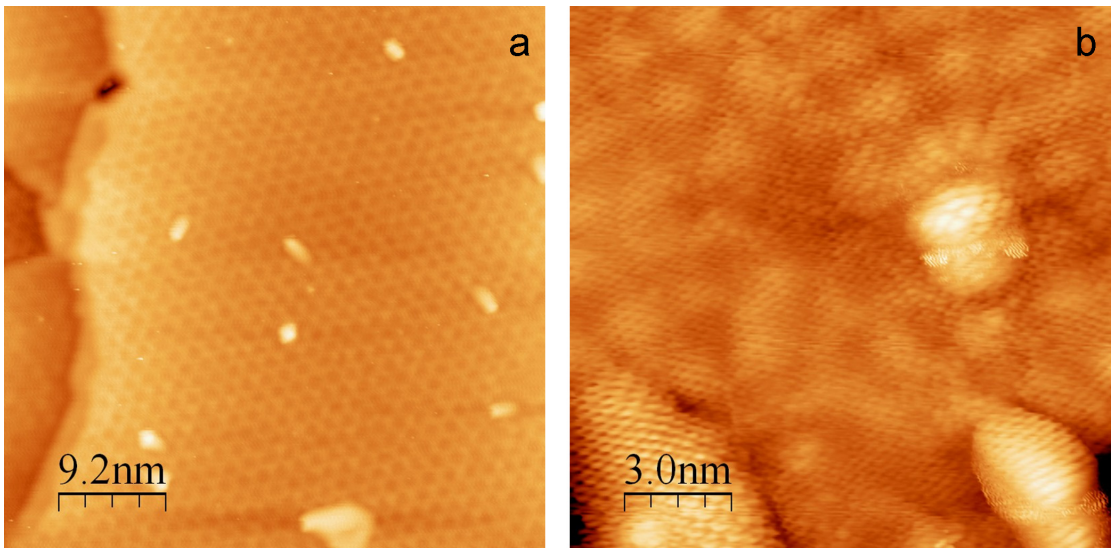

Figure 6.5. Clusters on oxidized EG sample. a) Large scale image of clusters on the surface (2.1V, 140pA, 46× 46nm^2); b) Zoomed in image of clusters on the surface (0.1V, 70pA, 15× 15nm^2).

Oxidized EG contains many clusters (figure 6.3). The density of clusters is about 3×10^{11} nm^{-2}, about one order of magnitude higher than flakes and pits. These clusters appear as bumps or asymmetrically elongated bumps on the surface with diameters of about 2nm in figure 6.5a. In the high resolution image (figure 6.5b), graphene networks are clearly resolved above the clusters, suggesting that they are covered by graphene rather than clusters above graphene. Similar to the observation of flakes, the graphene network above the clusters can be observed at high bias and do not possess the "6 × 6" modulation, suggesting the existence of intercalated silicon dioxide below the graphene clusters.

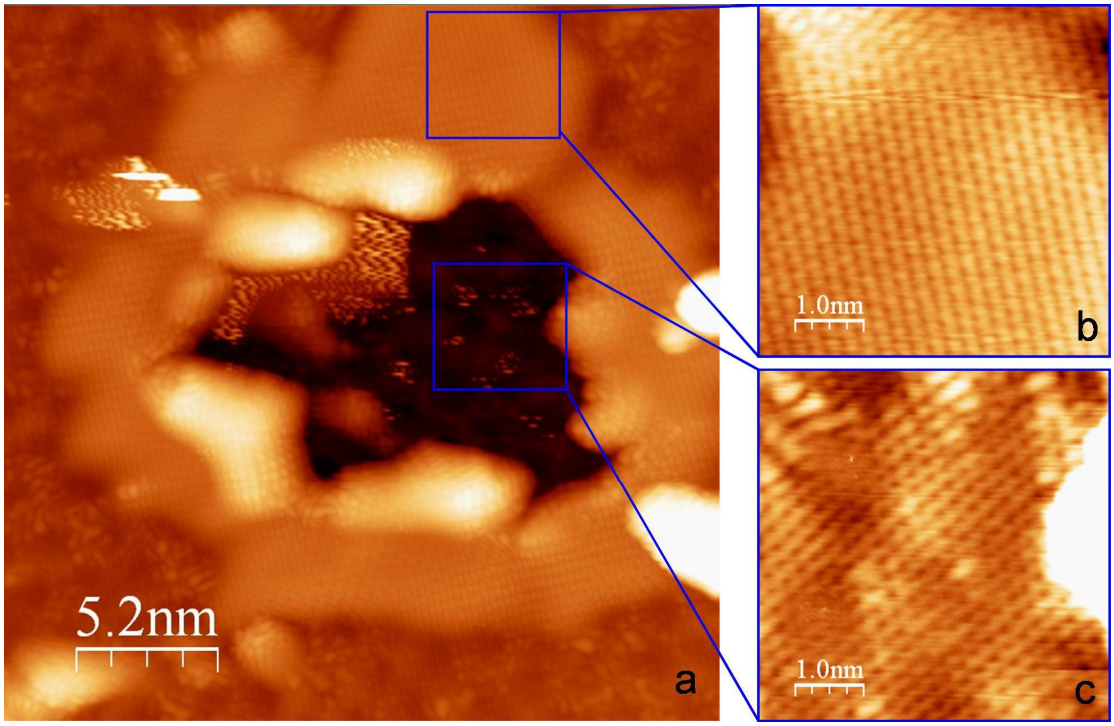

Figure 6.6. Oxidation induced pit on oxidized EG sample. a) an etch pit and its surrounding structures on the sample (0.5V, 70pA, 26 × 26nm^2); b) zoomed in image of bumps around the pit, graphene network can be distinguished (1.2V, 70pA, 5 × 5nm^2); c) zoomed in image of the bottom the etch pits, graphene network and 6 × 6 modulation can be distinguished (0.4V, 70pA, 5 × 5nm^2).

Our observations have clearly identified that flakes and clusters can be explained by the intercalation of silicon dioxide. However, the formation of pits should involve in the etching of EG layer and SiC substrate. An etch pit decorated with bumps and flakes is shown in figure 6.6. The depth of the pit center is about 0.24nm relative to the graphene outside the pit. The height difference is close to the thickness of a SiC bilayer (0.25nm), implying one silicon carbide bilayer is etched away by oxidation. Interestingly, the graphene network can still be distinguished at the bottom of pit although the EG layer inside should have been "etched". Moreover, the "6 × 6" modulation can also be distinguished, indicating the existence of the SiC nanomesh

below the graphene layer (figure 6.6c). The stacking of graphene and SiC nanomesh layer inside the pit implies that they are probably regenerated at high annealing temperature during oxidation. As observed in SiC nanomesh oxidation, the nanomesh layer can be transformed into EG at temperatures as low as 600°C under oxygen partial pressures of around 5×10^{-4} torr. The sample temperature (~1050°C) during oxidation is thus sufficient to generate the SiC nanomesh layer. Thus, after etching of EG, the pit bottom is covered by the regenerated graphene and SiC nanomesh. However, regeneration of one entire graphene layer requires three SiC bilayers, whereas only one bilayer is etched in figure 6.6. Hence, the pit formation cannot be explained by the simple removal of the top graphene/nanomesh layers. Both rearrangement and partial etching are probably involved in the formation of pits.

From the STM images, graphene networks are observed above all nanostructures on the oxidized sample. Thus, the signals of Si *2p* in its 4+ states and O *1s* are all contributed from the silicon dioxide intercalated below the top EG layer. This is consistent with the observation in the nanomesh oxidation where bumps are formed below the generated graphene layer. The intercalated silicon dioxide confirms the penetration of oxygen molecules through EG at elevated temperatures.

As all observed silicon dioxides are covered by a graphene layer, the intercalation of oxygen appears to be a dominant process. However, this contradicts the assertion that direct penetration of graphene layer is energetically unfavorable.[190] The penetration of molecules/atoms through the graphene layer has been widely observed in many studies.[52, 53, 86] Normally, this penetration is postulated to occur through

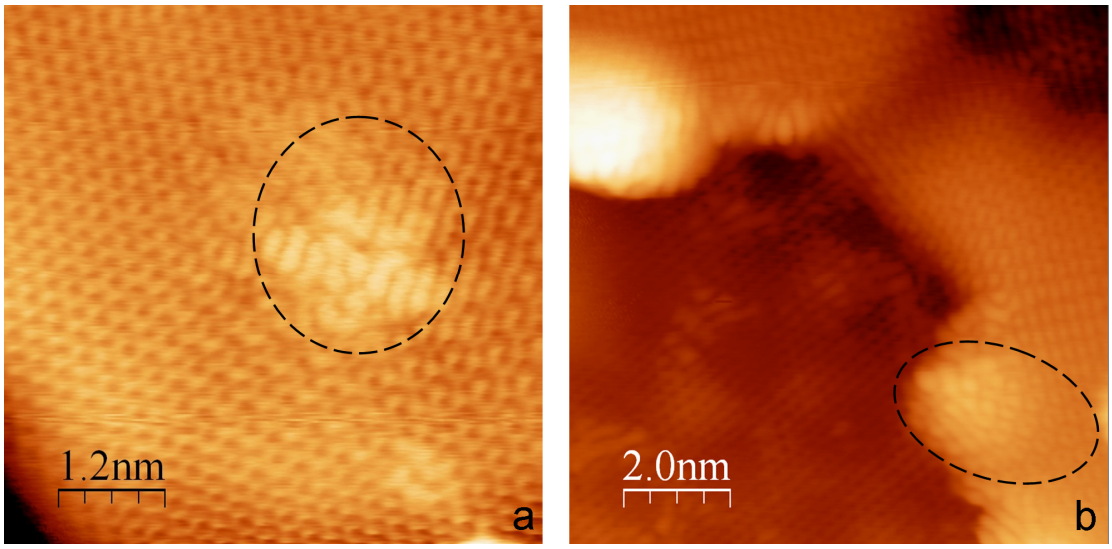

Figure 6.7. Defects on oxidized EG sample. a) point defect on graphene flake (-0.1V, 70pA, 6 × 6nm^2), b) graphene edge at the side of etch pit (0.4V, 70pA, 10 × 10nm^2).

graphene defects or domain boundaries, which have lower energy barriers for penetration. In this experiment, we observe defects and graphene boundaries mostly at the top of SiO_2 flakes (figure 6.7a, dash ellipses) and the edge of pits (figure 6.7b, dash ellipses), respectively. The discontinuity of graphene network at these sites could serve as possible routes for oxygen penetration and create a ring of clusters and flakes around the pits. However, we still observe a number of isolated flakes and clusters without any defects, indicating besides penetration, diffusion of penetrated oxygen at the interface could also be involved in the formation of silicon dioxide at the graphene/substrate interface.

In summary, oxidation of the graphene on SiC(0001) at elevated temperatures is studied by XPS and STM. Although pits generated by etching of EG are observed by STM at 1050°C, the surface is still covered by a complete graphene layer after oxidation. This observation indicates the regeneration of EG at the bottom of pits

during oxidation. XPS reveals the formation of silicon dioxide during oxidation. The silicon dioxide in the form of flakes and clusters is observed at the interface, suggesting interfacial interactions with oxygen molecules.

6.3 Iron silicide formation on epitaxial graphene

As demonstrated in the last section, oxygen molecules can penetrate the EG layer and form silicon dioxide nanostructures below it. However, very high temperatures (>1050°C) are needed for oxygen penetration of graphene on SiC. In this section, a solid iron thin film phase is deposited on EG. The penetration of iron atoms through the EG layer at much lower temperature is realized.

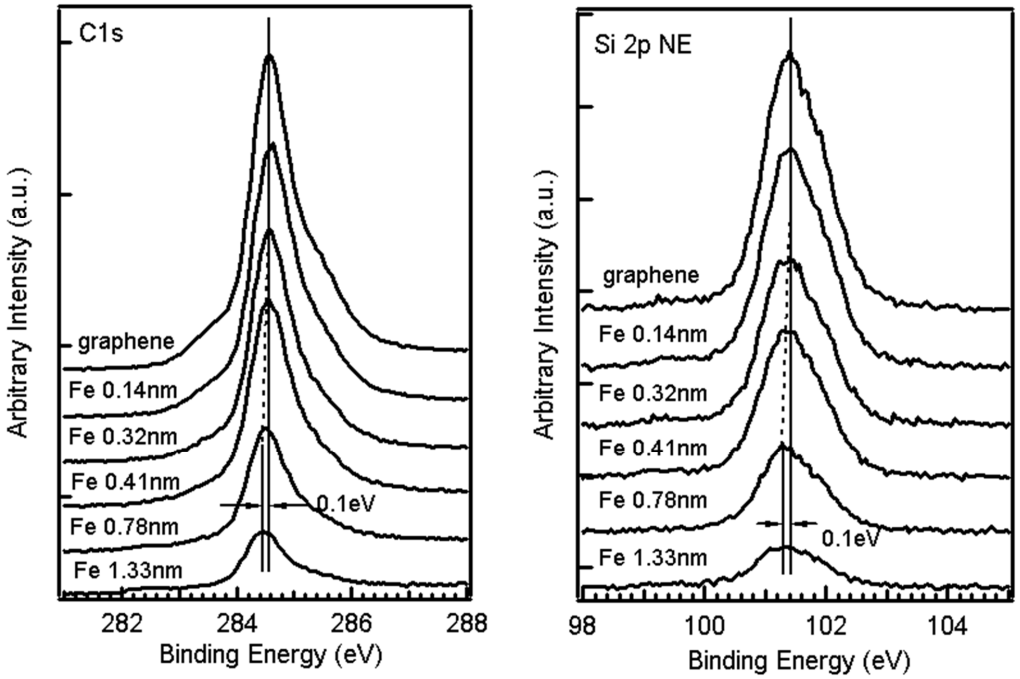

Figure 6.8. XPS spectra of C *1s* and Si *2p* of Fe deposition on graphene.

An EG sample is prepared on 6*H*-SiC(0001) by the conventional thermal graphitization process. The deposition of Fe atoms on EG is monitored by high

resolution core level photoelectron spectra (figure 6.8). During the deposition, no change of Si *2p* and C *1s* lineshapes is observed. However, a small shift (about 0.1eV) to lower binding energy in both C *1s* and Si *2p* spectra is observed by XPS after Fe deposition to a thickness of about 13.3Å. As there is no sign of surface chemical reactions, the small shift is probably owing to the polarization effect of deposited Fe atoms. Similar polarization induced binding energy shift has been observed in MgPc covered by ZnPc.[197] Meanwhile, the work function of graphene gradually increases from 4.2eV to 4.6eV after deposition of Fe. The linear increase of work function beyond one nominal layer of Fe implies a 3D growth mode in Fe deposition.

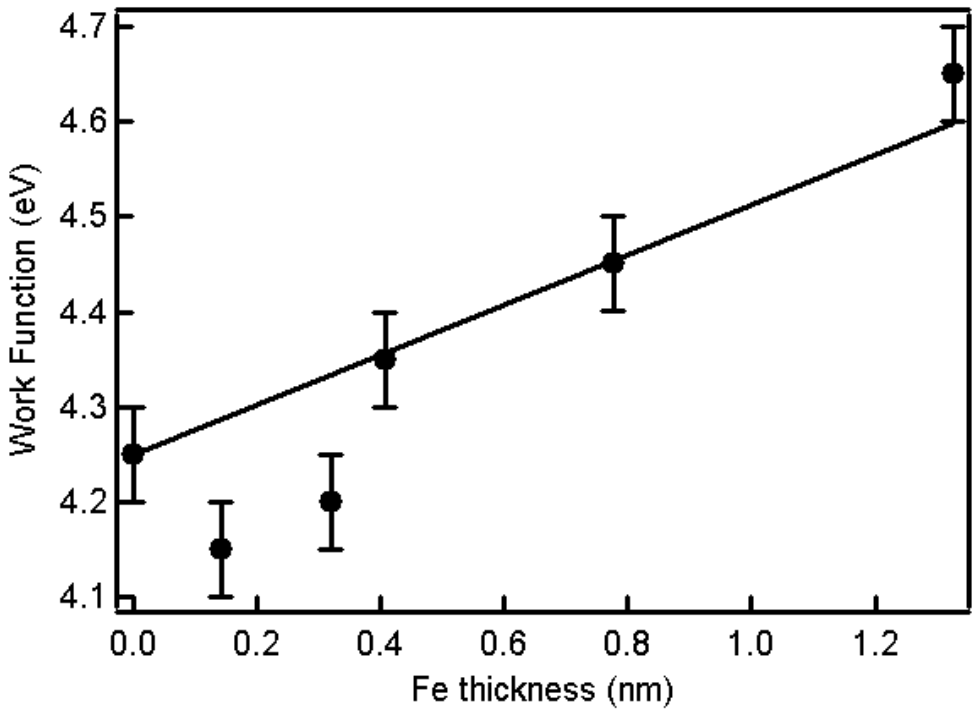

Figure 6.9. The change of work function during Fe deposition on EG.

After annealing at 600°C, the C *1s* restores to its origin intensity, indicating that the as-deposited Fe surface concentration decreases via either evaporation or

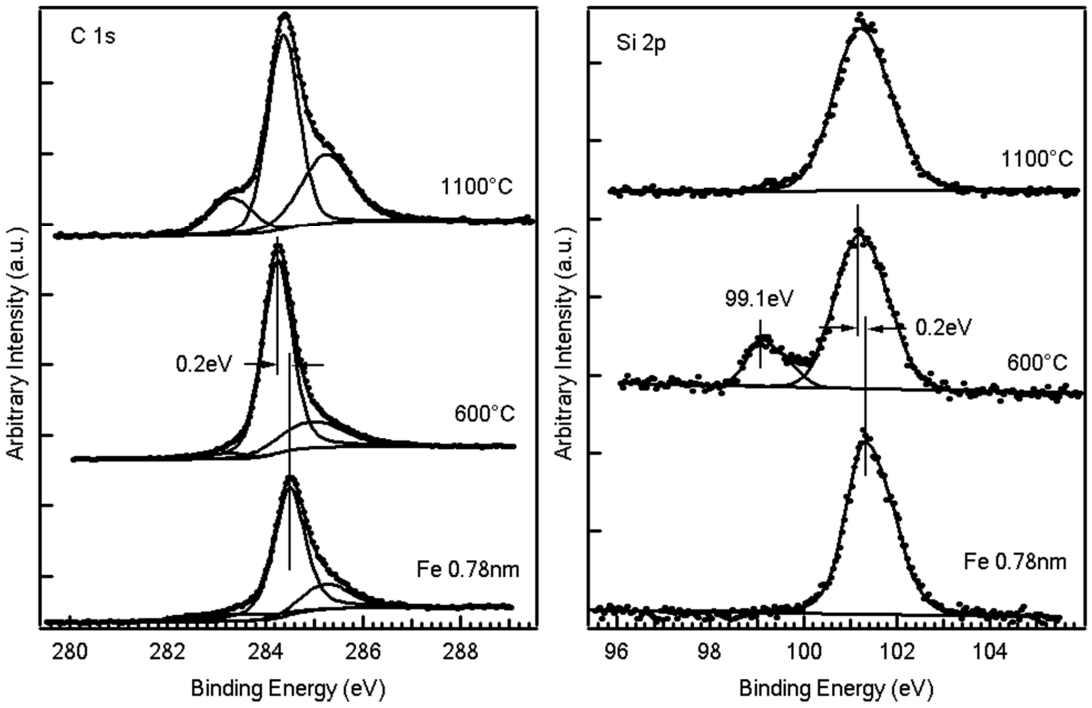

Figure 6.10. Photoemission spectra of C *1s* and Si *2p* before and after annealing.

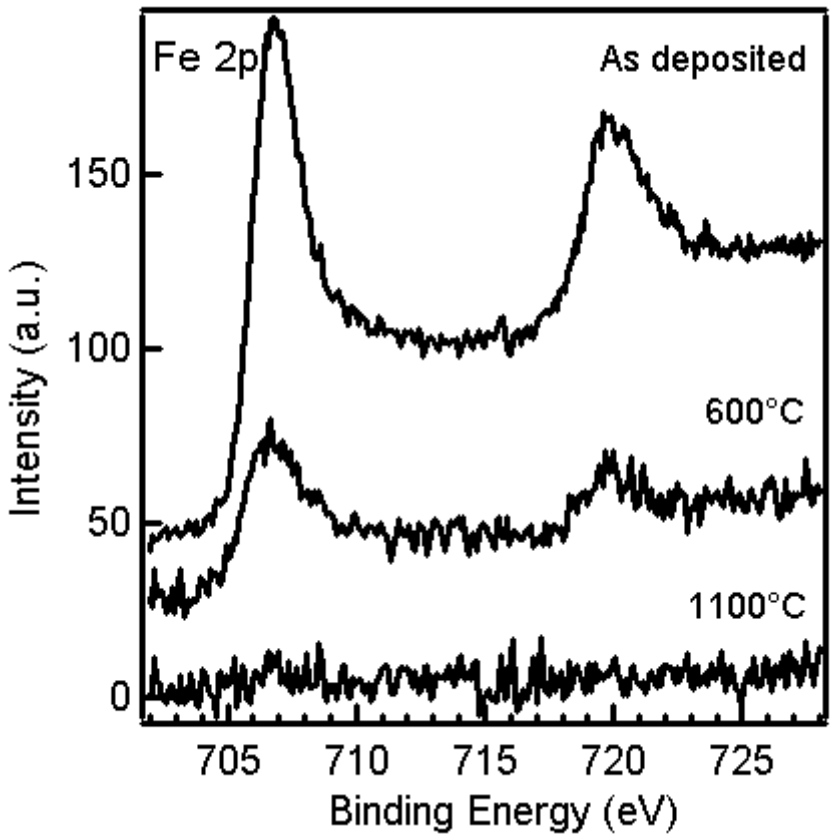

Figure 6.11. Photoemission spectra of Fe *2p* before and after annealing.

penetration. The intensity of Fe *2p* peaks decreases to about 40% of the as-deposited sample. As the Fe *2p* signals attenuated by one EG layer only reduces the intensity to about 70% of the as-deposited sample, a small portion of iron atoms must have evaporated during 600°C annealing. In the Si *2p* spectrum, a new component at 99.1eV is shown, suggesting a chemical reaction between silicon carbide and iron atoms. As the silicon atoms are covered by the EG layer and is unlikely to segregate above the EG surface below 1000°C, the reaction could only be due to the penetration of iron atoms. The silicon with lower binding energy than bulk SiC could be attributed to elemental silicon or iron silicide. On one hand, elemental silicon has a dopant dependent binding energy of 99.25-99.45eV for n-doped silicon and 98.78-98.9eV for p-doped silicon.[198] The binding energy at 99.1eV falls just beyond these two ranges. Although non-doped silicon should have a binding energy in this energy range, it is unlikely to have undoped silicon atoms when they are mixed with iron atoms at the interface due to two reasons. First, iron atoms easily react with surface silicon atoms to form iron silicides at room and elevated temperatures.[199] Second, even if there are elemental silicon atoms at the interface, the iron atoms or iron silicides can induce charge transfer to these elemental silicon atoms resulting in a binding energy shift. On the other hand, the binding energy of iron silicides ranges from 98.9eV to 99.5eV, which fits the new component in figure 6.10. More specifically, this component could be Fe_3Si or Fe-Si solid solution instead of FeSi or $FeSi_2$ because the former two have a binding energies from 98.9eV to 99.1eV while the later two is from 99.3eV to 99.5eV[199]. In figure 6.10, the C *1s* and Si *2p* spectra

show a consistent 0.2eV shift to lower binding energy. The shift of carbon and silicon peaks is attributed to band bending after iron silicide formation. Similar shifts after iron deposition are also observed on Si(100) 2 × 1 and Si(111) 7 × 7.[199, 200]

When the annealing temperature reaches 1100°C, both Fe *2p* and Si *2p* peaks at 99.1eV diminish. The iron silicide is decomposed and iron atoms are evaporated from the graphene substrate interface at this temperature. This observation suggests that the intercalation process of iron atoms can be reversed at 1100°C.

As inferred from the thermal stability of silicon atoms at 600°C, the iron silicide compounds are located below the EG layer. This conclusion is further supported by XPS depth profile measurements. By exploiting the short mean free path of outgoing photoelectrons (~nm), XPS core level spectra at two photoelectron emission angles (normal emission and grazing emission) are measured. By comparing the intensities at both angles, the depth of different layers on the surface can be determined. Although this method is only semi-quantitative due to uncertainty in the electron escape depth and surface topography, the qualitative determination of surface and bulk components using this method is widely used in surface science depending on the systems studied.[17, 18] The EG system we studied here is suitable for XPS depth profile measurements because the both EG layer and SiC nanomesh can be considered the perfect 2D layers.[54, 201] Thus, the depth determination of iron atoms using XPS depth profile is greatly simplified.

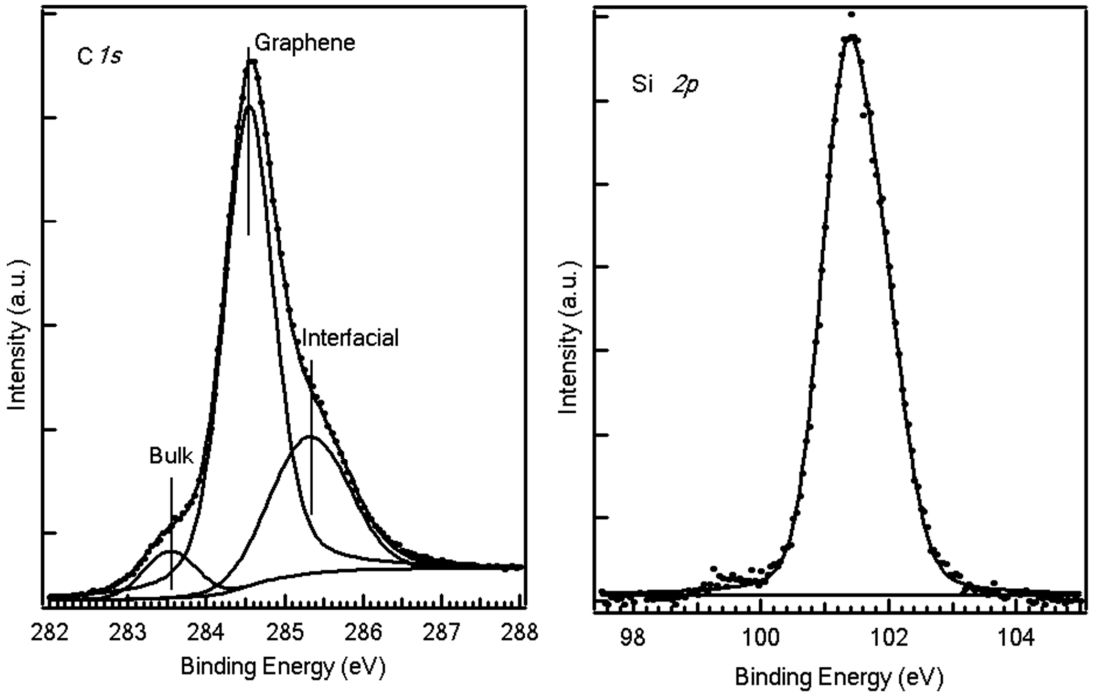

Figure 6.12. C *1s* and Si *2p* core level photoemission of EG.

Before performing the measurements, a clean graphene sample is measured as a model system to examine the feasibility of this method. The EG on SiC(0001) has an ideal layer-by-layer structure. The SiC bulk is covered by a layer of SiC nanomesh and an outmost graphene layer. This lamellar structure has been confirmed by cross-section TEM observation.[54] The z-position of these two layers can be distinguished from the three components of the C *1s* spectrum (figure 6.12). The strongest peak in the middle originates from the carbon atoms in sp^2 hybridization. These carbon atoms are mainly located in the graphene layer, though some portion of sp^2 carbon atoms are in the interfacial layer as well. The higher binding energy shoulder labeled by "interfacial" represents the carbon signal from the SiC nanomesh at the interface (C *1s* (I)). The lower binding energy shoulder originates from the bulk carbon atoms (C

1s (B)) in SiC. In the Si *2p* spectrum, the Si *2p* peak only originates from the bulk, which should have the same surface sensitivity as the C *1s* low energy shoulder. Thus, the intensities of C *1s* and Si *2p* components at normal (90°) and grazing (40°) photoelectron emission angles should be consistent with the EG structure.

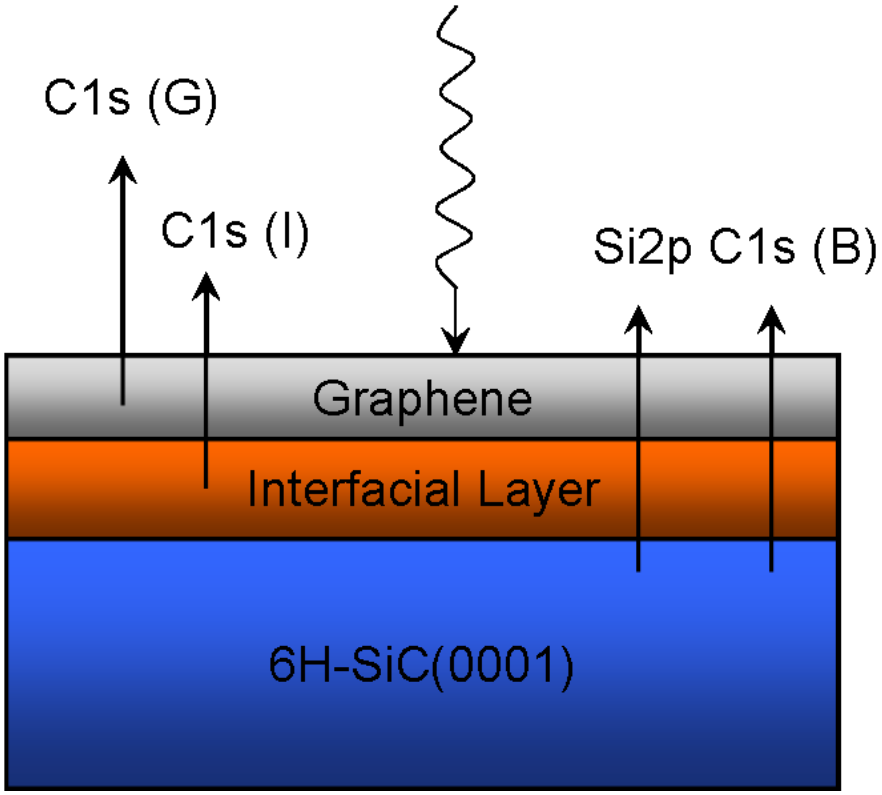

Figure 6.13. A schematic layer-by-layer model of EG on SiC, photoemission signals from different layers are shown.

Table 6.1. C *1s* and Si *2p* photoemission intensities at two angles of clean EG sample.

Normal Emission (NE) 90°				Grazing Emission (GE) 40°			
C*1s*(G)	C*1s*(I)	C*1s*(B)	Si *2p*	C*1s*(G)	C*1s*(I)	C*1s*(B)	Si *2p*
911.74	305.43	71.26	181.49	711.71	229.94	25.5	75.34
Relative Intensity (NE/GE)							
1.281	1.328	2.794	2.409				

Table 6.1 summarizes the measured intensities of C *1s* peaks and Si *2p* peak at two angles. As the intensity of the same peak may show a dependence on the emission

angle due to the layer-dependent chemical composition depth profile, the relative intensities obtained by normal emission intensity divided by grazing emission intensity is used to determine the depth of different species layers: the larger the relative intensity, the deeper the corresponding component. The order of surface to bulk from XPS measurement is C*1s* (G), C*1s* (I), Si *2p* and C *1s* (B). Both Si *2p* and C *1s* (B) NE/GE relative intensities indicate the SiC bulk component have the largest the relative intensity. Since the SiC sample used is silicon-terminated, silicon atoms are closer to surface than the carbon atoms. This explains the smaller value of Si *2p* than C *1s* (B). Thus, the XPS depth profile measurements are accurate in determining the sequence of different atomic layers for EG on SiC. The results are consistent with the graphene layer-by-layer model shown in figure 6.13. However, it should be noted that this method may not give a correct thickness of the surface layers. For example, the absolute thickness of top graphene layer calculated using attenuation of C *1s* (I) at different angles using $I(\theta) = I_0 e^{-\frac{d}{\lambda \cos\theta}}$ and IMFP of graphene (4.4Å)[202] only gives thickness about 0.2Å, much thinner than the thickness measured by other experimental methods (3.3-3.5Å).[54, 201] This is partially due to the fact that the C *1s* (G) signal also comes from the interfacial layer and makes the NE/GE ratio larger than expected.

Next, the XPS depth profile measurements are done on the annealed Fe-deposited sample. The proposed structure model is shown in figure 6.14. In this model, the Si *2p* (I) (the new Si *2p* component at 99.1eV in figure 6.10) is used to represent the iron silicide layer. This layer, which is buried by graphene layer, should show a larger

NE/GE ratio than graphene but smaller than the bulk. The normalized photoelectron intensities are listed in table 6.2 in two angles. The relative intensity of Si *2p* (I) component in this table clearly shows a larger value than that of C *1s* (G) component

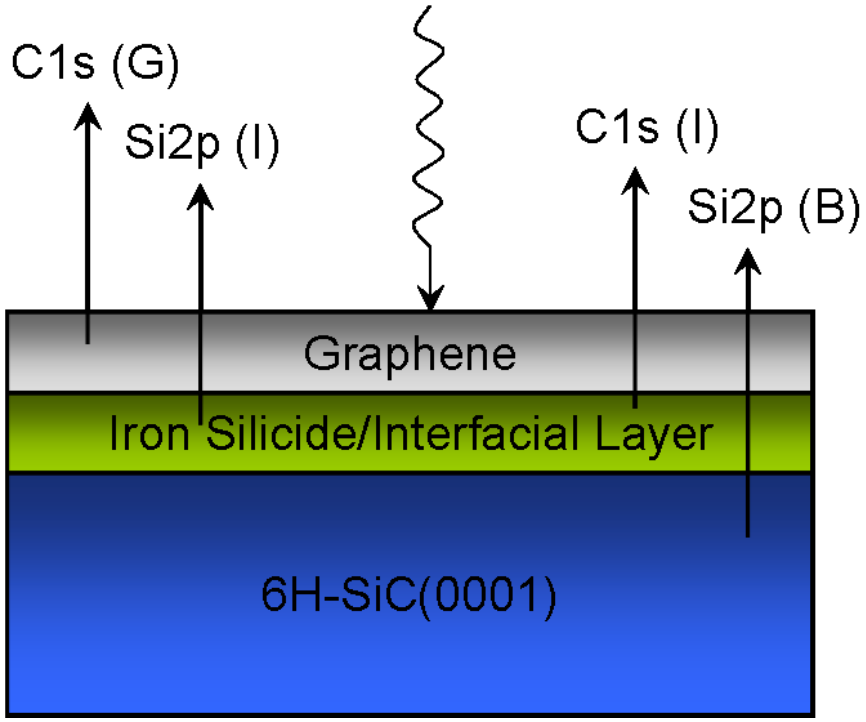

Figure 6.14. A schematic picture of z-position of iron silicide in EG sample, the iron silicide is proposed at the interfacial layer.

Table 6.2. C *1s* and Si *2p* photoemission intensities at two angles of iron silicide intercalated EG sample.

Normal Emission (NE) 90°				Grazing Emission (GE) 40°			
Si*2p*(B)	Si*2p*(I)	C*1s*(I)	C*1s*(G)	Si*2p*(B)	Si*2p*(I)	C*1s*(I)	C*1s*(G)
61.91	11.77	294.47	989.31	22.02	8.04	178.68	805.68
Relative Intensity (NE/GE)							
2.811	1.464	1.648	1.228				

but smaller than that of Si *2p* (B). These data confirm the intercalation of iron atoms. In table 6.2, it can be found that Si *2p* (I) is also smaller than C *1s* (I). However, it may not be sufficient to conclude that the buffer layer is below the iron silicide. This

is because the silicon atoms in iron silicide is provided from the buffer layer and may change the structure of the buffer layer. In summary, the intercalation model of iron silicide shown in figure 6.14 is verified by the XPS depth profile measurements.

Herein, the intercalation and chemical reactions of iron atoms on EG is confirmed by synchrotron-based XPS studies. At room temperature, the linear change of work function implies a 3D growth of iron on EG. At 600°C, iron atoms intercalate beneath the graphene layer and form iron silicide at the interface. From the binding energy of Si *2p*, the iron silicide compound is probably Fe_3Si or Fe-Si solid solution. When the annealing temperature reaches 1100°C, the iron silicide is decomposed and iron atoms are evaporated from the sample surface.

6.4 Summary

Intercalation as well as reaction of oxygen molecules and iron atoms on epitaxial graphene on SiC(0001) are studied by STM and XPS. Both reactants can intercalate between EG and the SiC substrate and react with silicon atoms at the interface at elevated temperatures. In the case of oxygen intercalation, silicon dioxide is formed at the interface; while in the case of iron intercalation, iron silicide is generated at the interface. Although oxygen can also etch the graphene layer to form deep pits on the surface at high temperatures, EG is regenerated at the bottom of these pits. This intercalated chemical reaction provides a new route to engineer supported EG on various interlayers. In particular, the ability to form an insulting silicon dioxide

interlayer beneath EG offers an attractive route for the fabrication of graphene-based devices.

The intercalation reactions of SiC nanomesh point to an alternative way to study the atomic structure of SiC nanomesh and its transition to epitaxial graphene. Due to high annealing temperature for the formation of graphene (1200°C), it is difficult to study this transition dynamically. However, the intercalation reactions which also cause the nanomesh-graphene transition require much lower annealing temperature and the transition is highly dependent on the presence of reactants. Thus, to manually slow down the transition via temperature control or reactant control becomes possible. This provides a convenient method to study the initial stage of the nanomesh-graphene transition.

CHAPTER 7 CONCLUSION AND OUTLOOK

The aim of this thesis is to study the SiC nanomesh structure and its possible applications. These two targets are interconnected. The discovery of silicon atoms in the nanomesh enables the reaction of SiC nanomesh to adsorbates, such as oxygen molecules; while the nanomesh-graphene transition caused by oxidation suggests that the SiC nanomesh structure may partially resemble the graphene framework.

The structure of SiC nanomesh is studied by complementary surface analytical techniques. The silicon atoms are investigated by XAS technique in this thesis. The EXAFS study reveals the bulk silicon vacancies with a depth of the order of the mean free path of emitted x-ray fluorescence photons, which suggests that the formation of SiC involves not only surface reconstructions, but also the creation of bulk silicon vacancies. The NEXAFS study reveals the presence of silicon-silicon bonds at the SiC nanomesh surface. This observation proves small Si clusters formed on this surface with silicon-silicon bonds. The XPS study under extended annealing of SiC nanomesh reveals an intensity decrease of Si *2p* peaks but an increase of C *1s* peaks, indicating that the SiC nanomesh has a variable Si and C stoichiometric ratio depending on the annealing duration. STM observations reveal local and medium range disorders in SiC nanomesh. These disorders further suggest that the SiC nanomesh may contain different self-organized structures. From these studies, the SiC nanomesh exhibits so many differences from the other reconstructions in this evolution that it should not be regarded a single surface reconstruction. Instead, we propose this unique surface to be a collection of local self-organized structures due to

silicon desorption. However, more work needs to be done to fully understand this unique and complicated structure. Experimental studies and calculations focusing on the local structures of the SiC nanomesh should be helpful to understand this structure.

Altering the structure of SiC nanomesh via chemical reaction is attempted during this work. Oxidation of the SiC nanomesh above 600ºC actually transforms it into single layer graphene. This temperature is much lower than the nanomesh-graphene transition temperature by annealing. This observation implies the structure of SiC nanomesh should have a close relationship to the graphene-like framework. During the oxidation, silicon oxides are generated below the top single layer graphene, exhibiting oxygen intercalation on this surface. This intercalation property is further explored on the EG surface where the SiC nanomesh is concealed below the top EG layer. Both oxygen molecules and iron atoms are observed to intercalate the EG layer and to react with SiC nanomesh. Silicon dioxide and iron silicide are observed at the interface, respectively. This study evokes a possible route to engineering the EG layer via the nanomesh at lower temperatures. The intercalated silicon dioxide is in the shapes of clusters and small flakes suggesting a non-uniform intercalation process. Further studies to form uniform large-area oxide layers are needed by optimizing the parameters of the oxidation conditions.

One possible application of SiC nanomesh is its template effect to organic molecules. In the absence of strong intermolecular interactions and molecule-substrate interactions, both CuPc (4-fold symmetry) and pentacene (2-fold symmetry) show

good confinement on the SiC nanomesh surface. Especially, molecular arrays are obtained for the adsorbed CuPc molecules. It is interesting to notice that template effects appears to be only achievable for planar molecules, and the ball-like fullerene molecule cannot be confined. Thus, other types of organic molecules, especially for 3-fold symmetric molecules, should be tested on this substrate to further explore its template effects.

BIBLIOGRAPHY

1. U. Starke, *Atomic structure of hexagonal SiC surfaces*, Phys. Stat. Sol. (b), **202**, 475, (1997).
2. F. Bechstedt, P. Käckell, A. Zywietz, K. Karch, B. Adolph, K. Tenelsen and J. Furthmüller, *Polytypism and properties of silicon carbide*, Phys. Stat. Sol. (b), **202**, 35, (1997).
3. Y. Goldberg, M. Levinshtein and S. Rumyantsev, *Properties of advanced semiconductor materials GaN, AlN, InN, BN, SiC, SiGe*, John Wiley, Singapore, (2001).
4. A. R. Powell and L. B. Rowland, *SiC materials - Progress, status, and potential roadblocks*, P. IEEE, **90**, 942, (2002).
5. H. Morkoç, S. Strite, G. B. Gao, M. E. Lin, B. Sverdlov and M. Burns, *LARGE-BAND-GAP SIC, III-V NITRIDE, AND II-VI ZNSE-BASED SEMICONDUCTOR-DEVICE TECHNOLOGIES*, J. Appl. Phys., **76**, 1363, (1994).
6. J. B. Casady and R. W. Johnson, *Status of silicon carbide (SiC) as a wide-bandgap semiconductor for high-temperature applications: A review*, Solid-State Electron., **39**, 1409, (1996).
7. M. Willander, M. Friesel, Q. U. Wahab and B. Straumal, *Silicon carbide and diamond for high temperature device applications*, J. Mater. Sci.-Mater. El., **17**, 1, (2006).
8. P. Masri, *Silicon carbide and silicon carbide-based structures: The physics of epitaxy*, Surf. Sci. Rep., **48**, 1, (2002).
9. L. I. Johansson, F. Owman and P. Mårtensson, *High-resolution core-level study of 6H-SiC(0001)*, Phys. Rev. B, **53**, 13793, (1996).
10. A. J. Van Bommel, J. E. Crombeen and A. Van Tooren, *LEED and Auger electron observations of the SiC(0001) surface*, Surf. Sci., **48**, 463, (1975).
11. V. vanElsbergen, T. U. Kampen and W. Mönch, *Surface analysis of 6H-SiC*, **365**, 443, (1996).
12. X. N. Xie, H. Q. Wang, A. T. S. Wee and K. P. Loh, *The evolution of 3 x 3, 6 x 6, root 3 x root 3R30 degrees and 6 root 3 x 6 root 3R30 degrees superstructures on 6H-SiC (0001) surfaces studied by reflection high energy electron diffraction*, Surf. Sci., **478**, 57, (2001).
13. V. M. Bermudez, *Adsorption and co-adsorption of boron and oxygen on ordered [alpha]-SiC surfaces*, Appl. Surf. Sci., **84**, 45, (1995).
14. T. Jikimoto, J. L. Wang, T. Saito, M. Hirai, M. Kusaka, M. Iwami and T. Nakata, *Atomic and electronic structures of heat treated 6H-SiC surface*, Appl. Surf. Sci., **130-132**, 593, (1998).
15. L. Li and I. S. T. Tsong, *Atomic structures of 6H-SiC(0001) and (0001) surfaces*, Surf. Sci., **351**, 141, (1996).
16. F. Amy, P. Soukiassian, Y. K. Hwu and C. Brylinski, *Identification of the 6H-SiC(0001) 3 x 3 surface reconstruction core-level shifted components*, Surf. Sci., **464**, L691, (2000).
17. J. E. Northrup and J. Neugebauer, *Theory of the adatom-induced reconstruction of the SiC(0001)root 3x root 3 surface*, Phys. Rev. B, **52**, R17001, (1995).
18. U. Starke, J. Schardt, J. Bernhardt, M. Franke, K. Reuter, H. Wedler, K. Heinz, J. Furthmüller, P. Käckell and F. Bechstedt, *Novel reconstruction mechanism for dangling-bond minimization: Combined method surface structure determination of SiC(111)-(3x3)*, Phys. Rev. Lett., **80**, 758, (1998).
19. J. Schardt, J. Bernhardt, U. Starke and K. Heinz, *Crystallography of the (3 <rm>x</rm> 3) surface reconstruction of 3C-SiC(111), 4H-SiC(0001), and 6H-SiC(0001) surfaces retrieved by low-energy electron diffraction*, Phys. Rev. B, **62**, 10335, (2000).

20. W. Chen, X. N. Xie, H. Xu, A. T. S. Wee and K. P. Loh, *Atomic Scale Oxidation of Silicon Nanoclusters on Silicon Carbide Surfaces*, J. Phys. Chem. B, **107**, 11597, (2003).

21. F. Amy, P. Soukiassian, Y. K. Hwu and C. Brylinski, *SiO2/6H-SiC(0001)3x3 initial interface formation by Si overlayer oxidation*, Appl. Phys. Lett., **75**, 3360, (1999).

22. F. Amy, H. Enriquez, P. Soukiassian, P. F. Storino, Y. J. Chabal, A. J. Mayne, G. Dujardin, Y. K. Hwu and C. Brylinski, *Atomic scale oxidation of a complex system: O-2/alpha-SiC(0001)-(3x3)*, Phys. Rev. Lett., **86**, 4342, (2001).

23. G. Baffou, A. J. Mayne, G. Comtet, G. Dujardin, P. Sonnet and L. Stauffer, *Anchoring phthalocyanine molecules on the 6H-SiC(0001)3x3 surface*, Appl. Phys. Lett., **91**, 073101, (2007).

24. S. Nakanishi, H. Tokutaka, K. Nishimori, S. Kishida and N. Ishihara, *THE DIFFERENCE BETWEEN 6H-SIC (0001) AND (0001) FACES OBSERVED BY AES, LEED AND ESCA*, Appl. Surf. Sci., **41-2**, 44, (1989).

25. U. Starke, C. Bram, P. R. Steiner, W. Hartner, L. Hammer, K. Heinz and K. Müller, *The (0001)-surface of 6H---SiC: morphology, composition and structure*, App. Surf. Sci., **89**, 175, (1995).

26. F. Owman and P. Mårtensson, *The SiC(0001)6 root x6 root 3 reconstruction studied with STM and LEED*, Surf. Sci., **369**, 126, (1996).

27. S. Takahashi, S. Hatta, A. Yoshigoe, Y. Teraoka and T. Aruga, *High resolution X-ray photoelectron spectroscopy study on initial oxidation of 4H-SiC(0001)-(root 3 x root 3)R30 degrees surface*, Surf. Sci., **603**, 221, (2009).

28. W. Chen, H. Xu, L. Liu, X. Y. Gao, D. C. Qi, G. W. Peng, S. C. Tan, Y. P. Feng, K. P. Loh and A. T. S. Wee, *Atomic structure of the 6H-SiC(0001) nanomesh*, Surf. Sci., **596**, 176, (2005).

29. C. Riedl, U. Starke, J. Bernhardt, M. Franke and K. Heinz, *Structural properties of the graphene-SiC(0001) interface as a key for the preparation of homogeneous large-terrace graphene surfaces*, Phys. Rev. B, **76**, 245406, (2007).

30. A. Charrier, A. Coati, T. Argunova, F. Thibaudau, Y. Garreau, R. Pinchaux, I. Forbeaux, J. M. Debever, M. Sauvage-Simkin and J. M. Themlin, *Solid-state decomposition of silicon carbide for growing ultra-thin heteroepitaxial graphite films*, J. Appl. Phys., **92**, 2479, (2002).

31. K. S. Novoselov, A. K. Geim, S. V. Morozov, D. Jiang, Y. Zhang, S. V. Dubonos, I. V. Grigorieva and A. A. Firsov, *Electric field effect in atomically thin carbon films*, Science, **306**, 666, (2004).

32. K. S. Novoselov, A. K. Geim, S. V. Morozov, D. Jiang, M. I. Katsnelson, I. V. Grigorieva, S. V. Dubonos and A. A. Firsov, *Two-dimensional gas of massless Dirac fermions in graphene*, Nature, **438**, 197, (2005).

33. K. S. Novoselov, D. Jiang, F. Schedin, T. J. Booth, V. V. Khotkevich, S. V. Morozov and A. K. Geim, *Two-dimensional atomic crystals*, Proc. Natl. Acad. Sci. U.S.A., **102**, 10451, (2005).

34. C. Berger, Z. M. Song, T. B. Li, X. B. Li, A. Y. Ogbazghi, R. Feng, Z. T. Dai, A. N. Marchenkov, E. H. Conrad, P. N. First and W. A. de Heer, *Ultrathin epitaxial graphite: 2D electron gas properties and a route toward graphene-based nanoelectronics*, J. Phys. Chem. B, **108**, 19912, (2004).

35. C. Berger, Z. M. Song, X. B. Li, X. S. Wu, N. Brown, C. Naud, D. Mayou, T. B. Li, J. Hass, A. N. Marchenkov, E. H. Conrad, P. N. First and W. A. de Heer, *Electronic confinement and coherence in patterned epitaxial graphene*, Science, **312**, 1191, (2006).

36. A. Bostwick, T. Ohta, T. Seyller, K. Horn and E. Rotenberg, *Quasiparticle dynamics in graphene*, Nature Phys., **3**, 36, (2007).

37. A. Bostwick, T. Ohta, J. L. McChesney, K. V. Emtsev, T. Seyller, K. Horn and E. Rotenberg, *Symmetry breaking in few layer graphene films*, New J. Phys., **9**, (2007).
38. W. A. de Heer, C. Berger, X. S. Wu, P. N. First, E. H. Conrad, X. B. Li, T. B. Li, M. Sprinkle, J. Hass, M. L. Sadowski, M. Potemski and G. Martinez, *Epitaxial graphene*, Solid State Commun., **143**, 92, (2007).
39. S. Y. Zhou, G. H. Gweon, A. V. Fedorov, P. N. First, W. A. De Heer, D. H. Lee, F. Guinea, A. H. C. Neto and A. Lanzara, *Substrate-induced bandgap opening in epitaxial graphene*, Nature mater., **6**, 770, (2007).
40. W. Chen, S. Chen, D. C. Qi, X. Y. Gao and A. T. S. Wee, *Surface transfer p-type doping of epitaxial graphene*, J. Am. Chem. Soc., **129**, 10418, (2007).
41. T. Seyller, A. Bostwick, K. V. Emtsev, K. Horn, L. Ley, J. L. McChesney, T. Ohta, J. D. Riley, E. Rotenberg and F. Speck, *Epitaxial graphene: a new material*, Phys. Stat. Sol. (b), **245**, 1436, (2008).
42. H. Huang, W. Chen, S. Chen and A. T. S. Wee, *Bottom-up Growth of Epitaxial Graphene on 6H-SiC(0001)*, ACS Nano, **2**, 2513, (2008).
43. E. Rollings, G. H. Gweon, S. Y. Zhou, B. S. Mun, J. L. McChesney, B. S. Hussain, A. Fedorov, P. N. First, W. A. de Heer and A. Lanzara, *Synthesis and characterization of atomically thin graphite films on a silicon carbide substrate*, J. Phys. Chem. Solids, **67**, 2172, (2006).
44. M. Hupalo, E. H. Conrad and M. C. Tringides, *Growth mechanism for epitaxial graphene on vicinal 6H-SiC(0001) surfaces: A scanning tunneling microscopy study*, Phys. Rev. B, **80**, 041401(R), (2009).
45. W. Norimatsu and M. Kusunoki, *Formation process of graphene on SiC (0001)*, Physica E, **42**, 691, (2010).
46. G. M. Rutter, N. P. Guisinger, J. N. Crain, P. N. First and J. A. Stroscio, *Edge structure of epitaxial graphene islands*, Phys. Rev. B, **81**, 245408, (2010).
47. N. P. Guisinger, G. M. Rutter, J. N. Crain, C. Heiliger, P. N. First and J. A. Stroscio, *Atomic-scale investigation of graphene formation on 6H-SiC(0001)*, J. Vac. Sci. Technol. A, **26**, 932, (2008).
48. M. L. Bolen, S. E. Harrison, L. B. Biedermann and M. A. Capano, *Graphene formation mechanisms on 4H-SiC(0001)*, Phys. Rev. B, **80**, 115433, (2009).
49. M. H. Tsai, C. S. Chang, J. D. Dow and I. S. T. Tsong, *ELECTRONIC CONTRIBUTIONS TO SCANNING-TUNNELING-MICROSCOPY IMAGES OF AN ANNEALED BETA-SIC(111) SURFACE*, Phys. Rev. B, **45**, 1327, (1992).
50. I. Forbeaux, J. M. Themlin and J. M. Debever, *Heteroepitaxial graphite on 6H-SiC(0001): Interface formation through conduction-band electronic structure*, Phys. Rev. B, **58**, 16396, (1998).
51. K. V. Emtsev, F. Speck, T. Seyller, L. Ley and J. D. Riley, *Interaction, growth, and ordering of epitaxial graphene on SiC{0001} surfaces: A comparative photoelectron spectroscopy study*, Phys. Rev. B, **77**, 155303, (2008).
52. C. Riedl, C. Coletti, T. Iwasaki, A. A. Zakharov and U. Starke, *Quasi-Free-Standing Epitaxial Graphene on SiC Obtained by Hydrogen Intercalation*, Phys. Rev. Lett., **103**, 246804, (2009).
53. C. Virojanadara, A. A. Zakharov, R. Yakimova and L. I. Johansson, *Buffer layer free large area bi-layer graphene on SiC(0001)*, Surf. Sci., **604**, L4, (2010).
54. J. Borysiuk, R. Bożek, W. Strupiński, A. Wysmołek, K. Grodecki, R. Stępniewski and J. M. Baranowski, *Transmission electron microscopy and scanning tunneling microscopy investigations of graphene on 4H-SiC(0001)*, J. Appl. Phys., **105**, 023503, (2009).

55. L. Simon, J. L. Bischoff and L. Kubler, *X-ray photoelectron characterization of 6H-SiC(0001)*, Phys. Rev. B, **60**, 11653, (1999).

56. J. Hass, J. E. Millán-Otoya, P. N. First and E. H. Conrad, *Interface structure of epitaxial graphene grown on 4H-SiC(0001)*, Phys. Rev. B, **78**, 205424, (2008).

57. Y. Qi, S. H. Rhim, G. F. Sun, M. Weinert and L. Li, *Epitaxial graphene on SiC(0001): Morethan just honeycombs*, Phys. Rev. Lett., **105**, 085502, (2010).

58. S. Kim, J. Ihm, H. J. Choi and Y. W. Son, *Origin of anomalous electronic structures of epitaxial graphene on silicon carbide*, Phys. Rev. Lett., **100**, 176802, (2008).

59. W. J. Ong and E. S. Tok, *Role of Si clusters in the phase transformation and formation of (6x6)-ring structures on 6H-SiC(0001) as a function of temperature: An STM and XPS study*, Phys. Rev. B, **73**, 045330, (2006).

60. S. W. Poon, W. Chen, E. S. Tok and A. T. S. Wee, *Probing epitaxial growth of graphene on silicon carbide by metal decoration*, Appl. Phys. Lett., **92**, 104102, (2008).

61. R. M. Tromp and J. B. Hannon, *Thermodynamics and Kinetics of Graphene Growth on SiC(0001)*, Phys. Rev. Lett., **102**, 106104, (2009).

62. A. Stabel, P. Herwig, K. Müllen and J. P. Rabe, *DIODE-LIKE CURRENT-VOLTAGE CURVES FOR A SINGLE MOLECULE-TUNNELING SPECTROSCOPY WITH SUBMOLECULAR RESOLUTION OF AN ALKYLATED, PERICONDENSED HEXABENZOCORONENE*, Angew. Chem. Int. Ed. Engl., **34**, 1609, (1995).

63. Z. Yao, H. W. C. Postma, L. Balents and C. Dekker, *Carbon nanotube intramolecular junctions*, Nature, **402**, 273, (1999).

64. H. Park, J. Park, A. K. L. Lim, E. H. Anderson, A. P. Alivisatos and P. L. McEuen, *Nanomechanical oscillations in a single-C-60 transistor*, Nature, **407**, 57, (2000).

65. W. J. Liang, M. P. Shores, M. Bockrath, J. R. Long and H. Park, *Kondo resonance in a single-molecule transistor*, Nature, **417**, 725, (2002).

66. C. P. Collier, G. Mattersteig, E. W. Wong, Y. Luo, K. Beverly, J. Sampaio, F. M. Raymo, J. F. Stoddart and J. R. Heath, *A 2 catenane-based solid state electronically reconfigurable switch*, Science, **289**, 1172, (2000).

67. J. K. Gimzewski, T. A. Jung, M. T. Cuberes and R. R. Schlittler, *Scanning tunneling microscopy of individual molecules: beyond imaging*, Surf. Sci., **386**, 101, (1997).

68. M. F. Crommie, C. P. Lutz and D. M. Eigler, *CONFINEMENT OF ELECTRONS TO QUANTUM CORRALS ON A METAL-SURFACE*, Science, **262**, 218, (1993).

69. T. Kudernac, S. B. Lei, J. Elemans and S. De Feyter, *Two-dimensional supramolecular self-assembly: nanoporous networks on surfaces*, Chem. Soc. Rev., **38**, 402, (2009).

70. J. A. Theobald, N. S. Oxtoby, M. A. Phillips, N. R. Champness and P. H. Beton, *Controlling molecular deposition and layer structure with supramolecular surface assemblies*, Nature, **424**, 1029, (2003).

71. G. B. Pan, J. M. Liu, H. M. Zhang, L. J. Wan, Q. Y. Zheng and C. L. Bai, *Configurations of a calix 8 arene and a C-60/calix 8 arene complex on a Au(111) surface*, Angew. Chem.-Int. Edit., **42**, 2747, (2003).

72. U. Schlickum, R. Decker, F. Klappenberger, G. Zoppellaro, S. Klyatskaya, M. Ruben, I. Silanes, A. Arnau, K. Kern, H. Brune and J. V. Barth, *Metal-organic honeycomb nanomeshes with tunable cavity size*, Nano Lett., **7**, 3813, (2007).

73. S. Stepanow, M. Lingenfelder, A. Dmitriev, H. Spillmann, E. Delvigne, N. Lin, X. B. Deng, C. Z. Cai, J. V. Barth and K. Kern, *Steering molecular organization and host-guest interactions using two-dimensional nanoporous coordination systems*, Nature Mater., **3**, 229, (2004).

74. S. Lei, M. Surin, K. Tahara, J. Adisoejoso, R. Lazzaroni, Y. Tobe and S. De Feyter, *Programmable hierarchical three-component 2D assembly at a liquid-solid interface: Recognition, selection, and transformation*, Nano Lett., **8**, 2541, (2008).

75. G. Schull, L. Douillard, C. Fiorini-Debuisschert, F. Charra, F. Mathevet, D. Kreher and A. J. Attias, *Single-molecule dynamics in a self-assembled 2D molecular sieve*, Nano Lett., **6**, 1360, (2006).

76. H. Spillmann, A. Kiebele, M. Stöhr, T. A. Jung, D. Bonifazi, F. Y. Cheng and F. Diederich, *A two-dimensional porphyrin-based porous network featuring communicating cavities for the templated complexation of fullerenes*, Adv. Mater., **18**, 275, (2006).

77. N. Neél, J. Kröger and R. Berndt, *Highly periodic fullerene nanomesh*, Adv. Mater., **18**, 174, (2006).

78. H. Brune, M. Giovannini, K. Bromann and K. Kern, *Self-organized growth of nanostructure arrays on strain-relief patterns*, Nature, **394**, 451, (1998).

79. M. Böhringer, K. Morgenstern, W. D. Schneider, R. Berndt, F. Mauri, A. De Vita and R. Car, *Two-dimensional self-assembly of supramolecular clusters and chains*, Phys. Rev. Lett., **83**, 324, (1999).

80. H. Dil, J. Lobo-Checa, R. Laskowski, P. Blaha, S. Berner, J. Osterwalder and T. Greber, *Surface trapping of atoms and molecules with dipole rings*, Science, **319**, 1824, (2008).

81. V. Repain, G. Baudot, H. Ellmer and S. Rousset, *Two-dimensional long-range-ordered growth of uniform cobalt nanostructures on a Au(111) vicinal template*, Europhys. Lett., **58**, 730, (2002).

82. M. Corso, W. Auwärter, M. Muntwiler, A. Tamai, T. Greber and J. Osterwalder, *Boron nitride nanomesh*, Science, **303**, 217, (2004).

83. S. Berner, M. Corso, R. Widmer, O. Groening, R. Laskowski, P. Blaha, K. Schwarz, A. Goriachko, H. Over, S. Gsell, M. Schreck, H. Sachdev, T. Greber and J. Osterwalder, *Boron nitride nanomesh: Functionality from a corrugated monolayer*, Angew. Chem.-Int. Edit., **46**, 5115, (2007).

84. W. Chen, K. P. Loh, H. Xu and A. T. S. Wee, *Growth of monodispersed cobalt nanoparticles on 6H-SiC(0001) honeycomb template*, Appl. Phys. Lett., **84**, 281, (2004).

85. A. M. Shikin, Y. S. Dedkov, V. K. Adamchuk, D. Farias and K. H. Rieder, *Modification of electronic and atomic structure upon intercalation of C-60 molecules underneath a graphite monolayer on Ni(111)*, Mol. Mater., **13**, 177, (2000).

86. A. M. Shikin, Y. S. Dedkov, V. K. Adamchuk, D. Farias and K. H. Rieder, *Formation of an intercalation-like system by intercalation of C-60 molecules underneath a graphite monolayer on Ni(111)*, Surf. Sci., **452**, 1, (2000).

87. A. M. Shikin, V. K. Adamchuk and K. H. Rieder, *Formation of quasi-free graphene on the Ni(111) surface with intercalated Cu, Ag, and Au layers*, Phys. Solid State, **51**, 2390, (2009).

88. A. M. Shikin, D. Farías, V. K. Adamchuk and K. H. Rieder, *Surface phonon dispersion of a graphite monolayer adsorbed on Ni(111) and its modification caused by intercalation of Yb, La and Cu layers*, Surf. Sci., **424**, 155, (1999).

89. Y. S. Dedkov, M. Fonin, U. Rüdiger and C. Laubschat, *Graphene-protected iron layer on Ni(111)*, Appl. Phys. Lett., **93**, 022509, (2008).

90. A. K. Geim, *Graphene: Status and Prospects*, Science, **324**, 1530, (2009).

91. S. Hüfner, *Photoelectron Spectroscopy: Principles and Applications*, Springer, (2003).
92. A. Enstein, Ann. Phys., **17**, (1905).
93. C. Berglund and W. Spicer, *Photoemission Studies of Copper and Silver: Theory*, Phys. Rev., **136**, (1964).
94. D. P. Woodruff and T. A. Delchar, *Modern Techniques of Surface Science*, Cambridge University Press, (1994).
95. L. Wang, *SPECTROSCOPY AND SCANNING PROBE MICROSCOPY STUDIES OF FULLERENE-SILICON INTERACTION*, Ph.D. thesis,*University of Nottingham* (2005).
96. J. B. Hudson, *Surface Science*, Butterworth-Heinemann, Stoneham, MA, (1992).
97. A. Damascelli, Z. Hussain and Z.-X. Shen, *Angle-resolved photoemission studies of the cuprate superconductors*, Rev. Mod. Phys., **75**, 473, (2003).
98. J. Stöhr, *NEXAFS spectroscopy*, Springer, Berlin, (1992).
99. G. Binnig, H. Rohrer, C. Gerber and E. Weibel, *Tunneling through a controllable vacuum gap*, Appl. Phys. Lett., **40**, 178, (1982).
100. Schematic structure of Omicron room temperature STM/AFM, available at: http://www.physics.purdue.edu/nanophys/newpage10-03/equipment/omicron.htm.
101. V. W. Brar, Y. Zhang, Y. Yayon, T. Ohta, J. L. McChesney, A. Bostwick, E. Rotenberg, K. Horn and M. F. Crommie, *Scanning tunneling spectroscopy of inhomogeneous electronic structure in monolayer and bilayer graphene on SiC*, Appl. Phys. Lett., **91**, 122102, (2007).
102. R. A. Bennett, P. Stone, N. J. Price and M. Bowker, *Two (1 x 2) reconstructions of TiO2(110): Surface rearrangement and reactivity studied using elevated temperature scanning tunneling microscopy*, Phys. Rev. Lett., **82**, 3831, (1999).
103. H. L. Zhang, W. Chen, H. Huang, L. Chen and A. T. S. Wee, *Preferential trapping of C-60 in nanomesh voids*, J. Am. Chem. Soc., **130**, 2720, (2008).
104. Schematic view of a typical LEED system, available at: http://www.chembio.uoguelph.ca/thomas/oldthom/LEEDexpl.htm.
105. Eward sphere to explain the electron diffraction in LEED, available at: http://en.wikipedia.org/wiki/Low-energy_electron_diffraction.
106. C. Kittel, *Introduction to solid state physics*, Wiley, Hoboken, NJ (2005).
107. M. V. Hove, W. Weinberg and C. Chan, *Low-energy Electron Diffraction: Experiment, Theory, and Surface Structure Determination*, Springer-Verlag, (1986).
108. H. O. Moser, B. D. F. Casse, E. P. Chew, M. Cholewa, C. Z. Diao, S. X. D. Ding, J. R. Kong, Z. W. Li, M. Hua, M. L. Ng, B. T. Saw, S. bin Mahmood, S. V. Vidyaraj, O. Wilhelmi, J. Wong, P. Yang, X. J. Yu, X. Y. Gao, A. T. S. Wee, W. S. Sim, D. Lu and R. B. Faltermeier, *Status of and materials research at SSLS*, Nucl. Instr. Methods B, **238**, 83, (2005).
109. Schematic layout of surface, interface and nanostructure (SINS) beamline, SSLS, available at: http://ssls.nus.edu.sg/facility/beamlines/sins/beamline.htm.
110. X. J. Yu, O. Wilhelmi, H. O. Moser, S. V. Vidyaraj, X. Y. Gao, A. T. S. Wee, T. Nyunt, H. J. Qian and H. W. Zheng, *New soft X-ray facility SINS for surface and nanoscale science at SSLS*, J. Electron Spectrosc. Relat. Phenom., **144**, 1031, (2005).
111. D. Qi, *ORGANIC MOLECULES ON DIAMOND (001): A SYNCHROTRON STUDY*, Ph.D. thesis,*National University of Singapore* (2009).
112. Omicron LT-STM system in surface science lab, physics department, NUS, available at: http://www.physics.nus.edu.sg/~surface/Equipment/LT-STM.htm.

113. H. Huang, W. Chen and A. T. S. Wee, *Low-Temperature Scanning Tunneling Microscopy Investigation of Epitaxial Growth of F16CuPc Thin Films on Ag(111)*, J. Phys. Chem. C, **112**, 14913, (2008).
114. K. Yoshida, T. Takayama and T. Hori, *Compact synchrotron light source of the HSRC*, J. Synchrotron Radiat., **5**, 345, (1998).
115. S. Yagi, G. Kutluk, T. Matsui, A. Matano, A. Hiraya, E. Hashimoto and M. Taniguchi, *Design and performance of a soft X-ray double crystal monochromator at HSRC*, Nucl. Instr. Methods A, **467**, 723, (2001).
116. M. P. Seah and W. A. Dench, *Quantitative electron spectroscopy of surface: a standard data base for electron inelastic mean free paths in solids*, Surf. Interface Anal., **1**, (1979).
117. L. I. Johansson, F. Owman and P. Mårtensson, *A photoemission study of 4H-SiC(0001)*, Surf. Sci., **360**, L483, (1996).
118. F. Varchon, R. Feng, J. Hass, X. Li, B. N. Nguyen, C. Naud, P. Mallet, J. Y. Veuillen, C. Berger, E. H. Conrad and L. Magaud, *Electronic structure of epitaxial graphene layers on SiC: Effect of the substrate*, Phys. Rev. Lett., **99**, 126805, (2007).
119. A. Mattausch and O. Pankratov, *Ab initio study of graphene on SiC*, Phys. Rev. Lett., **99**, 076802, (2007).
120. J. H. Park, W. C. Mitchel, H. E. Smith, L. Grazulis and K. G. Eyink, *Studies of interfacial layers between 4H-SiC (0 0 0 1) and graphene*, **48**, 1670, (2010).
121. G. M. Whitesides and B. Grzybowski, *Self-assembly at all scales*, Science, **295**, 2418, (2002).
122. A. L. Ankudinov, B. Ravel, J. J. Rehr and S. D. Conradson, *Real-space multiple-scattering calculation and interpretation of x-ray-absorption near-edge structure*, Phys. Rev. B, **58**, 7565, (1998).
123. A. M. Haghiri-Gosnet, F. Rousseaux, E. Gat, J. Durand and A. M. Flank, *Structural properties of amorphous SiC films and x-ray membranes by EXAFS*, Microelectronic Engineering, **17**, 215, (1992).
124. Y. Baba, T. Sekiguchi, I. Shimoyama and K. G. Nath, *Structures of sub-monolayered silicon carbide films*, Appl. Surf. Sci., **237**, 176, (2004).
125. Y. H. Tang, T. K. Sham, D. Yang and L. Xue, *Preparation and characterization of pulsed laser deposition (PLD) SiC films*, Appl. Surf. Sci., **252**, 3386, (2006).
126. R. Nakajima, J. Stöhr and Y. U. Idzerda, *Electron-yield saturation effects in L-edge x-ray magnetic circular dichroism spectra of Fe, Co, and Ni*, Phys. Rev. B, **59**, 6421, (1999).
127. M. Krawczyk, L. Zommer, A. Kosiński, J. W. Sobczak and A. Jablonski, *Measured electron IMFPs for SiC*, Surf. Interface Anal., **38**, 644, (2006).
128. J. H. Hubbell and S. M. Seltzer, *Tables of X-Ray Mass Attenuation Coefficients and Mass Energy-Absorption Coefficients*, (NIST, Gaiherburg, 1996), from online database "NIST Standard Reference Database 126, online May 1996; last update July 2004," see http://physics.nist.gov/PhysRefData/XrayMassCoef/cover.html
129. C. Radtke, I. J. R. Baumvol, F. C. Stedile, I. C. Vickridge, I. Trimaille, J. Ganem and S. Rigo, *Thermal growth of SiO2 on SiC investigated by isotopic tracing and subnanometric depth profiling*, Appl. Surf. Sci., **212-213**, 570, (2003).
130. I. C. Vickridge, I. Trimaille, J. J. Ganem, S. Rigo, C. Radtke, I. J. R. Baumvol and F. C. Stedile, *Limiting step involved in the thermal growth of silicon oxide films on silicon carbide*, Phys. Rev. Lett., **89**, 256102, (2002).

131. C. J. Glover, G. J. Foran and M. C. Ridgway, *Structure of amorphous silicon investigated by EXAFS*, Nucl. Instr. Methods B, **199**, 195, (2003).
132. K. V. Emtsev, A. Bostwick, K. Horn, J. Jobst, G. L. Kellogg, L. Ley, J. L. McChesney, T. Ohta, S. A. Reshanov, J. Röhrl, E. Rotenberg, A. K. Schmid, D. Waldmann, H. B. Weber and T. Seyller, *Towards wafer-size graphene layers by atmospheric pressure graphitization of silicon carbide*, Nature Mater., **8**, 203, (2009).
133. J. B. Hannon and R. M. Tromp, *Pit formation during graphene synthesis on SiC(0001): In situ electron microscopy*, Phys. Rev. B, **77**, 241404R, (2008).
134. S. Unarunotai, Y. Murata, C. E. Chialvo, H. S. Kim, S. MacLaren, N. Mason, I. Petrov and J. A. Rogers, *Transfer of graphene layers grown on SiC wafers to other substrates and their integration into field effect transistors*, Appl. Phys. Lett., **95**, 202101, (2009).
135. C. Virojanadara and L. I. Johansson, *Metastable oxygen adsorption on SiC(0001)-root 3x root 3 R30 degrees*, Surf. Sci., **519**, 73, (2002).
136. C. Virojanadara and L. I. Johansson, *Oxidation studies of 4H-SiC(0001) and (000-1)*, Surf. Sci., **505**, 358, (2002).
137. G. M. Rutter, J. N. Crain, N. P. Guisinger, T. Li, P. N. First and J. A. Stroscio, *Scattering and interference in epitaxial graphene*, Science, **317**, 219, (2007).
138. F. Hiebel, P. Mallet, F. Varchon, L. Magaud and J. Y. Veuillen, *Scanning Tunneling Microscopy investigation of the graphene/6H-SiC(000(1)over-bar) (3 x 3) interface*, Solid State Comm., **149**, 1157, (2009).
139. P. Ruffieux, O. Groning, P. Schwaller, L. Schlapbach and P. Gröning, *Hydrogen atoms cause long-range electronic effects on graphite*, Phys. Rev. Lett., **84**, 4910, (2000).
140. H. A. Mizes and J. S. Foster, *LONG-RANGE ELECTRONIC PERTURBATIONS CAUSED BY DEFECTS USING SCANNING TUNNELING MICROSCOPY*, Science, **244**, 559, (1989).
141. L. Tapasztó, G. Dobrik, P. Lambin and L. P. Biró, *Tailoring the atomic structure of graphene nanoribbons by scanning tunnelling microscope lithography*, Nature Nano., **3**, 397, (2008).
142. H. Yang, G. Baffou, A. J. Mayne, G. Comtet, G. Dujardin and Y. Kuk, *Topology and electron scattering properties of the electronic interfaces in epitaxial graphene probed by resonant tunneling spectroscopy*, Phys. Rev. B, **78**, 041408R, (2008).
143. G. Ashkenasy, D. Cahen, R. Cohen, A. Shanzer and A. Vilan, *Molecular engineering of semiconductor surfaces and devices*, Acc. Chem. Res., **35**, 121, (2002).
144. S. De Feyter and F. C. De Schryver, *Two-dimensional supramolecular self-assembly probed by scanning tunneling microscopy*, Chem. Soc. Rev., **32**, 139, (2003).
145. G. Heimel, L. Romaner, E. Zojer and J. L. Bredas, *The interface energetics of self-assembled monolayers on metals*, Acc. Chem. Res., **41**, 721, (2008).
146. S. D. Wang, X. Dong, C. S. Lee and S. T. Lee, *Orderly growth of copper phthalocyanine on highly oriented pyrolytic graphite (HOPG) at high substrate temperatures*, J. Phys. Chem. B, **108**, 1529, (2004).
147. W. Chen, H. Huang, S. Chen, X. Y. Gao and A. T. S. Wee, *Low-temperature scanning tunneling microscopy and near-edge X-ray absorption fine structure investigations of molecular orientation of copper(II) phthalocyanine thin films at organic heterojunction interfaces*, J. Phys. Chem. C, **112**, 5036, (2008).
148. S. X. Yin, C. Wang, B. Xu and C. L. Bai, *Studies of CuPc adsorption on graphite surface and alkane adlayer*, J. Phys. Chem. B, **106**, 9044, (2002).

149. R. Strohmaier, C. Ludwig, J. Petersen, B. Gompf and W. Eisenmenger, *Scanning tunneling microscope investigations of lead-phthalocyanine on MoS2*, J. Vac. Sci. Technol. B, **14**, 1079, (1996).

150. C. Gunther, N. Karl, J. Pflaum, R. Strohmaier, B. Gompf, W. Eisenmenger, M. Muller and K. Mullen, *LEED, STM, and TDS studies of ordered thin films of the rhombus-shaped polycondensed aromatic hydrocarbon C54H22, on MoS2, GeS, and graphite*, Langmuir, **21**, 656, (2005).

151. J. Y. Grand, T. Kunstmann, D. Hoffmann, A. Haas, M. Dietsche, J. Seifritz and R. Möller, *Epitaxial growth of copper phthalocyanine monolayers on Ag(111)*, Surf. Sci., **366**, 403, (1996).

152. W. Chen, H. L. Zhang, H. Huang, L. Chen and A. T. S. Wee, *Self-assembled organic donor/acceptor nanojunction arrays*, Appl. Phys. Lett., **92**, (2008).

153. M. Stöhr, T. Wagner, M. Gabriel, B. Weyers and R. Möller, *Binary molecular layers of C-60 and copper phthalocyanine on Au(111): Self-organized nanostructuring*, Adv. Funct. Mater., **11**, 175, (2001).

154. S. Yoshimoto, A. Tada, K. Suto and K. Itaya, *Adlayer structures and electrocatalytic activity for O-2 of metallophthalocyanines on Au(111): In situ scanning tunneling microscopy study*, J. Phys. Chem. B, **107**, 5836, (2003).

155. X. Lu, K. W. Hipps, X. D. Wang and U. Mazur, *Scanning tunneling microscopy of metal phthalocyanines: d(7) and d(9) cases*, J. Am. Chem. Soc., **118**, 7197, (1996).

156. X. Lu and K. W. Hipps, *Scanning tunneling microscopy of metal phthalocyanines: d(6) and d(8) cases*, J. Phys. Chem. B, **101**, 5391, (1997).

157. J. T. Sadowski, Y. Fujikawa, K. F. Kelly, K. Nakayama, T. Sakurai, E. T. Mickelson, R. H. Hauge and J. L. Margrave, *Fluorinated fullerene thin films on Si(111)-(7x7) surface*, Mater. Charact., **48**, 127, (2002).

158. S. Dobrin, K. R. Harikumar, C. F. Matta and J. C. Polanyi, *An STM study of the localized atomic reaction of 1,2- and 1,4-dibromoxylene with Si(111)-7x7*, Surf. Sci., **580**, 39, (2005).

159. K. S. Yong, Y. P. Zhang, S. W. Yang and G. Q. Xu, *Naphthalene adsorption on Si(111)-7 x 7*, Surf. Sci., **602**, 1921, (2008).

160. T. Suzuki, D. C. Sorescu and J. T. Yates, *The chemisorption of pentacene on Si(001)-2 x 1*, Surf. Sci., **600**, 5092, (2006).

161. D. Choudhary, P. Clancy and D. R. Bowler, *Adsorption of pentacene on a silicon surface*, Surf. Sci., **578**, 20, (2005).

162. J. Lu, S. B. Lei, Q. D. Zeng, S. Z. Kang, C. Wang, L. J. Wan and C. L. Bai, *Template-induced inclusion structures with copper(II) phthalocyanine and coronene as guests in two-dimensional hydrogen-bonded host networks*, J. Phys. Chem. B, **108**, 5161, (2004).

163. W. Chen, H. L. Zhang, H. Xu, E. S. Tok, K. P. Loh and A. T. S. Wee, *C-60 on SiC nanomesh*, J. Phys. Chem. B, **110**, 21873, (2006).

164. X. D. Wang, T. Hashizume, H. Shinohara, Y. Saito, Y. Nishina and T. Sakurai, *ADSORPTION OF C60 AND C84 ON THE SI(100)2X1 SURFACE STUDIED BY USING THE SCANNING TUNNELING MICROSCOPE*, Phys. Rev. B, **47**, 15923, (1993).

165. H. Liu and P. Reinke, *C-60 thin film growth on graphite: Coexistence of spherical and fractal-dendritic islands*, J. Chem. Phys., **124**, 164707, (2006).

166. E. I. Altman and R. J. Colton, *THE INTERACTION OF C-60 WITH NOBLE-METAL SURFACES*, Surf. Sci., **295**, 13, (1993).

167. B. Krause, F. Schreiber, H. Dosch, A. Pimpinelli and O. H. Seeck, *Temperature dependence of the 2D-3D transition in the growth of PTCDA on Ag(111): A real-time X-ray and kinetic Monte Carlo study*, Europhys. Lett., **65**, 372, (2004).
168. I. Markov, *Method for evaluation of the Ehrlich-Schwoebel barrier to interlayer transport in metal homoepitaxy*, Phys. Rev. B, **54**, 17930, (1996).
169. Z. Y. Zhang and M. G. Lagally, *Atomistic processes in the early stages of thin-film growth*, Science, **276**, 377, (1997).
170. H. Ishii, K. Sugiyama, E. Ito and K. Seki, *Energy level alignment and interfacial electronic structures at organic metal and organic organic interfaces*, Adv. Mater., **11**, 605, (1999).
171. N. Koch, J. Ghijsen, R. L. Johnson, J. Schwartz, J. J. Pireaux and A. Kahn, *Physisorption-like interaction at the interfaces formed by pentacene and samarium*, J. Phys. Chem. B, **106**, 4192, (2002).
172. R. W. Lof, M. A. Vanveenendaal, B. Koopmans, H. T. Jonkman and G. A. Sawatzky, *BAND-GAP, EXCITONS, AND COULOMB INTERACTION IN SOLID C-60*, Phys. Rev. Lett., **68**, 3924, (1992).
173. J. H. Weaver, J. L. Martins, T. Komeda, Y. Chen, T. R. Ohno, G. H. Kroll, N. Troullier, R. E. Haufler and R. E. Smalley, *ELECTRONIC-STRUCTURE OF SOLID C60 - EXPERIMENT AND THEORY*, Phys. Rev. Lett., **66**, 1741, (1991).
174. P. Reinke, H. Feldermann and P. Oelhafen, *C-60 bonding to graphite and boron nitride surfaces*, J. Chem. Phys., **119**, 12547, (2003).
175. H. Ulbricht, G. Moos and T. Hertel, *Interaction of C-60 with carbon nanotubes and graphite*, Phys. Rev. Lett., **90**, 095501, (2003).
176. S. Saito and A. Oshiyama, *COHESIVE MECHANISM AND ENERGY-BANDS OF SOLID C_{60}*, Phys. Rev. Lett., **66**, 2637, (1991).
177. H. Kröger, P. Reinke, M. Büttner and P. Oelhafen, *Gold cluster formation on a fullerene surface*, J. Chem. Phys., **123**, 114706, (2005).
178. C. Ludwig, R. Strohmaier, J. Petersen, B. Gompf and W. Eisenmenger, *EPITAXY AND SCANNING-TUNNELING-MICROSCOPY IMAGE-CONTRAST OF COPPER PHTHALOCYANINE ON GRAPHITE AND MoS_2*, J. Vac. Sci. Technol. B, **12**, 1963, (1994).
179. K. Manandhar, T. Ellis, K. T. Park, T. Cai, Z. Song and J. Hrbek, *A scanning tunneling microscopy study on the effect of post-deposition annealing of copper phthalocyanine thin films*, Surf. Sci., **601**, 3623, (2007).
180. M. Kanai, T. Kawai, K. Motai, X. D. Wang, T. Hashizume and T. Sakura, *SCANNING-TUNNELING-MICROSCOPY OBSERVATION OF COPPER-PHTHALOCYANINE MOLECULES ON SI(100) AND SI(111) SURFACES*, Surf. Sci., **329**, L619, (1995).
181. L. Lozzi, S. Santucci, S. La Rosa, B. Delley and S. Picozzi, *Electronic structure of crystalline copper phthalocyanine*, J. Chem. Phys., **121**, 1883, (2004).
182. F. Evangelista, V. Carravetta, G. Stefani, B. Jansik, M. Alagia, S. Stranges and A. Ruocco, *Electronic structure of copper phthalocyanine: An experimental and theoretical study of occupied and unoccupied levels*, J. Chem. Phys., **126**, 124709, (2007).
183. W. Chen, H. Huang and A. T. S. Wee, *Molecular orientation transition of organic thin films on graphite: the effect of intermolecular electrostatic and interfacial dispersion forces*, Chem. Commun., 4276, (2008).

184. J. Repp, G. Meyer, S. M. Stojković, A. Gourdon and C. Joachim, *Molecules on insulating films: Scanning-tunneling microscopy imaging of individual molecular orbitals*, Phys. Rev. Lett., **94**, 026803, (2005).

185. D. B. Dougherty, W. Jin, W. G. Cullen, J. E. Reutt-Robey and S. W. Robey, *Variable Temperature Scanning Tunneling Microscopy of Pentacene Monolayer and Bilayer Phases on Ag(111)*, J. Phys. Chem. C, **112**, 20334, (2008).

186. M. Kasaya, H. Tabata and T. Kawai, *Scanning tunneling microscopy and molecular orbital calculation of pentacene molecules adsorbed on the Si(100)2 x 1 surface*, Surf. Sci., **400**, 367, (1998).

187. L. Casalis, M. F. Danisman, B. Nickel, G. Bracco, T. Toccoli, S. Iannotta and G. Scoles, *Hyperthermal molecular beam deposition of highly ordered organic thin films*, Phys. Rev. Lett., **90**, 206101, (2003).

188. C. Baldacchini, F. Allegretti, R. Gunnella and M. G. Betti, *Molecule-metal interaction of pentacene on copper vicinal surfaces*, Surf. Sci., **601**, 2603, (2007).

189. S. J. Kang, Y. Yi, C. Y. Kim, K. H. Yoo, A. Moewes, M. H. Cho, J. D. Denlinger, C. N. Whang and G. S. Chang, *Chemical reaction at the interface between pentacene and HfO_2*, Phys. Rev. B, **72**, 205328, (2005).

190. O. Leenaerts, B. Partoens and F. M. Peeters, *Graphene: A perfect nanoballoon*, Appl. Phys. Lett., **93**, 193107, (2008).

191. A. M. Shikin, D. Farias and K. H. Rieder, *Phonon stiffening induced by copper intercalation in monolayer graphite on Ni(111)*, Europhys. Lett., **44**, 44, (1998).

192. D. Farías, A. M. Shikin, K. H. Rieder and Y. S. Dedkov, *Synthesis of a weakly bonded graphite monolayer on Ni(111) by intercalation of silver*, J. Phys.: Condens. Matter, **11**, 8453, (1999).

193. I. Gierz, C. Riedl, U. Starke, C. R. Ast and K. Kern, *Atomic Hole Doping of Graphene*, Nano Lett., **8**, 4603, (2008).

194. T. Shen, J. J. Gu, M. Xu, Y. Q. Wu, M. L. Bolen, M. A. Capano, L. W. Engel and P. D. Ye, *Observation of quantum-Hall effect in gated epitaxial graphene grown on SiC (0001)*, Appl. Phys. Lett., **95**, 172105, (2009).

195. G. M. Rutter, N. P. Guisinger, J. N. Crain, E. A. A. Jarvis, M. D. Stiles, T. Li, P. N. First and J. A. Stroscio, *Imaging the interface of epitaxial graphene with silicon carbide via scanning tunneling microscopy*, Phys. Rev. B, **76**, 235416, (2007).

196. L. Liu, S. M. Ryu, M. R. Tomasik, E. Stolyarova, N. Jung, M. S. Hybertsen, M. L. Steigerwald, L. E. Brus and G. W. Flynn, *Graphene oxidation: Thickness-dependent etching and strong chemical doping*, Nano Lett., **8**, 1965, (2008).

197. D. Kolacyak, H. Peisert and T. Chassé, *Charge transfer and polarization screening in organic thin films: phthalocyanines on Au(100)*, Appl. Phys. A-Mater. Sci. Process., **95**, 173, (2009).

198. M. V. Gomoyunova and I. I. Pronin, *Binding energy of silicon 2p electrons in iron silicides*, Technic. Phys., **55**, 588, (2010).

199. M. V. Gomoyunova, D. E. Malygin, I. I. Pronin, A. S. Voronchikhin, D. V. Vyalikh and S. L. Molodtsov, *Initial stages of iron silicide formation on the Si(100)2 x 1 surface*, Surf. Sci., **601**, 5069, (2007).

200. I. I. Pronin, M. V. Gomoyunova, D. E. Malygin, D. V. Vyalikh, Y. S. Dedkov and S. L. Molodtsov, *Magnetic ordering of the Fe/Si interface and its initial formation*, J. Appl. Phys., **104**, 104914, (2008).

201. W. Norimatsu and M. Kusunoki, *Transitional structures of the interface between graphene and 6H-SiC (0001)*, Chem. Phys. Lett., **468**, 52, (2009).
202. S. Tanuma, C. J. Powell and D. R. Penn, *Calculations of electron inelastic mean free paths. VIII. Data for 15 elemental solids over the 50-2000 eV range*, Surf. Interface Anal., **37**, 1, (2005).